

3-2016

Mechanical dispersion of semi-solid binders in high-shear granulation

Nathan J. Davis
Purdue University

Follow this and additional works at: https://docs.lib.purdue.edu/open_access_dissertations



Part of the [Chemical Engineering Commons](#)

Recommended Citation

Davis, Nathan J., "Mechanical dispersion of semi-solid binders in high-shear granulation" (2016). *Open Access Dissertations*. 637.
https://docs.lib.purdue.edu/open_access_dissertations/637

This document has been made available through Purdue e-Pubs, a service of the Purdue University Libraries. Please contact epubs@purdue.edu for additional information.

**PURDUE UNIVERSITY
GRADUATE SCHOOL
Thesis/Dissertation Acceptance**

This is to certify that the thesis/dissertation prepared

By Nathan J. Davis

Entitled

MECHANICAL DISPERSION OF SEMI-SOLID BINDERS IN HIGH-SHEAR GRANULATION

For the degree of Doctor of Philosophy

Is approved by the final examining committee:

James D. Litster

Chair

Carl Wassgren

Zoltan Nagy

Gintaras Reklaitis

To the best of my knowledge and as understood by the student in the Thesis/Dissertation Agreement, Publication Delay, and Certification Disclaimer (Graduate School Form 32), this thesis/dissertation adheres to the provisions of Purdue University's "Policy of Integrity in Research" and the use of copyright material.

Approved by Major Professor(s): James D. Litster

Approved by: John Morgan

Head of the Departmental Graduate Program

3/3/2016

Date

MECHANICAL DISPERSION OF SEMI-SOLID BINDERS IN HIGH-SHEAR
GRANULATION

A Dissertation

Submitted to the Faculty

of

Purdue University

by

Nathan J. Davis

In Partial Fulfillment of the

Requirements for the Degree

of

Doctor of Philosophy

May 2016

Purdue University

West Lafayette, Indiana

Soli Deo gloria

To my parents, brother, sister and the rest of my family,
thank you for your love and support.

ACKNOWLEDGEMENTS

Thank you to Jim Litster for advising me during my time in graduate school. You have been an incredibly patient and sportive adviser in my life both in graduate school and undergrad.

Thank you to Procter & Gamble for funding the project and especially John Hecht, Steve Glassmeyer, and Yuen-Sin Cheong for their invaluable feedback over the course of the project. Working with all of you has been a very valuable experience that has helped my personal development outside of research.

Thank you also to all of my friends in graduate school who have provided the comradery to make it to the end.

TABLE OF CONTENTS

	Page
LIST OF TABLES	vii
LIST OF FIGURES	ix
ABSTRACT	xvi
CHAPTER 1. INTRODUCTION AND OBJECTIVES	1
1.1 Introduction	1
1.2 Thesis Objectives	6
1.3 Thesis Outline	7
CHAPTER 2. LITERATURE REVIEW	9
2.1 Rate Processes in Granulation.....	9
2.1.1 Wetting and Nucleation	9
2.1.2 Consolidation and Coalescence	14
2.1.2.1 Consolidation.....	14
2.1.2.2 Coalescence	17
2.1.3 Breakage and Attrition.....	22
2.1.4 Rate Processes Summary.....	24
2.2 Population Balance Modeling	24
2.2.1 Population Balance Model Theory	24
2.2.2 Multiscale and Compartment Modeling	29
2.3 Discrete Element Method Modelling	34
2.4 Literature Review Summary	41
CHAPTER 3. MECHANICAL DISPERSION OF SEMI-SOLID BINDERS IN HIGH SHEAR GRANULATION	43
3.1 Introduction	43

	Page
3.2 Theory	44
3.2.1 Probability of breakage given an impact has occurred	45
3.2.2 Impact Efficiency.....	47
3.3 Methods and Materials	48
3.3.1 Materials:	48
3.3.2 Mechanical Dispersion Experiments	51
3.3.3 Granule Characterization:	53
3.4 Results	54
3.4.1 Surfactant Yield Stress:	54
3.4.2 Mechanical Dispersion Kinetics:	59
3.4.3 System Parameter Effects on Mechanical Dispersion:	66
3.5 Discussion	68
3.5.1 Stokes Deformation Number	69
3.5.2 Number of Impacts	71
3.6 Conclusions	76
CHAPTER 4. POPULATION BALANCE MODELING OF SEMI-SOLID BINDER	
MECHANICAL DISPERSION AS A MILLING PROCESS	78
4.1 Introduction	78
4.2 Theory	79
4.3 Model Solution.....	84
4.3.1 Parameter Estimation.....	85
4.3.2 Parameter Estimation Strategy	86
4.3.3 Measure of Success.....	88
4.4 Results and Discussion.....	89
4.4.1 Parameter Estimation 1	89
4.4.2 Parameter Estimation 2.....	94
4.4.3 Parameter Estimation 3.....	100
4.5 Conclusions	106

	Page
CHAPTER 5. PREDICTING LOCAL SHEAR IN POWDER FLOW USING DEM: EFFECT OF SIMULATION PARAMETERS.....	108
5.1 Introduction	108
5.2 Methods.....	109
5.2.1 Simulations	109
5.2.2 Post Processing	114
5.3 Results and Discussion.....	115
5.3.1 Shear Flow	115
5.3.2 Shear Cell Stress	124
5.3.3 Particle of Interest Stress	128
5.3.4 von Mises yield criterion	132
5.4 Conclusions	133
CHAPTER 6. CONCLUSIONS AND RECOMENDATIONS.....	135
6.1 Major Conclusions	135
6.2 Recommendations for Further Study	137
REFERENCES	139
APPENDICES	
Appendix A Kinetic Data.....	155
Appendix B Full size distributions of breakage model.....	158
VITA.....	164

LIST OF TABLES

Table	Page
Table 1.1 Types of granulators in industrial applications.....	2
Table 2.1 Proposed breakage kernels in the literature. Expanded from Kumar et al. 2013 ⁵	27
Table 2.2 Summary of multiscale population balance models in the literature.....	32
Table 2.3 Collision Model types and examples. Adapted from Stevens et. al. 2005 ⁹² and Freireich et. al. 2009 ⁹⁴	37
Table 3.1 Properties of sodium aluminosilicate powder.....	49
Table 3.2 Operating Conditions for Mechanical Dispersion Experiments.....	52
Table 3.3 Stokes deformation numbers using room temperature and injection temperature yield stress.....	70
Table 4.1 Description of breakage model parameters.	83
Table 4.2 Estimated parameters using only 1200 RPM experiments for surfactant A.....	89
Table 4.3 Estimated parameters using all surfactant A experiments.....	94
Table 4.4 Surfactant B estimated parameter q using 1200 RPM data. Other parameters are from parameter estimation 1.	101
Table 5.1 Constant parameters of the unit cell model design.....	112
Table 5.2 Varied Simulation parameters and material properties.....	112
Table 5.3 von Mises yield criterion varying shear cell parameters	133

Table	Page
Table 5.4 von Mises yield criterion varying Young's modulus.....	133
Table 5.5 von Mises yield criterion varying friction coefficient	133

LIST OF FIGURES

Figure	Page
Figure 1.1.1 The three rate processes of granulation. Adapted from Litster and Ennis 2004 ² .	4
Figure 2.1.1 Nucleation mechanism for case when liquid drop size is larger than particle size. Adapted from Hapgood et al. ¹⁰	10
Figure 2.1.2 Nucleation regime map proposed by Hapgood et al. ¹¹	11
Figure 2.1.3 Schematic of two liquid bound granules coalescing adapted from Iveson et al 2001 ¹ .	18
Figure 2.1.4 Regime map showing the solution to the coalescence mechanisms ³⁴	19
Figure 2.1.5 Growth regime map (a) and validated map (b) adapted from Iveson et al. ^{37,38}	21
Figure 2.2.1 Forberg mixer coater and compartment model adapted from Li et al 2011 ⁶⁸ .	31
Figure 2.3.1 DEM Vertical High Shear Mixer system in EDEM.	35
Figure 2.3.2 Normal and tangential forces shown together using spring and dashpot models for each and a friction slider in the tangential direction. Image adapted from Gantt et. al. 2006 ⁷⁸ .	36
Figure 2.3.3 DEM 2D shear cell showing granule breakup at high stokes deformation numbers. Adapted from Tardos et al. 2000 ¹⁰⁶	38

Figure	Page
Figure 2.3.4 2D coalescence of granules. Adapted from Adams et al. 1998 ⁸⁰	39
Figure 3.3.1 Particle Volume Distribution for sodium aluminosilicate powder.....	49
Figure 3.3.2 Experimental schedule for mechanical dispersion experiments.....	53
Figure 3.4.1 Typical results for step transient stress growth (surfactant A, 60 °C shear rate 1 s ⁻¹).	55
Figure 3.4.2 Dependence of measured peak stress on shear rate for Surfactant A at 60 °C.	56
Figure 3.4.3 Regression of stress strain data the yield stress is the slope of the line (surfactant A), compression speed 10 ⁻³ ms ⁻¹	57
Figure 3.4.4 Yield stress for a) surfactant A and b) surfactant B for various compression velocities.	58
Figure 3.4.5 a) Material in Pan and b) material on sieve after sieve analysis for surfactant A.....	60
Figure 3.4.6 Volume log frequency distributions showing mechanical dispersion kinetics for surfactant A with an injection temperature of 60 °C at a) 1200 RPM, b) 900 RPM, c) 600 RPM.	61
Figure 3.4.7 Volume log frequency distributions showing mechanical dispersion kinetics for surfactant B with an injection temperature of 60 °C at a) 1200 RPM, b) 900 RPM, c) 600 RPM.	62
Figure 3.4.8 a) d ₃₂ and b) σ / d_{32} for surfactant A kinetics at 60 °C.....	64
Figure 3.4.9 a) d ₃₂ and b) σ / d_{32} for surfactant B kinetics at 60 °C.....	65

Figure	Page
Figure 3.4.10 Impeller speed dependence of the d_{32} and σ/d_{32} at 60 °C injection temperature and 10 sec mixing time for (a) surfactant A and (b) surfactant B.	67
Figure 3.4.11 Temperature dependence of the d_{32} for surfactant A and B at 1200 RPM and 2 s and 10 s mixing time.	68
Figure 3.5.1 Sauter mean size at 60 °C versus number of impeller revolutions at 60 °C for (a) surfactant A and (b) surfactant B.	73
Figure 3.5.2 first 50 revolutions at all impeller speeds and 60 °C injection temperature for (a) surfactant A and (b) surfactant B.	75
Figure 4.3.1 gSOLIDS process flow sheet for the breakage process.	84
Figure 4.3.2 Flow sheet for parameter estimation of surfactant A and B.	88
Figure 4.4.1 Particle size distributions of model and experiments for Surfactant A at 1200 RPM fit to 1200 RPM experiment data.	91
Figure 4.4.2 a) d_{32} and b) σ/d_{32} for surfactant A at 1200 RPM fit to 1200 RPM experimental data.	91
Figure 4.4.3 a) d_{32} and b) σ/d_{32} for surfactant A at 900 RPM fit to 1200 RPM experimental data.	92
Figure 4.4.4 a) d_{32} and b) σ/d_{32} for surfactant A at 600 RPM fit to 1200 RPM experimental data.	93
Figure 4.4.5 Particle size distributions for model and experiments for Surfactant A at 1200 RPM fit using all experiments.	95
Figure 4.4.6 a) d_{32} and b) σ/d_{32} for surfactant A at 1200 RPM fit using all surfactant A experiments.	96

Figure	Page
Figure 4.4.7 a) d_{32} and b) σ/d_{32} for surfactant A at 900 RPM fit using all surfactant A experiments.	97
Figure 4.4.8 a) d_{32} and b) σ/d_{32} for surfactant A at 600 RPM fit using all surfactant A experiments.	98
Figure 4.4.9 Efficiency plot as a function of particle size and velocity. Solid line is values from parameter estimation 1 and dotted line is values from parameter estimation 2.	100
Figure 4.4.10 Particle size distributions for model and experiments for Surfactant B at 1200 RPM fit using all experiments.	102
Figure 4.4.11 a) d_{32} and b) σ/d_{32} for surfactant B at 1200 RPM with λ_1 and Stk^* from parameter estimation 1 and q estimated from surfactant B experiments at 1200 RPM..	103
Figure 4.4.12 a) d_{32} and b) σ/d_{32} for surfactant B at 900 RPM with λ_1 and Stk^* from parameter estimation 1 and q estimated from surfactant B experiments at 1200 RPM..	104
Figure 4.4.13 a) d_{32} and b) σ/d_{32} for surfactant B at 900 RPM with λ_1 and Stk^* from parameter estimation 1 and q estimated from surfactant B experiments at 1200 RPM..	105
Figure 5.2.1 Shear unit cell model based on Kholá and Wassgren ¹²⁵ . Large particle of interest can be seen in the center of the bed in white, the bulk particles in blue, and the wall particles in red.	110
Figure 5.3.1 Shear profile every 5000 time steps for the base case conditions at shear rates a) 0 s^{-1} b) 1 s^{-1} c) 5 s^{-1} d) 10 s^{-1}	117
Figure 5.3.2 a) Dimensionless velocity and b) actual shear rate versus dimensionless bed height as a function of shear rate (γ) with the remaining parameters at base case conditions.	119

Figure	Page
Figure 5.3.3 a) Dimensionless velocity and b) actual shear rate versus dimensionless bed height as a function of bed fraction(χ) with the remaining parameters at base case conditions.....	120
Figure 5.3.4 Dimensionless velocity and b) actual shear rate versus dimensionless bed height as a function of Young's Modulus (E) with the remaining parameters at base case conditions.....	122
Figure 5.3.5 Dimensionless velocity and b) actual shear rate versus dimensionless bed height as a function of the friction coefficient (μ) with the remaining parameters at base case conditions.....	123
Figure 5.3.6 a) Pressure and b) deviatoric stress versus dimensionless bed height as a function of shear rate with the remaining parameters at base case conditions.	125
Figure 5.3.7 a) Pressure and b) deviatoric stress versus dimensionless bed height as a function of bed fraction below the particle of interest with the remaining parameters at base case conditions.....	126
Figure 5.3.8 a) Pressure and b) deviatoric stress versus dimensionless bed height as a function of Young's Modulus with the remaining parameters at base case conditions..	127
Figure 5.3.9 a) Pressure and b) deviatoric stress versus dimensionless bed height as a function of the friction coefficient with the remaining parameters at base case conditions.....	128
Figure 5.3.10 Effect of shear rate on pressure and deviatoric stress at a shear rate of 1 s ⁻¹ and bed fractions of a) 0.3 b) 0.4 c) 0.5 and d) 0.6.....	130

Figure	Page
Figure 5.3.11 Effect of the young's modulus of the bulk material on the stress experienced by the particle of interest at a shear rate of 1 s^{-1} and bed fraction of a) 0.4 and b) 0.5	131
Figure 5.3.12 Effect of the coefficient of friction on pressure and deviatoric stress at a shear rate of 1 s^{-1}	132
Figure A.1 Surfactant A 1200 RPM	155
Figure A.2 Surfactant A 900 RPM	155
Figure A.3 Surfactant A 600 RPM	156
Figure A.4 Surfactant B 1200 RPM.....	156
Figure A.5 Surfactant B 900 RPM.....	156
Figure A.6 Surfactant B 600 RPM.....	157
Figure B.1 Particle size distributions of model and experiments for Surfactant A at 900 RPM fit to 1200 RPM experiment data.	158
Figure B.2 Particle size distributions of model and experiments for Surfactant A at 600 RPM fit to 1200 RPM experiment data.	159
Figure B.3 Particle size distributions of model and experiments for Surfactant A at 900 RPM fit to all experiment data.....	160
Figure B.4 Particle size distributions of model and experiments for Surfactant A at 600 RPM fit to all experiment data.....	161
Figure B.5 Particle size distributions of model and experiments for Surfactant B at 900 RPM fit to 1200 RPM experiment data.	162

Figure	Page
Figure B.6 Particle size distributions of model and experiments for Surfactant B at 900 RPM fit to 1200 RPM experiment data.	163

ABSTRACT

Davis, Nathan J. Ph.D., Purdue University, May 2016. Mechanical Dispersion of Semi-Solid Binders in High-Shear Granulation: Major Professor: James D. Litster.

Granulation is an important industrial process used to produce many foods, medicines, consumer products, and industrial intermediate products. This thesis focuses on high shear wet granulation with the specific case study of detergent manufacture using a high shear pin mixer. The key rate process in detergent manufacturing was determined to be the mechanical dispersion of the semi-solid surfactant binder. The pin mixer and mechanical dispersion utilized experiments, population balance models, and discrete element method (DEM) models.

The mechanical dispersion of the surfactant binder was studied using a lab scale 6 liter pin mixer. An experimental method was developed to isolate mechanical dispersion from the other rate processes of granulation. Experiments were conducted over a range of impeller speeds, mixing times, and surfactant injection temperatures. Two surfactants were used each with different yield stresses. The yield stresses of both surfactants were characterized using uniaxial compression tests and extrapolated to the impact speeds observed in the pin mixer. Using the yield stress to calculate the Stokes deformation number revealed that the breakage of surfactant would occur at all impact conditions in the pin mixer. The mechanical dispersion results demonstrated that the rate process could

be modeled as a breakage process. The results determined that the key parameter governing the mechanical dispersion of paste was the number of revolutions of the impeller. This implies that impaction or sudden stress from the impeller is the mechanism that causes nuclei breakage.

The results of the mechanical dispersion experiments were then used to develop a mechanistic semi-empirical model. Because the results indicated that breakage should occur for every impact with the impeller, the model was based on particle impact efficiency between the impeller and nuclei. The impact efficiency was described in a way similar to particle gas filtration where the Stokes number is the characteristic dimensionless group. The population balance model was breakage only and was able to accurately predict the full size distributions of the surfactant nuclei. The results showed that the model was able to accurately account for the effect of tip speed and number of revolutions. This was found by fitting the simulation to a single impeller speed and then predicting the size distributions by varying only the velocity input.

Finally, a DEM unit shear cell was developed to understand the transmission of stress from a bulk material to a single large particle of interest similar to surfactant nuclei. The simulation examined the effect of both shear rate, placement of the large particle, and the material properties. The results determined that the material properties used in the simulation had a much greater effect on the shear profile and stress in the shear cell than the effect of the macroscopic shear rate. Using the von Mises yield criteria, the results demonstrated that the shear cell transmitted more stress to the large particle than the yield stress characterized experimentally from the surfactant. The results indicate that the surfactant should break in shear within the pin mixer.

Mechanical dispersion has been successfully modeled for the case of detergent granulation in the pin mixer. The combined results demonstrate that mechanical dispersion of surfactant can be modeled as a breakage process. The number of impeller rotations and the Stokes number are key parameters to accurately describe and model the simulation. The surfactant should break apart due to both impact and shear within the granulator.

CHAPTER 1. INTRODUCTION AND OBJECTIVES

1.1 Introduction

Granulation is a common process used to turn one or more primary powders into granules. Fine powders can have many undesirable properties including strong cohesive forces, poor flowability, and, in the case of powder blends, segregation. Creating granules out of the primary powders helps alleviate these problems by creating a product with more desirable properties. The created granules can either be the final product or an intermediate for use in a further process.

Examples of granulation are wide spread across many industries that handle powder materials including home chemicals such as dry laundry detergent, iron ore processing, intermediate materials such as enzymes, pharmaceutical powders for tableting, and others. In all of these applications, granulation is used to address one of the undesirable characteristics of the fine powders or powder blends that make up the product. Good granulation processes allow for particle design by controlling granule properties especially porosity, composition, and size. Consistent granule properties minimize waste and recycle in industrial process improving yield and reducing cost.

Several different methods have been developed to produce granules with desired properties. Broadly, granulation can be separated into dry and wet granulation. During granulation, the initial powders are combined either with a liquid binder, wet granulation, or without a binder, dry granulation. Dry granulation, such as roll compaction, relies on

inter-particle or inter-molecular bond formation to hold the granule together. In contrast, wet granulation typically uses the liquid to form the bonds between particles. Wet granulation is more difficult to model than dry granulation because of the presence of both a liquid and solid phase. Due to the complexity of wet granulation and the variety of industries that use the process, many different types of granulators have been developed for different applications (see Table 1.1.).

Table 1.1 Types of granulators in industrial applications


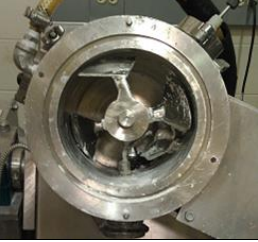

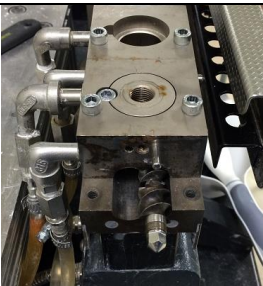


Granulator	Type of Granulation	Example Applications	Image
Vertical High Shear Mixer (VHSM)	Wet, High Shear Batch	Pharmaceuticals	
Horizontal High Shear Mixer (HHSM)	Wet, High Shear, Batch or Continuous	Laundry Detergent, Enzymes	
Fluid Bed Granulator	Wet, Low shear Simultaneous Drying Batch or Continuous	Melt Granulation	

Table 1.1 Continued

Granulator	Type of Granulation	Example Applications	Image
Twin Screw Granulator	Wet, High Shear Continuous	Pharmaceuticals with liquids	
Roll Compaction	Dry, Compaction, Milling Continuous	Solid only pharmaceuticals	
Tumbling Drum	Wet, Low Shear Batch		

Although granulation is a commonly used process, modeling of granulation and especially wet granulation is very difficult and current models are not predictive. The foundation for modern wet granulation modeling was proposed by Ennis and Litster,^{1,2} and describes granulation as a combination of three rate processes. The rate processes, are (i) wetting and nucleation, (ii) consolidation and coalescence, and (iii) attrition and breakage (Figure 1.1). Quantifying, and combining these rate process into a single model has been the focus of current research in the field. However, despite the large amount of

research conducted in the 15 years since these publications, the complex and stochastic nature of granulation has kept predictive modeling of granulation out of reach.

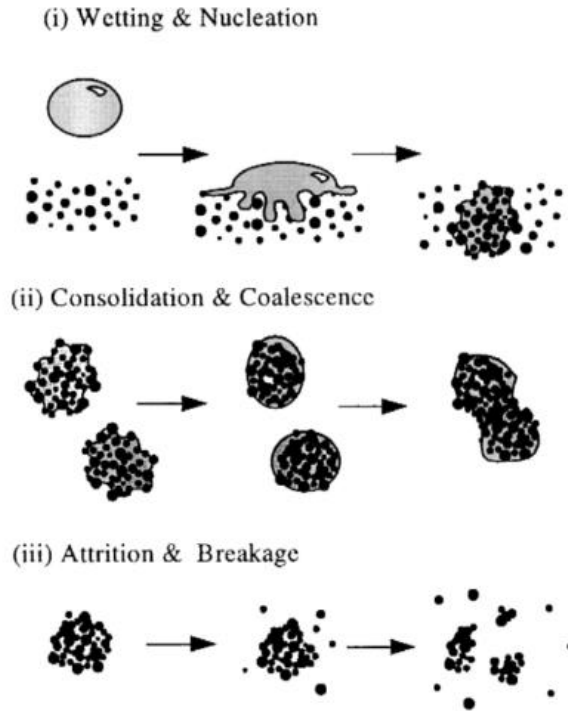


Figure 1.1.1 The three rate processes of granulation. Adapted from Litster and Ennis 2004².

The state of the art for granulation models is currently multi-scale compartment modeling³. Compartment models combine current state of the art models including use semi-empirical or first principle physical models, discrete element method (DEM) models, population balance modeling (PBM), and others. These models are applied to the micro or particle scale, the meso or granule scale, and the macro or granulator scale. First principle or physical models typically focus on the micro scale looking at primary particles and individual granules. These models attempt to create a mathematical model for the three rate process of granulation and many competing models exist³⁻⁵. Such

models predict how primary particles nucleate, how granules densify and coalesce, and other rate processes.

DEM modeling has been used at all scales of granulation to determine information such as bulk powder flow (macro), granule-granule collisions (meso) and inter granule structure (micro). DEM models are computer simulations that solve the equations of motion for a domain of interacting particles. In these simulations, idealized granule interactions can be measured providing information such as granule collision rate and energy, force distributions, and particle velocity. These simulations are handicapped by the limit to current computer power that prevents the number of particles in the simulation from exceeding the order of 10^6 for even the most robust simulations.

Population balance modeling focuses on the meso and macro scale. It is an approach that keeps track of the number of granules that have a specific value of a property or properties such as particle size. Granules will change state based on the boundary conditions and the current state of the granules described mathematically in a kernel. In granulation modeling, kernels are developed for specific rate process using physical or empirical models and may require information from another model such as DEM.

An interesting case study for granulation is the production of dry powder laundry detergent. This process uses two horizontal high shear mixers a plow mixer and a pin mixer. The materials for this process include a powder blend and a highly viscous semi-solid paste⁶. Most prior literature on granulation uses low viscosity, atomized fluids. There is limited work on using semi-solid pastes as binders in granulation. Additionally, several studies in the literature look at a similar case study but in a horizontal plow

mixer⁷. During the pin mixer granulation, the paste is broken up into a distribution of fragments through mechanical dispersion, a nucleation process. The relative simplicity of the system and initial conditions makes this process a good choice for the study of mechanical dispersion. Implementation of mechanical dispersion in a population balance model will provide the first step in a predictive model of the granulator.

1.2 Thesis Objectives

Mechanical Dispersion is very important in the many granulation processes but is not well understood in the literature. The horizontal high shear pin mixer provides an opportunity to develop experiments isolating mechanical dispersion from the other rate processes to produce a population balance model of only mechanical dispersion.

The goal of this thesis is to produce a population balance model of Mechanical Dispersion in the horizontal high shear Pin Mixer granulator. This will be the first study characterizing mechanical dispersion of semi-solid binders. The specific objectives to complete these goals are to:

1. Experimentally isolate mechanical dispersion from the other rate processes in the pin mixer and demonstrate the effect of material properties and operating conditions on mechanical dispersion.
2. Develop a population balance model and rate equation that incorporates material properties, operating conditions, and process knowledge to predict the full particle size distribution of the pin mixer over time.
3. Validate the model using data collected under objective 1.
4. Develop a DEM model of a shear cell to characterize the stress of a large particle in a shear bed and compare this to yield criteria.

1.3 Thesis Outline

The thesis is divided into several chapters to meet the objectives.

Chapter 2 is a review of the relevant literature in granulation. The chapter surveys the granulation rate processes, previous studies with similar materials, population balance modeling as applied to granulation, and DEM modelling of particulate flows. This chapter demonstrates that the proposed objectives fill existing gaps in the literature.

Chapter 3 describes the experimental set up for the pin mixer mechanical dispersion experiments. The experiments use a model system of zeolite and surfactant. The material properties of the zeolite and surfactant are characterized. The experimental system varies surfactant injection temperature, impeller RPM, and mixing time. The resulting particle size distributions are characterized and the Sauter mean size is used to demonstrate the effect of granulator operating conditions.

Chapter 4 describes the implementation of the population balance in gSOLIDS to model the system used in chapter 3. The chapter describes the derivation of a new physically inspired breakage kernel to describe the pin mixer. The model incorporates measurable parameters including granular strength and velocity to track the entire particle size distribution with time. The sensitivity to, and confidence of, the estimated parameters are also discussed.

Chapter 5 describes the development of a discrete element method simulation of a particle shear cell. The shear cell contains one large particle in a bed of smaller particles. The stress observed on the large particle is characterized and compared to yield criteria in the literature. Additionally, the effects of simulation parameters on the stress are also examined to determine the sensitivity of the results.

Chapter 6 summarizes the contributions of the previous chapters and suggests several future directions for study in the area. Appendices are also included to provide supporting information as a stepping stone for future work.

CHAPTER 2. LITERATURE REVIEW

2.1 Rate Processes in Granulation

The modern view of the granulation process is a system of three rate processes; (1) Wetting and Nucleation, (2) Consolidation and Growth, and (3) Attrition and Breakage¹. Due to their complexity, a large number of models exist for each of the rate processes. During a typical granulation, all of the rate processes are occurring to various degrees depending on location within the granulator.

2.1.1 Wetting and Nucleation

The nucleation and wetting rate process is the mechanism where liquid binder and unwet powder come together to form granule nuclei. Although the relative size of the drop to the powder is important, granulation generally focuses on the case when the drop is much larger than the primary powders. There are two mechanisms for wetting when the liquid drop size is larger than the primary powder, immersion and solid spreading⁸. The mechanisms are controlled by thermodynamics of the surface and interface energies between the components. Figure 2.1 shows immersion occurs when the liquid-solid spreading coefficient (λ_{LS}) is positive and liquid is distributed into the powder bed by wetting and capillary action. In this case it is energetically favorable for the binder to increase the amount of surface area in contact with the powder. Solid spreading occurs when the solid-liquid spreading coefficient (λ_{SL}) is positive and the binder reduces the

contact area with the powder such as with hydrophobic powders where the particles coat the liquid center forming liquid marbles^{9,10}.

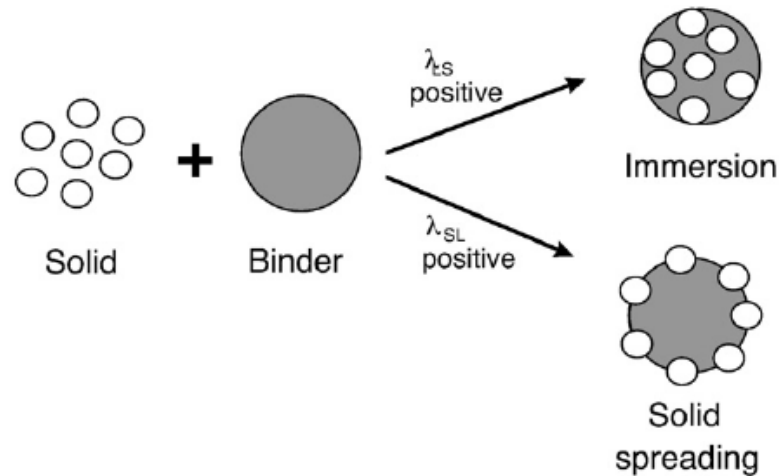


Figure 2.1.1 Nucleation mechanism for case when liquid drop size is larger than particle size. Adapted from Hapgood et al.¹⁰.

Granule nucleation is strongly affected not only by material properties but also the operating conditions of the granulator. The nucleation mechanism has been separated into a regime map developed by Hapgood et al.¹¹ The regime map, Figure 2.2, has three regions, drop controlled, mechanical dispersion, and an intermediate region. The author assumes that the binder is liquid and spray nozzles are the means of liquid addition. The regime map is separated by material properties on the vertical excess and equipment properties on the horizontal axis.

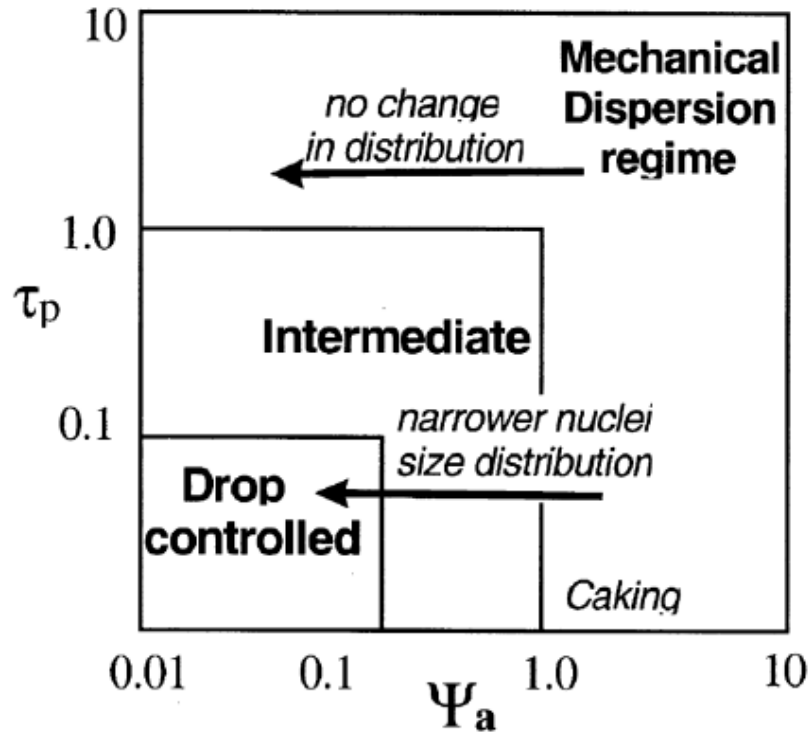


Figure 2.1.2 Nucleation regime map proposed by Hapgood et al.¹¹.

Eqn. 2.1 defines the dimensionless spray flux (Ψ_a). The dimensionless spray flux is a ratio of the flux of powder through the spray zone to the flux of the binder being sprayed on the region.

$$\Psi_a = \frac{3\dot{V}}{2\dot{A}d_d} \quad (2.1)$$

Where \dot{V} is the volumetric flow rate of liquid binder, \dot{A} is the flux of the particle bed surface in the spray zone, and d_d the average droplet diameter. At high dimensionless spray fluxes, the rate of liquid hitting the particle bed is large relative to the flux of the powder bed surface. This leads to drop overlap and mechanical dispersion in the bottom left of the regime map. The interaction of multiple drops has been observed

experimentally, and reduces control of the nucleation mechanism and has a large effect on the nuclei size distribution¹¹⁻¹³.

Eqn. 2.2 gives the ratio of the drop penetration time to the time required for a particle to make a cycle through the granulator back to the spray zone.

$$\tau_p = \frac{t_p}{t_c} \quad (2.2)$$

Where t_p is given by Eqn. 2.3:

$$t_p = 1.35 \frac{V_d^{2/3}}{\varepsilon_{eff}^2 R_{eff}} \frac{\mu}{\gamma_{lv} \cos \theta} \quad (2.3)$$

V_d is the volume of the droplet, ε_{eff} is the powder bed porosity, R_{eff} is the effective radius of pores in the bed, μ is the fluid viscosity, γ_{LV} is the liquid surface tension, and Θ is the dynamic contact angle between the liquid and solid. The drop penetration time is a function of the particle, particle bed, and liquid binder properties. It should be noted that this equation predicts that the drop penetration time is directly proportional to the binder viscosity. This means that for high viscosity or semisolid binders, the nucleation and wetting is likely within the mechanical dispersion regime regardless of the granulator operating conditions.

A large and robust body of work exists either characterizing the drop controlled regime or regime map separation^{9,10,13-18}. Research has focused on this area because operation in the drop controlled regime gives better control over granules and granular properties¹¹. However, mechanical dispersion is not always avoidable. A few studies have focused on mechanical dispersion regime along both axial extremes of the nucleation regime map.

Wildboer et al.¹⁷ explored the effect of over-wetting using Monte Carlo to predict droplet distribution obtaining a Poisson distribution. This was extended by Hapgood et

al.¹⁸ The authors validated the model for spray fluxes in the drop controlled nucleation regime, but found poor agreement at higher spray fluxes. This error was attributed to the presence of a bimodal distribution in the experimental data at large spray fluxes that the Poisson distribution does not predict.

Foam granulation has been explored and under some conditions is classified as mechanical dispersion^{19,20}. These studies focus on the effect of the bed penetration time of foam. The penetration time was found to behave as mechanical dispersion with high quality foam that would not penetrate the powder bed. However, these results do not apply to semi-solid binders which are discrete dense pastes.

Solid and semi-solid binders are used in melt granulation²¹. Typically melt granulation is used in fluidized bed granulators. The binder melts in the hot fluidizing gas and then forms nuclei. The process operates in the drop controlled regime where each binder particle melts and forms a nucleus. The nucleus then grows from coalescence with the surrounding material. Hounslow et al.²² proposed an immersion mechanism as the method of nucleation for single liquid drops applicable to melt granulation. In these cases the binder is not mechanically dispersed. Instead, the binder begins as a discrete droplets and form individual granule nuclei.

Schaefer et al. in a series of studies²³⁻²⁵ investigated melt granulation in a vertical high shear mixer. These parametric studies focused on agglomeration of pellets rather than mechanical dispersion of the initial binder droplets.

In a series of studies^{6,26-28}, Rough et al. used the same dry laundry materials as the case study for this thesis including the use of the semi-solid binder. These studies used a vertical high shear mixer to create granules. The results allowed the granulation of pastes

to be plotted on granulation regime maps for coalescence and growth and showed the evolution of bulk particle properties with time. However, the authors used limited characterization techniques including bulk and tap densities, and image analysis to place the granules on a series of regime maps for the other rate processes. Although the authors did measure particle size distributions, the mechanical dispersion of the binder was not studied or modeled.

None of these studies are able to provide insight into how to quantify and model the mechanical dispersion of a semi-solid binder. Melt granulation treats the binder as pre-nucleated and studies with similar materials were not robust. The mechanical dispersion of paste must describe how large pure binder particles are converted into smaller binder nuclei.

2.1.2 Consolidation and Coalescence

Consolidation and coalescence is the second rate process. It encompasses the mechanisms describing the way granules densify and agglomerate. Since granule size and porosity are very important properties in particle design, control over this rate process is very important in obtaining the desired product.

2.1.2.1 Consolidation

During consolidation a granule reduces its pore volume and increase in density. This occurs when granules are impacted by both other particles and equipment surfaces. After an impact a granule that is not perfectly elastic will retain some deformation. This deformation results in reduced pore volume in between the primary particles.

Several models have been proposed to model the consolidation process including both empirical²⁹ and theoretical models³⁰⁻³². In the empirical model proposed by Iveson²⁹, after a large number of impacts a granule will reach what is called the minimum porosity. This model is a three phase model that includes the solid, liquid, and gas volumes to calculate porosity. Eqn. 2.4 describes this process as an exponential decay in the porosity ϵ , based on number of impacts N . In this equation ϵ_{min} is the minimum porosity, ϵ_0 is the initial porosity and k is a fitting parameter.

$$\frac{\epsilon - \epsilon_{min}}{\epsilon_0 - \epsilon_{min}} = e^{-kN} \quad (2.4)$$

There are two theoretical models of consolidation². The first developed by Ouchiya and Tanaka³² focuses on capillary forces as the way the granules are held together. In this model, granules densify and the coordination number of the primary particles increases creating more liquid bridges between the primary particles. Eqn. 2.5 shows the rate of change in porosity (ϵ) as a function of compaction time (τ) and is a function of K_ϵ the dimensionless granule compaction rate that is inversely proportional to viscosity and surface tension. The resulting minimum porosity equation, eqn. 2.6, is dependent on the on the dimensionless granule compaction rate.

$$\frac{d\epsilon}{d\tau} \cong \left\{ 1 - \frac{(1-\epsilon)^3}{\epsilon} \frac{1}{K_\epsilon} \right\} \quad (2.5)$$

$$\frac{(1-\epsilon_{min})^3}{\epsilon_{min}} = \frac{1}{K_\epsilon} \quad (2.6)$$

Eqn. 2. 7 is the second theoretical model developed by Ennis et. al.³¹ This model uses the viscous stokes number St_v as the independent variable in the consolidation rate. The viscous Stokes number, eqn. 2.8, is a ratio of the impact forces to the viscous forces within the granule. The viscous forces from the binder have an important effect on

consolidation²⁹. To account for these forces, this model uses viscous dissipation as the primary source of energy dissipation in the granule. The model accounts for the viscous dissipation by proposing a string of particles connected by liquid bridges and determines the energy absorbed in the string due to viscous dissipation.

$$\frac{\Delta x}{h} = 1 - \exp(-St_v) \quad (2.7)$$

where Δx is the change in size, h is the thickness of liquid on the surface of the particles, and St_v is the Stokes deformation defined for a spherical particle as:

$$St_v = \frac{4\rho_g U_c d_g}{9\mu} \quad (2.8)$$

Where ρ_p is the granule density, U_c is the characteristic velocity, d_g is the granule diameter, and μ is the fluid viscosity. In this model, the amount of deformation (Δx) is an exponential function of viscous Stokes number. At high viscous Stokes number, the impact forces are much greater than the viscous forces and the model predicts a large amount of deformation. As viscosity increase, or the collision energy decrease, the viscous Stokes number is lower and the relatively larger viscous forces retard the deformation.

More recently, the immersion nucleation model 2 proposed by Hounslow et al.²² could be considered a consolidation model. In this model the authors propose that powder will be assimilated by an initial drop of liquid by repeated deformations. The form of this model is the same as that of eqn. 2.4 proposed by Iveson. However this model is a two phase model for liquid and solid whereas the Iveson model is three phase for solid liquid and gas. Eqn. 2.9 describes the size of the nuclei, v , at a given time t .

$$v \cong \frac{v_L}{\phi_{cp}} \left(1 - (1 - \phi_{cp}) e^{-\frac{12D_{eff}\phi_{cp}^{2/3}t}{h_0^2}} \right) \quad (2.9)$$

In this equation v_L is the volume of liquid, ϕ_{cp} is the volume fraction of the critical packing state, D_{eff} is the binary effective diffusivity, and h_0 is the half thickness of the nuclei. This expression is related to the consolidation of the nuclei. In the long time limit, the volume approaches the maximum nuclei volume of the volume of liquid divide by the critical packing fraction. This model is dependent on the diffusivity assumption which requires validation, and is not likely to be true for surfactant pastes since particles must be physically pushed into the paste rather than agglomerating through diffusion.

The importance of consolidation is primarily from its effect on granule internal structure. Granule porosity is a very important parameter in predicting the final properties of the granule and consolidation reduces the porosity. The reduction in porosity also reduces the available volume for liquid binder that is squeezed to the surface. The liquid binder on the surface promotes coalescence between other particles or granules.

2.1.2.2 Coalescence

During coalescence, two granules will combine into a new granule with the combined mass of the parent granules. The vast majority of models focus on binary collisions between particles of varying sizes³³⁻³⁶ (Figure 2.3). Whether or not two granules or particles will coalesce is determined by both the collision energy and the material properties. Material properties such as viscosity along with granule properties including yield strength, size and surface liquid, have a large effect on the coalescence mechanism.

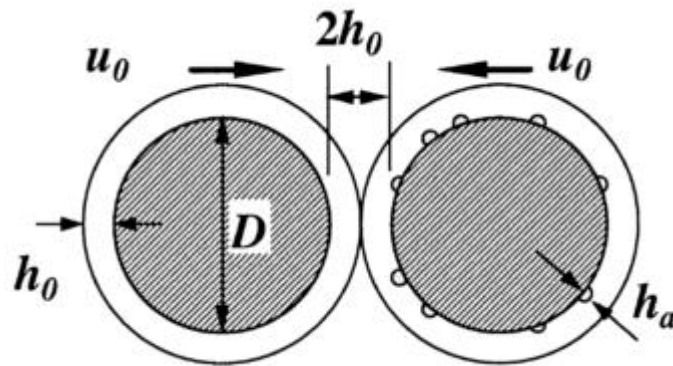


Figure 2.1.3 Schematic of two liquid bound granules coalescing adapted from Iveson et al 2001¹.

The availability of surface liquid is considered to be one of the most important parameters in determining both whether and how two particles will coalesce². Liquid can reach the surface of granules during coalescence if the internal pores are saturated leaving nowhere else for the liquid to go. The resulting granules are considered to undergo a binary collision resulting in the possibility of viscous dissipation, plastic deformation, and capillary bridge forces. Whether or not two granules will coalesce is dependent on the strength of these forces compared to the impact velocity. If the impact energy is sufficiently large, the particles will undergo consolidation and deformation, fail to coalesce, and rebound away from each other. To take the wide range of properties into account, a regime map, Figure 2.4, developed by Liu et. al.³⁴, has separated the process into two mechanisms, Type I and Type II coalescence.

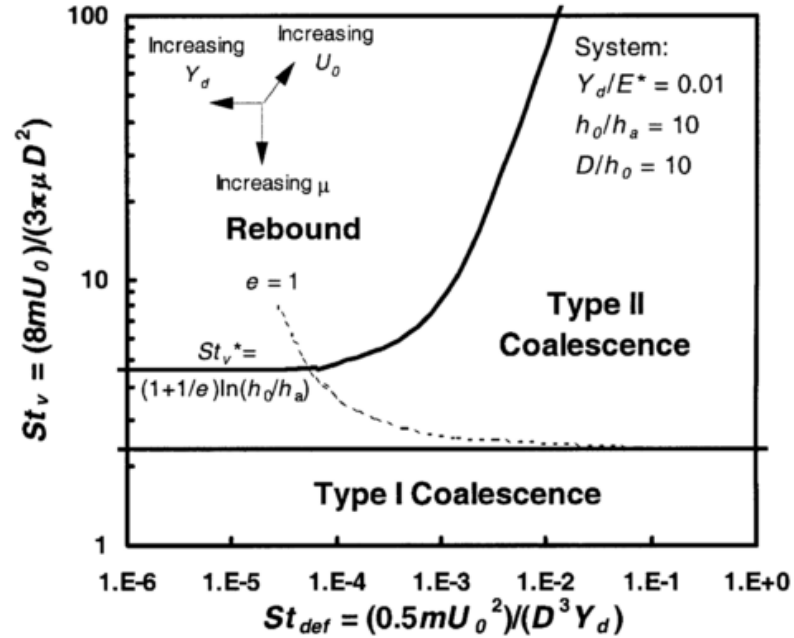


Figure 2.1.4 Regime map showing the solution to the coalescence mechanisms³⁴.

This regime map is quantified by the viscous Stokes number on the vertical axis and the Stokes deformation number on the horizontal axis. The Stokes deformation number, Eqn. 2.10, is a ratio of the strength of the granule to the energy of an impact. In this equation, m is the mass of the granule, U_0 is the impact velocity, D is the granule diameter, and Y_d is the yield stress.

$$St_{def} = \frac{mU_0^2}{2D^3Y_d} \quad (2.10)$$

The rebound region is where granules fail to coalesce due to a combination of weak inter-granular forces and high collision energy. Type I Coalescence occurs at low collision energy where the viscous dissipation is sufficient to stop the granule surfaces from coming into contact. In this case there is no deformation of the particles and a liquid bridge holds the two granules together. In Type II Coalescence, granule deformation plays a significant role in dissipating the kinetic energy of the collision. In this case,

particles do deform with the Stokes deformation number indicating the amount of energy absorbed. After the plastic deformation the resulting liquid bridge is enough to prevent the granules from separating keeping them coalesced.

Combining consolidation and coalesce together describes the growth of the granules during a granulation. Consolidation effects the porosity and liquid saturation that in turn allows for coalescence. Another regime map, Figure 2.5, developed by Iveson et. al.^{37,38} separates the growth mechanisms by maximum pore saturation and Stokes deformation number. The maximum pore saturation s_{\max} is a measure of liquid content compared to the total available pore volume and is an indicator of whether surface liquid will appear.

The regions on the map are separated by the availability of liquid and the strength of the granule or impact energy. At low amounts of liquid, the growth is either nucleation only, or dry free flowing. In the free-flowing region too little liquid is available for growth and granules are broken apart due to the high stokes deformation number. In contrast, all though the nucleation region also has too little liquid for coalescence and growth, the granules are strong enough to remain intact.

Once a sufficient amount of liquid is introduced growth can be achieved in either the induction or steady growth regime. In the induction growth, strong granules resist deformation and have a maturation time before liquid becomes available. Once liquid is available the coalescence and growth proceeds rapidly. In steady growth liquid is steadily brought to the surface allowing for consistent growth.

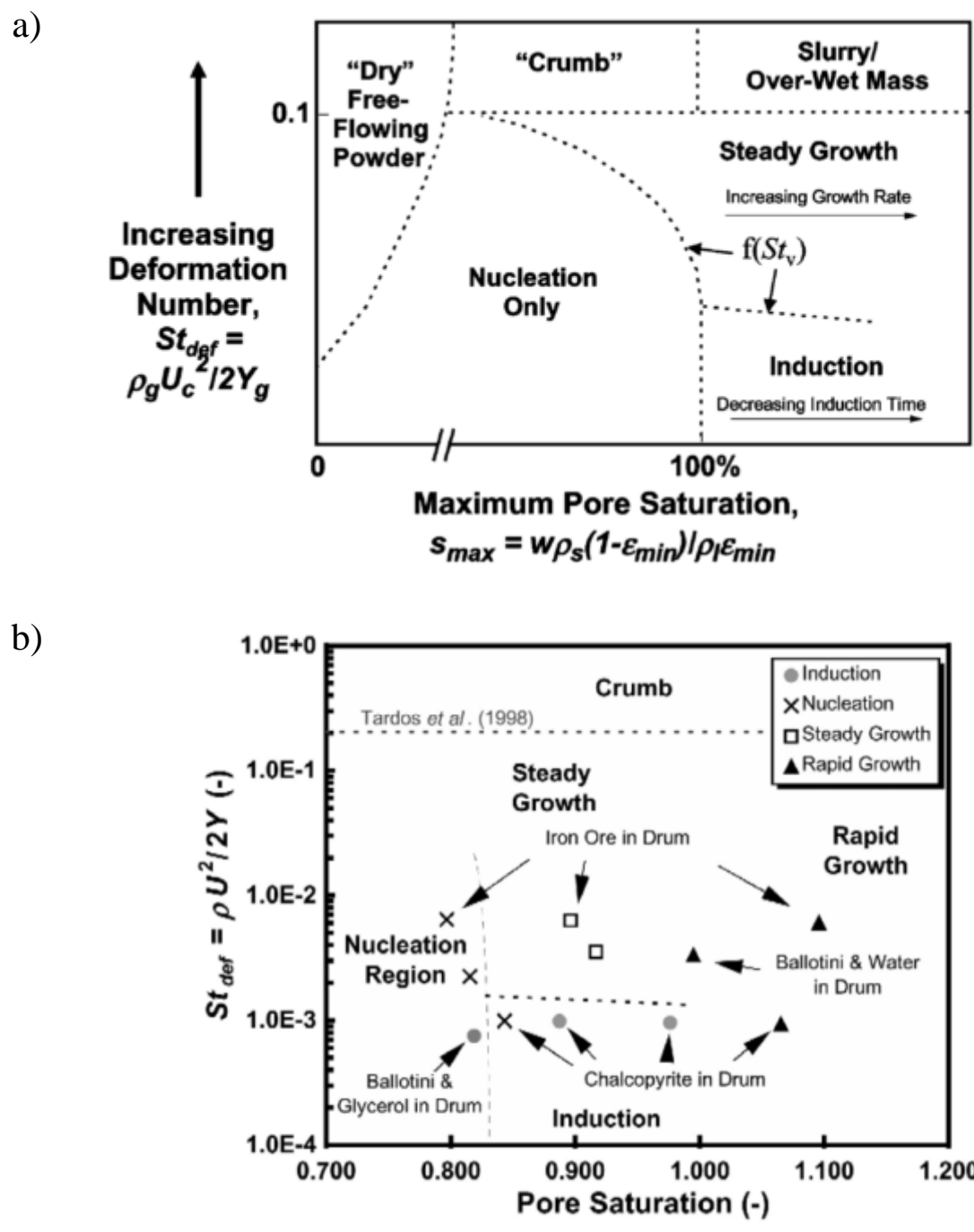


Figure 2.1.5 Growth regime map (a) and validated map (b) adapted from Iveson et al.^{37,38}

Finally, the Crumb and Slurry regions describe weak granules of high Stokes deformation number. With a large amount of liquid and weak granules the slurry region

is reached as discrete granules fall apart. In the crumb region granules rapidly coalesce and fall apart again without achieving a consistent granular product. In general steady growth is the most desirable region as it provides the greatest control over granular properties and is the most easily predictable.

2.1.3 Breakage and Attrition

Breakage and attrition are the rate processes that are responsible for reducing particle size. Breakage is primarily the fracturing of a larger particle into two or more smaller particles, while attrition is the abrasion of particles generating fines much smaller than the original particle. Iveson et al. (2001)¹ and Reynolds et al. (2005)³⁹ reviews several literature breakage theories encompassing several scales and focusing on different forces such as Van der Waals, capillary, and solid bridges. The majority of work cited in these reviews focus on the breakage of materials by crack propagation which is important for brittle or elastic particles.

The application of breakage models is very material specific. Breakage in brittle materials is described by crack propagation, Eqn. 2.11. This is the model pioneered by Rumpf et al.⁴⁰. In this equation K_c is the fracture toughness, T is a fitting parameter, σ_f is the applied stress, c is the crack length, and δ_c is the diameter of the process zone where the crack forms. This equation is useful for dry granules but not for wet granules with viscous and capillary forces¹.

$$K_c = T\sigma_f\sqrt{\pi(c + \delta_c)} \quad (2.11)$$

Tardos et al.¹², used the Stokes number to predict breakage. This model evaluates the Stokes deformation number, eqn. 2.12. In this version of the Stokes deformation number, τ_0 is the yield stress, γ is the shear rate, a is the particle diameter, and ρ_p is the

particle density. For this model the breakage of a particle occurs if the stresses of the particle exceed some critical stokes deformation number $St_{def} > St_{def}^*$. Additionally, granules are assumed to behave as Herschel-Bulkley fluids.

$$St_{def} = \frac{\rho_p a^2 \gamma^2}{2\tau_0} \quad (2.12)$$

For the case study in this thesis, the binder is a Heschel-Bulkely or Bingham plastic fluid. The methods developed by Tardos et al. can be easily applied to the surfactant paste binder of the case study. Using this model the mechanical dispersion of paste through the granulator is modeled as a breakage process. The conditions for breakage are defined by the critical stokes deformation number and is a function of the material properties.

Another model not included in these reviews developed by Vogel and Peukert (2003)⁴¹⁻⁴⁴ represents breakage as a probability function based on the Weibull distribution and coupled with a breakage distribution. In this paper, the authors demonstrate a method to use a modified hammer mill without a screen to break a large number of particles in a way that mimics a single particle breakage test. The multiple particle breakage greatly reduces the amount of time necessary to complete a representative sample. This model is primarily useful for granules that will easily fragment instead of undergo attrition. However, the experimental protocol to mimic single granule experiments is very useful.

Other breakage models exist based on correlations and various first principle models. Bika et al.⁴⁵ summarizes many of them. These models make various improvements for specific granule cases but are not necessary to go into full detail.

However, the author does point out the use of the Herschel-Bulkley model for fluids as a method for characterizing wet agglomerate strength.

2.1.4 Rate Processes Summary

A large number of models have been developed for the various rate processes. So far no standard practice has been developed to decide which model to use. Many of these models use assumptions, such as binary collisions, that may be quite poor in an actual granulator. The literature has shown that isolating rate processes is an important step in developing physical models. Although some work has been done with the materials of interest, no model for mechanical dispersion of a semi-solid binder has been developed. Tardos et al. showed that granule breakage occurs when the Stokes deformation number exceeds a critical limit. This can readily be applied to the binder in the case study and define the rate of mechanical dispersion as a breakage rate.

2.2 Population Balance Modeling

2.2.1 Population Balance Model Theory

Population balance models are state of the art for granulation models^{46,47}. In granulation, population balance models (PBMs) keep track of the number of granules, or particles, in the system. Granules are classified based on one or more independent variables such as particle size for 1D models and volume of solid, volume of liquid, and volume of air for 3D models. The population balance equation, eqn. 2.13, 2.14, is analogous to a mass or energy balance but for the case of a discrete population.

rate of change in number of particles with distributed property value $v = in -$

$$out + gen + (birth - death) \quad (2.13)$$

$$\frac{\partial Vn(v,t)}{\partial t} = \dot{Q}_{in}n_{in}(v,t) - \dot{Q}_{out}n_{out}(v,t) - V \frac{\partial(G^*-A^*)n(v,t)}{\partial v} + V(\dot{b}(v)_{nuc} + \dot{b}(v)_{coal} + \dot{b}(v)_{br} - \dot{d}(v)_{coal} - \dot{d}(v)_{br}) \quad (2.14)$$

$n(v, t)$ is the number of particles with distributed property v . \dot{Q}_{in} is the flow rate of particles into the system, \dot{Q}_{out} is the flow rate of particles out of the system. The third term is the steady growth term with G^* as the growth rate and A^* as the attrition rate. The population balance deals with discrete entities instead of a continuum. Therefore, it is possible for two individual granules to coalesce into a new granule. The new granule will be “born” and added to the population while the two older granules will cease to exist, “die” and be removed from the population. Birth, $\dot{b}(v)$, can happen due to nucleation, coalescence, or breakage while death, $\dot{d}(v)$, only occurs due to coalescence of smaller particles or breakage of larger particles.

There has been moderate success in developing population balance kernels describing breakage. Eqn. 2.15 and 2.16 show the general forms of the breakage kernel.

$$\dot{b}(v)_{br} = V \int_v^{\infty} \phi(u, v) K_{break}(u) n(u) du \quad (2.15)$$

$$\dot{d}(v)_{br} = -V K_{break}(v) n(v) \quad (2.16)$$

where $\dot{b}(v)_{br}$ is the birth rate and $\dot{d}(v)_{br}$ is the death rate of particles of volume v per unit volume, V is the volume of the system, $\phi(u, v)$ is the fraction of particles of size u that break into size v , $K_{break}(u)$ is the breakage rate of particles of volume u , $n(u)$ is the number of particles of volume u . The left hand side of the equation is integrated by particle volume over the entire domain of particles from the volume of the daughter particle v to the largest size in the domain.

Table 2.1 is non exhaustive list of proposed breakage kernels used in granulation models. The size independent, product type, sum type, sum of powers, and discrete

homogeneous are all empirical correlations using various functions of particle size to model particle breakage. They contain many fitting parameters which make them poor at predicting particle breakage a priori. The Semi-empirical and Austin models contain some physical emphasis such as shear rate or the size adjustment parameters. The mechanistic breakage kernel, Vogel & Peukert, and Capece models all use some physical description of breakage to develop the population balance kernel.

The Vogel & Peukert and Capece kernels both use fracture mechanics as a basis of deriving the population balance kernels. Particles are said to be able to break if the impact energy is greater than the internal strength of the material to resist breakage. In fracture mechanics this is a function of the number and size of the flaws in the particle which is size dependent. However, particles fracturing due to crack propagation may be a poor model for soft wet agglomerates typical in granulation. Other models exist in the literature for the breakage of hard materials, however they are beyond the scope of granule breakage.

Picking the appropriate breakage kernel to use in population balance modeling for granulation is still difficult. There is currently no formal approach for deciding which set of kernels to use in population balance modeling. Additionally, the large variety of granulator types and granulation make it difficult to develop a singular kernel useful for all granulation conditions.

Table 2.1 Proposed breakage kernels in the literature. Expanded from Kumar et al. 2013⁵

Kernel Name and Parameters	Equation Particle size given by (z)
Size Independent	$K_{break}(z) = constant$
Semi-empirical breakage kernel: ⁴⁸ G: shear rate, D: diameter P ₁ , P ₂ : fitting	$K_{break}(z) = \frac{P_1 G_{shear} (D(z))^{P_2}}{2}$
Product type: ⁴⁹ B : beta function v(y): y > 1 number of paste fragments q > 0, parameter	$K_{break}(z) = \frac{z^{q-1} (1-z)^{q(v-1)-1}}{B(q, q(v-1))}$
Sum Type: ⁵⁰ B : beta function, v(y): y > 1 number of paste fragments q > 0, parameter	$K_{break}(z) = \frac{z^{q-1} (1-z)^{v-2}}{B(q, v-1)} + (v-1) \frac{(1-z)^{q+v-3}}{B(1, q+v-2)}$
Sum of Powers: ⁵¹ c _i : fitting parameter k _i : power fitting parameter	$K_{break}(z) = \sum_{i=1}^n c_i z^{k_i}$ with $\sum_{i=1}^n \frac{c_i}{k_i+2} = 1$ -2 < k _i < inf
Discrete homogeneous ⁵² c _i : fitting parameter a _i : fitting parameter	$K_{break}(z) = \sum_{i=1}^n a_i \delta(z - c_i)$
Mechanistic Breakage: ⁵³ F : particle density WA : total wall surface area SA : particle surface area IA : impeller surface area N _a = Avogadro's constant Z _{a,upper} = upper limits on volumes	$K_{break}(z_a) = \sum_{z_a=1}^{z_{a-upper}} \frac{\sigma_{ext}^{particle}(z_a, z_b)}{\sigma_{int}(z_a)} F(z_a) N_a \frac{SA(z_a)}{SA+WA+IA} + \frac{\sigma_{ext}^{wall}(z_a)}{\sigma_{int}(z_a)} \frac{WA}{SA+WA+IA} + \frac{\sigma_{ext}^{impeller}(z_a)}{\sigma_{int}(z_a)} \frac{IA}{SA+WA+IA} + \frac{\sigma_{ext}^{fluid}(z_a)}{\sigma_{int}(z_a)}$
Vogel & Peukert ⁴¹ : k _{break} : breakage fitting constant f _{Mat} : mass based strength parameter k : number of impacts W _{m,kin} : mass specific impact energy W _{m,min} : minimum energy required for particle breakage	$K_{break}(z) = k_{break} \left[1 - e^{-f_{Mat} k z (W_{m,kin} - W_{m,min, z})} \right]$

Table 2.1 Continued

Kernel Name and Parameters	Equation Particle size given by (z)
Capece⁵⁴: f_{Mat} : material strength parameter $f_{coll,l,z}$: collision/impact frequency $E_{m,kin}$: mass specific impact energy $E_{m,min}$: threshold impact energy L : total number of energy bins i : size index t : time index	$K_{break}(z_{i,t}) = f_{Mat} z_{i,t} \sum_{l=1}^L f_{coll,i,l,t} (E_{m,kin} - E_{m,min,i})$
Austin (1984)⁵⁵: $z_{critical}$: critical particle size μ : size adjustment parameter a : constant rate of breakage α, Λ : fitting parameters	$K_{break}(z) = \begin{cases} a \left(\frac{z}{z_{critical}} \right)^\alpha \left(\frac{1}{1 + \left(\frac{z}{\mu} \right)^\Lambda} \right) & \text{for } z \geq z_{critical} \\ 0 & \text{for } z < z_{critical} \end{cases}$

The kernels shown in table 2.1 are all for one dimensional population balance models based on the size of the particles. The 1 dimensional population balance model can only keep track of one parameter of the population typically size (z) or volume (v). The limit of 1D population balance models is higher order interactions in the population can only be functions of the population parameter or time.

The limits of 1D size has been a concern for many years⁵⁶. Differences in the population of granules such as liquid content and porosity are known to have a large effect on granulations. These attributes of granules require a higher order population balance model to adequately develop predictive models of granulation. However, the ease of developing a 1D population balance model has seen their continued use in appropriate systems such as milling breakage^{42,57}.

Computational time is a major limitation on multidimensional population balance modelling⁵⁸. Increasing the number of dimensions has a power affect increase on the number of bins in the solution space. Additionally, while the one dimensional population

balance model has been solved⁵⁹, the numerical methods used to solve the population balance equation is also important. A review of numerical methods are beyond the scope of this literature review but should be understood before applying multidimensional population balance models. Despite these limitations, there are several studies on multidimensional population balance models and kernels^{53,58,60-66}. The results have shown an improved ability to account for granule properties and improved ability to predict the transient granulation population.

2.2.2 Multiscale and Compartment Modeling

Applying population balance models to entire granulators is challenging. Multidimensional population balance models allow the properties of the granules to be included in the process model. However, different regions within the granulator may result in different rate process or different rate process intensities i.e. a mill for breakage or a spray zone for wetting and nucleation. The discrete nature of particles also makes particle-particle interaction and particle flow from region to region difficult to model. These weaknesses of population balance modeling have been addressed by using multiscale and/or compartment models³.

Multiscale modeling is the method of using multiple computational simulations to describe different levels of material interactions. The interaction of material at the particle level is difficult to describe with a physical model using population balance models alone. Discrete Element Method (DEM) models or Computational Fluid Dynamics (CFD) models can be used to describe the flow of material within a granulator. Additionally, if the granulator is divided into multiple compartments the flow between

compartments can be approximated from these models. DEM models can also be used to determine the stress or collision of material within a process.

Compartment modeling is the method of dividing the equipment to be modeled into several regions where particles experience similar rate processes. This is commonly done heuristically by examine the equipment and separating the rate process by region i.e. breakage occurs near the chopper. An alternative to a heuristic division is to divide the population of particles into compartments based on particle attributes such as velocity, or whether particle surface is exposed to the spray zone⁶⁷.

Freireich and Li in a series of papers developed a 1D population balance compartment model for a coating process in a Forberg mixer. The authors used DEM models to describe quantify the flow of particles within the mixer. The divided the mixer into two regions, spray region and bed region as seen in figure 2.6. The spray region is defined by calculating which particles have exposed surface area to the spray and is modeled a single continuous stirred take reactor (CSTR). The bed region is defined as all the remaining particles and is modeled as a series of CSTR's each with its own population balance equation. The authors found good agreement between the particle coating population balance model and experiments. This case is simpler than granulation since coating is the only rate processes.

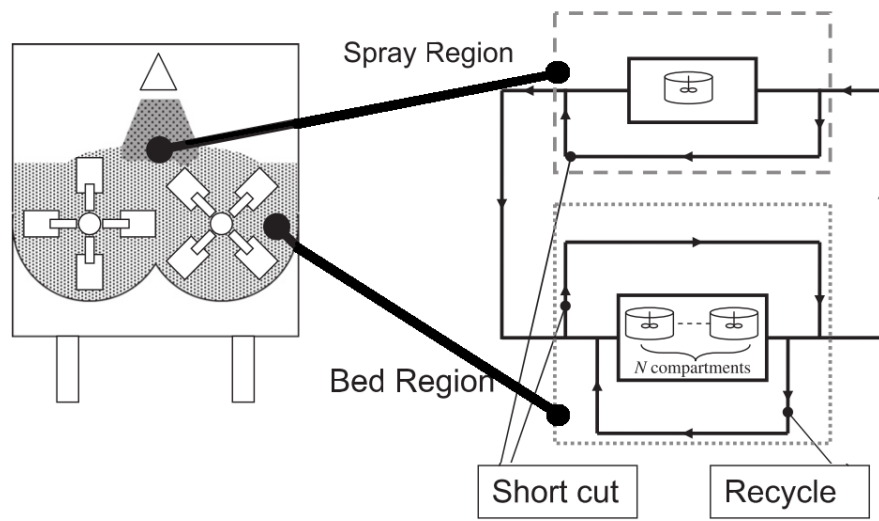


Figure 2.2.1 Forberg mixer coater and compartment model adapted from Li et al 2011⁶⁸.

In addition to the Forberg mixer, there are several attempts in the literature to complete multiscale compartment models of granulators and coaters. Table 2.2 summarizes many of these attempts.

Table 2.2 Summary of multiscale population balance models in the literature.

Particle Equipment	Modeling Techniques	Rate processes
Forberg mixer coater	DEM, 1D PB, compartment	Layering/coating
Vertical high shear mixer Xi Yu ⁶⁹	CFD, Monte Carlo, 2D PB multi compartment	Nucleation, coalescence, breakage
Spheronizer Bouffard et al. ⁷⁰	DEM, Monte Carlo, 1D PB 3 compartment	Nucleation, agglomeration, breakage
Fluid bed granulation Börner et al. ⁶⁴	1D PB 2 compartment	Nucleation, Layering/growth
Fluid bed granulation Liu et al. ⁷¹	CFD 1D PB 2 compartment	Nucleation, Aggregation, Breakage
High Shear Granulator Chaudhury et al. ⁷² Barrasso et al. ⁷³	Coupled DEM-PB 3D PB Multi compartment	Nucleation, Agglomeration, Breakage

Recent work at the University of Sheffield by Xi Yu⁶⁹ has developed a compartment model for a vertical high shear mixer. The five compartments are defined heuristically with an impeller, spray, chopper, and 2 bed zones. This compartment model uses CFD to determine flow fields, and Monte Carlo simulations to determine the residence time distributions of the compartments. The population balance is 2D with solid volume and liquid volume as the distributed parameters. The model includes nucleation, coalescence, and breakage rate processes, but neglects growth.

Bouffard et al.⁷⁰ developed a compartment model for a spheronizer. The spheronizer geometry is simpler than the vertical high shear mixer. The model has three compartments, shear, bulk, and wetting zone. DEM is used to obtain particle flow information and a Monte Carlo based PBM model to model the compartments.

Several authors have studied multiscale modeling of fluid bed granulators^{64,71,74-76}. Börner et al.⁶⁴ developed a compartment model for a Wurster fluidized bed granulation. This model obtained particle flow information using a first principles gas velocity solution and validated using image analysis. The Population balance is 1D with particle size as the distributed variable. The model uses two compartments to separate the fluid bed granulator. More recent models such as by Liu et al.⁷¹ have improved on earlier work producing more predictive models. However, these models are not very useful for a direct comparison to the case study because it is low shear.

Chaudhury et al.⁷² and Barrasso et al.⁷³ developed models for high shear granulation. This model is unique in that it uses a coupled DEM-PM simulation with a 3D population balance model. The DEM simulation provides collision information to the population balance model which then returns breakage and agglomeration information. The DEM then updates the simulation population size using the information. This model allows the DEM simulation to provide up to date information to the population balance model. The models are very complex but are able to capture the largest amount of physical information. However, calibrating the model can be difficult and the results may be very sensitive to the DEM simulation which was not validated.

The multiscale compartment models establish the feasibility of implementing a multiscale compartment model for granulation. The literature shows that both single and multi-dimensional population balances are reasonable along with DEM, Monte-Carlo, and CFD models. However, validation remains a key concern since often the DEM or CFD models are not independently validated. Additionally, the large number of equations and compartments introduce a large number of fitting parameters that reduce the

predictability of the model. The studies show that simpler systems such as coaters are produce more confident and simpler models. The complex granulation models were not simplified and validated to study single rate processes independently.

2.3 Discrete Element Method Modelling

Discrete Element Method (DEM) is a modeling technique used to simulate the motion of a large number of particles. In a DEM simulation individual particles are given a mass, size, and a set of initial conditions for translational and angular velocity. The simulation then solves the Newtons' laws of motion for the complete population of particles for a series of time steps to generate particle flow information. DEM modeling has become increasingly popular over the last few decades partially due to increasing computer power but also due to the availability of relatively easy to use software such as EDEM, Figure 2.7, and LIGGGHTS to build models. DEM models provide detailed information on the particle level. Information from a DEM model can include velocities, kinetic energy, collision frequency, and other particle scale information.

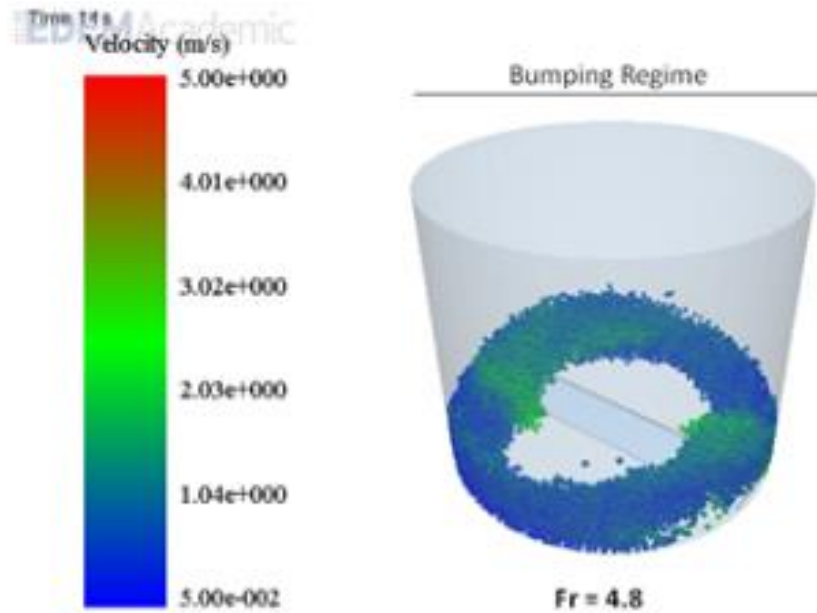


Figure 2.3.1 DEM Vertical High Shear Mixer system in EDEM.

DEM models have been used to study a large number of particle systems including granulators, fluid beds, mixers, and individual particles⁷⁷. These models derive a variety of information from the DEM simulations. A non-exhaustive list includes modeling of rate processes^{78–81}, granular mixing^{81–83}, particle coating^{67,84}, particle flow information^{81,85–87}, and scale up⁸⁸.

DEM models rely on underlying contact models to determine how particle will behave in contact. These models typically follow the soft-sphere spring and dashpot interaction first developed by Cundall and Strack⁸⁹. The soft sphere model allows for particles to overlap where a hard-sphere model prevents particle overlap by applying a force to keep the particles from overlapping. The collision model consists of both normal and tangential forces combined to form an overall particle-particle interaction Figure 2.8. Both the normal and tangential forces can be described as spring and dashpot with the

total force in each direction being the sum of both a linear spring for elastic repulsion, and a linear or non-linear viscous damper for viscous dissipation eqn. 2.17.

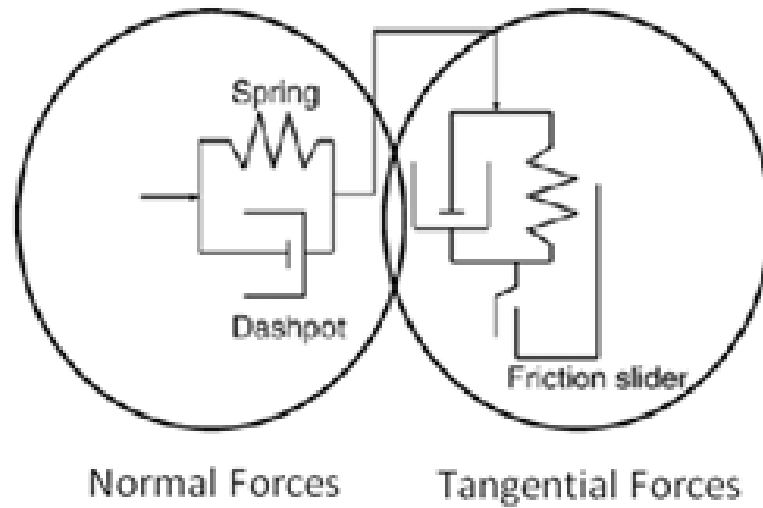


Figure 2.3.2 Normal and tangential forces shown together using spring and dashpot models for each and a friction slider in the tangential direction. Image adapted from Gantt et. al. 2006⁷⁸.

$$\vec{F}^n = \vec{F}_{el}^n + \vec{F}_{diss}^n \quad (2.17)$$

A large number of models have been reviewed for both normal forces and tangential forces⁹⁰⁻⁹³. These models provide various improvements of the Cundall and Strack model, including physically meaningful parameters, at the cost of greater complexity. These collision models use various types of spring and dashpot types to create summarized in Table 2.3. Notably, Hertz theory, or Hertzian Springs, are often used in granular modeling for elastic primary particles that tend to have high coefficients of restitution of restitution. The specific equations for each model is beyond the scope of this review.

Table 2.3 Collision Model types and examples. Adapted from Stevens et. al. 2005⁹² and Freireich et. al. 2009⁹⁴.

Spring Type	Particle Regime	Examples
Linear Spring	Empirical	Cundall and Strack ⁸⁹
Hysteretic Spring	Elastic-Plastic	Walton and Braun ⁹⁵ , Thornton ⁸⁰
Hertzian Spring	Viscoelastic	Lee and Herrmann ⁹⁶ , others ⁹⁷⁻¹⁰⁰
Hertzian spring	Viscoelastic	Kuwabara and Kono ¹⁰¹ , others ^{102,103}
JKR improved Hertz	Elastic	Johnson Kendall Roberts ¹⁰⁴
DMT improved Hertz	Elastic	Derjaguin Muller Toporov ¹⁰⁵

Unfortunately, current computational limits put a limit on the number of particles that can be simulated in a reasonable time. While typical lab scale granular systems have a minimum number of particles on the order of 10^9 . Current simulations are capped at around 10^6 particles. This discrepancy has been avoided by both decreasing the size of the simulation domain and by increasing particle size.

Decreasing the size of the simulation domain has been achieved by dividing the larger system into periodic segments¹⁰⁶. The segment or “unit cell” is given periodic boundary conditions. Figure 2.9 shows the breakup of a granule in a 2D shear field developed by Tardos et al.¹⁰⁶ In this model the granule is modeled by a combination of primary particles with liquid bridge forces holding the granule together. At high stokes deformation numbers, the granule shears apart while at lower values it merely deforms. The unit cell here provides information to the higher level models. The model is only 2D limiting the use in 3D models. Additionally, the use of a liquid binder network to hold the granule together is difficult to calibrate.

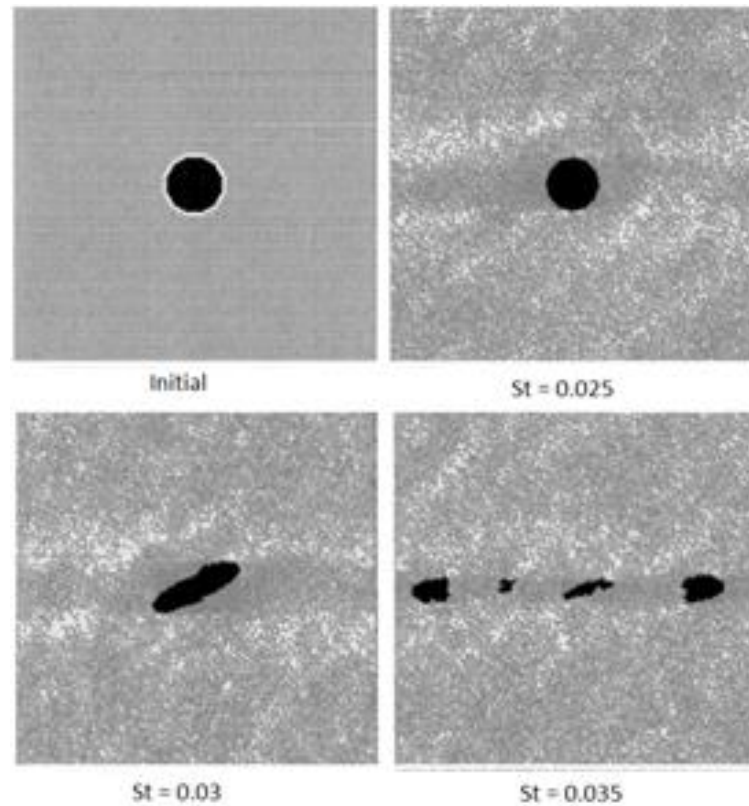


Figure 2.3.3 DEM 2D shear cell showing granule breakup at high Stokes deformation numbers. Adapted from Tardos et al. 2000¹⁰⁶.

Similar to the work by Tardos, Adams et al 1998⁸⁰ used DEM to coalesce two granules figure 2.10. These granules are also constructed out of primary particles connected by liquid bridges. These DEM models are both models of rate processes. Simulations like these can be used to obtain information for the rate processes. However, it is important that proper validation is completed on the DEM model.

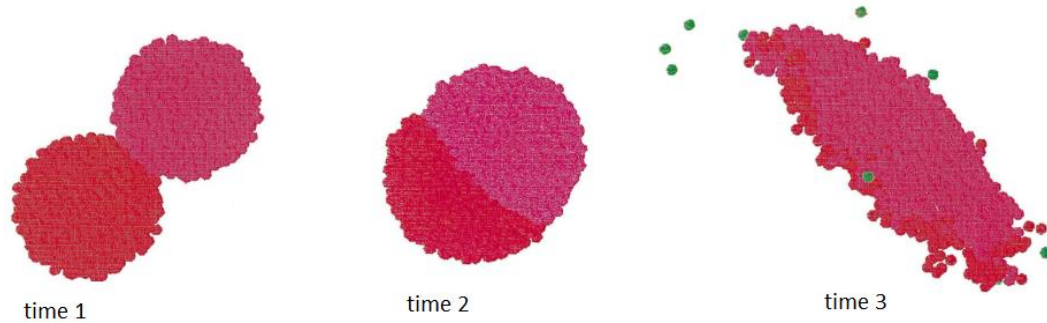


Figure 2.3.4 2D coalescence of granules. Adapted from Adams et al. 1998⁸⁰

DEM simulations have also been used to look at the development of stress in a particle bed. In a series of studies by Ghadiri and collaborators^{85,107–109}, the authors studied the hydrostatic and deviatoric stress in sheared medium. The authors studied a unit cell within a granulator and determined the mean deviatoric and hydrostatic stress in a series of regions in the granulator. Characterizing the stress on the particle population is important since particle stress, velocity, and particle-particle interactions form the basis of the rate processes in granulation.

The results showed the effect of position and operating conditions on the stress. The results provided a good foundation for further work examining the stress on granules in powered beds. However, the authors only examined low strain rates far below what is observed in typical granulations. Additionally, validation of shear rates in high shear granulators is difficult was not completed in the studies.

In addition to direct rate process modeling, DEM modelling has also been used to obtain population balance kernel information.^{54,55} In this case, Cameron et al use DEM data to obtain the collision rate within a slice of a vertical high shear granulator. The collision rate is used in the coalescence kernel to calculate the rate of agglomeration. The DEM model uses a very dilute particle phase at low RPM making it an unrealistic

simulation. In addition, these simulations have the same issue as the previous unit cell models, i.e. the models use collision scale data that is not validated.

Freireich et al 2009⁹⁴, performed a sensitivity analysis on a DEM data for a rotating drum. The results showed that bulk properties such as velocity flow fields were insensitive to the simulation parameters. However, collision scale data are strongly affected by parameter variance. Because of these results, it is important to validate the DEM model at the scale that the information is going to be gathered.

DEM model validation typically compares particle flow fields in an experimental system with those generated in the simulation. Positron emission particle tracking (PEPT) has been used to statistically determine the special residence times of particles by comparing the simulation to special data of a single particle in a running granulator^{110,111}. In this method an irradiated particle is added to a granulator and the radiation is detected to determine the particle position. After a large measuring time it is assumed that the particle has occupied all available regions and the positional frequency can be compared to a DEM simulation. Another method uses image analysis either by direct measurement of particle velocities⁸⁴ or by color labeling of particles^{82,83}. However, these methods focus on the macroscopic easily measured properties of the particle bulk powder. The validation of macro level trends such as particle flow does not validate the particle scale behavior such as collision frequency⁹⁴. It is important to attempt to validate DEM simulations at the same physical scale as the data of interest.

An important use of DEM modeling is developing particle flow information and residence times in granulator equipment for compartment models. DEM was used by several of the compartment models mentioned in section 2.2.2. DEM simulations are

ideal for these models since they can provide macroscopic position information that is more readily validated than the particle level information.

For example, Freireich and Li used DEM to obtain the flow rates in their compartment model.⁶⁷ This was made easy by having a 1:1 ratio between the number of particles in the simulation and the number of particles in the experimental set up. To use this method in systems where the particle number ratio is not equal, the required data would be in terms of mass fraction instead of number of particles.

2.4 Literature Review Summary

The review of the literature applicable to the case study has revealed several opportunities for deeper investigation. The key findings of this review are:

1. Previous work using the same materials as the current study focused only on qualitative regime mapping and not modeling. The rate process of mechanical dispersion has not been explored in the literature for materials that behave like a semi-solid. The experiments did not isolate individual rate processes and revealed a hole in the physical understanding of the mechanical dispersion process. The case study geometry of the pin mixer is a geometry that is understudied in the literature compared to twin screw granulation and fluid bed granulation.
2. There are a large number of breakage kernels for population balance models in the literature. Several of these have been demonstrated to successfully model breakage in the granulation process. However, many of these models are empirical and do not use either material properties or operating parameters of the equipment. Development of a mechanistic model will require the use of both.

3. Compartment models have been demonstrated as a powerful combination of tools in granulation modeling. However, many recent attempts try to combine too much into a single model that is difficult to validate. Many studies have focused on implementing DEM into population balance models. These models typically use unit cells of real granulators that are difficult to validate. Obtaining particle scale data using a model that can be validated is necessary to improve confidence in the model.

Each of these gaps in the literature correspond to the thesis objectives described earlier indicating their importance and novelty.

CHAPTER 3. MECHANICAL DISPERSION OF SEMI-SOLID BINDERS IN HIGH SHEAR GRANULATION

3.1 Introduction

In this chapter, the mechanical dispersion of a semi-solid surfactant paste is examined. As described in the literature review, mechanical dispersion is an important but understudied rate process in granulation. The objective of this chapter is to identify the mechanism of mechanical dispersion and determine the important parameters governing the rate process. The objective is achieved by:

1. Derivation of a mechanistic and physically based model of mechanical dispersion in the pin mixer.
2. Characterization of the materials used in detergent granulation including the powder size and density, and the yield stress of the surfactant.
3. Development of an experimental procedure that isolates mechanical dispersion from the other rate processes.
4. Identification of the important parameters governing mechanical dispersion.

Two surfactants with different rheological properties are compared. It is hypothesized that mechanical dispersion can be treated as an impact breakage process. In this mechanism, granule nuclei are hit by the fast moving impeller causing a size reduction of the initial binder inlet stream.

3.2 Theory

Semi solid binders such as those used in detergent granulation cannot be atomized using a spray nozzle. For these materials the binder must be mechanically broken into granule nuclei that are agglomerated into the product granules. In detergent granulation the mechanical dispersion of the semi-solid binder can be accomplished in a pin mixer. This geometry uses high speed pins to break up the incoming stream of binder into nuclei.

The breakage of semi-solid surfactants into nuclei may possibly occur through two mechanisms, impact or shear. The impact mechanism describes binder particles being physically hit by the pin and breaking apart. The shear mechanism describes binder particles breaking due to the shear stress applied in annular region of powder flow and particularly in the small gap between the pin tip and the wall. Both of these mechanisms are governed by the rotational speed of the granulator. A high impeller speed will increase both the number of impacts per unit time and the intensity of both impacts and the shear field in the area around the pins. Consider breakage by impact with the pin. The breakage rate is:

$$K_{break} = \dot{N} * \eta * P_{breakage} \quad (3.1)$$

where K_{break} is the breakage rate (breakage selection function), \dot{N} is the number of times an impeller passes a point in the granulator per unit time, η is the probability of impact occurring for each impeller pass, and $P_{breakage}$ is the probability of breakage given that an impact has occurred. \dot{N} will be a function of the impeller geometry and proportional to the angular velocity of the pin ω . During a rotation of the impeller a single paste particle has the opportunity to experience a maximum of 4 pin impacts since the granulator impeller has 4 groups of pins offset at 90° . Therefore:

$$\dot{N} = 8\pi\omega \quad (3.2)$$

3.2.1 Probability of breakage given an impact has occurred

It is postulated that breakage will occur if the stress applied to a paste particle during impact with the pin exceeds the plastic yield stress of the particle. Kousaka¹¹² evaluated the breakage of agglomerate in a fluid flow by both shear and impact. The model assumes spherical particles and produces a relationship for the maximum tensile stress through the plane going through the particle center which is the maximum tensile stress in the particle.

$$\sigma = \frac{2}{3}\rho_p d_p \left(\frac{v_i}{t_p} \right) \quad (3.3)$$

where ρ_p is the density of the agglomerate, d_p is the diameter of the agglomerate, v_i is the velocity of the impact, and t_p is the impact time. This equation can be used to determine the stress on a particle due to impact at a velocity of v_i . According to Tabor¹¹³, the impact time Δt will be dominated by the plastic flow of the deformable material. This time can be calculated using the equation derived by Tabor for a spherical particle:

$$t_p = \frac{1}{2} \sqrt{\frac{\pi M}{p d_p}} \quad (3.4)$$

where M is the mass of the particle which can be determined using the volume and density of the spherical particle, p is the mean contact pressure, and d_p is the diameter of the particle. The pressure p is the contact force, F , divided by the contact area, A :

$$p = \frac{F}{A} \quad (3.5)$$

The contact force is can be defined as the impact velocity divided by the impact time t_p . If the contact area is assumed to be the circle of radius a that defines a spherical cap of height h , then the equation for pressure becomes:

$$p = \frac{Mv_i/t_p}{\pi a^2} \quad (3.6)$$

where a^2 is given by:

$$a^2 = d_p h - h^2 \quad (3.7)$$

The height of the cap h is equal to the tip speed multiplied by the impact time:

$$h = v_i t_p \quad (3.8)$$

resulting in a final equation for the contact pressure:

$$p = \frac{M}{\pi t_p^2 (d_p - v_i t_p)} \quad (3.9)$$

Substituting from eqn. 3.9 for pressure into eqn. 3.4 for the impact time gives:

$$t_p = \frac{1}{2} \sqrt{\frac{\frac{\pi M}{M}}{\frac{M}{\pi t_p^2 (d_p - v_i t_p)} d_p}} \quad (3.10)$$

which reduces to:

$$t_p = \left(1 - \frac{4}{\pi^2}\right) \frac{d_p}{v_i} \quad (3.11)$$

Substituting for t_p from eqn. 3.11 into eqn. 3.3 for tensile stress gives:

$$\sigma = \frac{2}{3} \left(1 - \frac{4}{\pi^2}\right)^{-1} \rho_p v_i^2 \quad (3.12)$$

Thus, breakage will occur if:

$$\sigma = \frac{2}{3} \left(1 - \frac{4}{\pi^2}\right)^{-1} \rho_p v_i^2 > \tau \quad (3.13)$$

Rearranging:

$$St_{def} = \frac{\rho_p v_i^2}{2\tau} > \frac{3}{4} \left(1 - \frac{4}{\pi^2}\right) = 0.45 \quad (3.14)$$

Eqn. 3.14 describes of the probability of breakage using only experimentally determinable quantities. An immediate observation of this equation is the lack of size dependence on the probability of breakage. Large particles are usually considered more

likely to break than smaller ones due to the presence of larger flaws. However, for this derivation the material does not break by crack propagation. Additionally, this derivation describes the probability of breakage given that an impact has occurred. The size dependence of breakage is contained in the impact efficiency η not the probability of breakage given an impact has occurred (see below).

Eqn. 3.14 predicts the critical value of the Stokes deformation number (St_{def}^*) to be 0.45. This is similar to the value estimated for granules under different impeller conditions by Smith et al.¹¹⁴ As there is no size dependence on the probability of breakage given an impact has occurred, particles of all sizes are expected to break if they experience an impact. Thus:

$$P_{break} = \begin{cases} 1 & St_{def} > St_{def}^* \\ 0 & St_{def} < St_{def}^* \end{cases} \quad (3.15)$$

Due to the high velocity of the pin, it is expected that $St_{def} \gg St_{def}^*$ except for extremely stiff pastes. That is to say $P_{break} = 1$. Therefore, over a wide range of paste rheology, the paste size distribution will not be a function of paste yield stress.

3.2.2 Impact Efficiency

The analysis of the P_{break} term has demonstrated that the critical parameter governing mechanical dispersion in the pin mixer is the impact efficiency between the impeller and nuclei. However, a given particle may not experience all 4 impacts during a single rotation. This phenomenon is accounted for in the impact efficiency η .

The impact efficiency describes the ability for nuclei to avoid pins by remaining in the bulk material. Large particles are more likely to impact the impeller for two reasons. First larger particles occupy more space and are therefore more likely to extend into the swept

volume of the impeller. Additionally, smaller particles with low inertia may be carried in the stream lines of the bulk material and be swept away from contact with the pin. The probability of impact should increase with increasing impeller speed as the inertia of the particle relative to the pin will increase. Combining eqn. 3.1, 3.2 and 3.15 yields:

$$K_{break} = 8\pi\omega * P_{break}(St_{def}) * \eta(x, \omega) \quad (3.16)$$

or

$$\left(\frac{K_{break}}{2\pi\omega}\right) = 4 * P_{break}(St_{def}) * \eta(x, \omega) \quad (3.17)$$

$\left(\frac{K_{break}}{2\pi\omega}\right)$ is the number of breakage events per revolution of the impeller. If $St_{def} \gg 1$, then from eqn. 3.15 $P_{break} = 1$. Thus eqn. 3.17 becomes:

$$\left(\frac{K_{break}}{2\pi\omega}\right) = 4\eta(x, \omega) \quad (3.18)$$

Early in the process when the paste particles are large, it is expected that $\eta(x, \omega) \approx$

1. Under these conditions, $\left(\frac{K_{break}}{\omega}\right)$ will be independent of both material properties and impeller speed. Thus, the paste nuclei size when plotted as a function of total number of impeller revolutions, should yield the same curve under all conditions. When paste nuclei size is small enough, $\eta(x, \omega)$ will reduce and the rate of breakage will also slow. Under these conditions, the nuclei size will be a function of impeller angular velocity ω due to its effect on η .

3.3 Methods and Materials

3.3.1 Materials:

Sodium aluminosilicate zeolite type A powder was used as the solid phase for the granulation. Figure 3.2 shows the particle size distribution of the zeolite measured using a Malvern Mastersizer 2000 using water as the dispersant with 50% maximum sonication.

Several measurements were taken to ensure that neither aggregation nor dissolution was occurring. Table 3.1 shows the material properties of the zeolite. The d_{50} of the zeolite is $3.8 \mu\text{m}$ and the bulk density is 390 kg/m^3 . Sodium aluminosilicate is a major constituent of the powder phase in many detergent granulations.

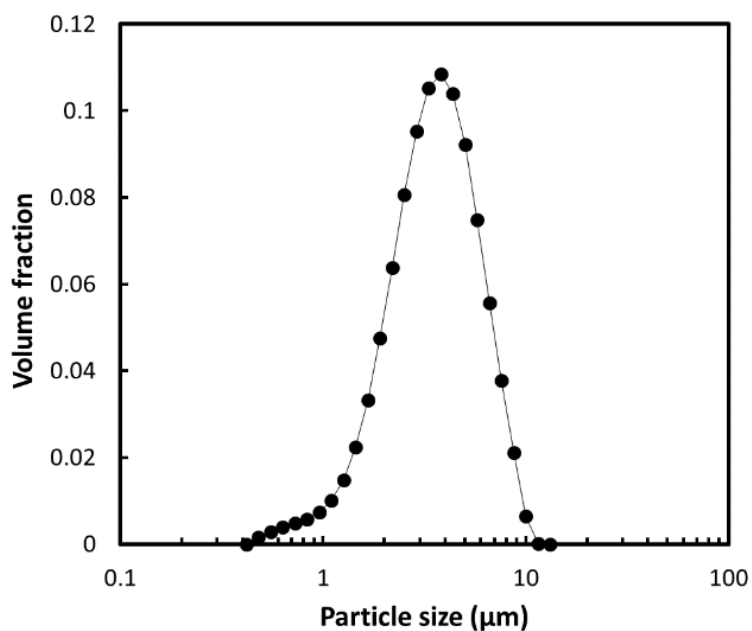


Figure 3.3.1 Particle Volume Distribution for sodium aluminosilicate powder.

Table 3.1 Properties of sodium aluminosilicate powder

NaA Powder Properties		
Size	d_{10}	$1.9 \mu\text{m}$
	d_{50}	$3.8 \mu\text{m}$
	d_{90}	$6.9 \mu\text{m}$
Density	Bulk	390 kg/m^3
	Tap	620 kg/m^3
Hausner Ratio		1.6

Two surfactant binders were used in separate granulation experiments surfactant A and surfactant B. Both pastes are a semisolid at room temperature and become more

fluid like at higher temperatures. Surfactant yield stress was characterized using two methods, a vane and cup rheometer for measurements at the higher injection temperatures and a squeeze test for room temperature measurements.

The high temperature yield stress was characterized using a TA instruments ARG2 rheometer with a vane and cup geometry. The surfactants and the jacketed rheometer cup were first preheated to the desired temperature. Next 25 g of surfactant was injected into the rheometer cup using a 60 ml syringe and pressed down into the cup to minimize air volume. Next the vane was lowered into the cup and immersed by the surfactant. The samples were sheared using a step transient stress growth setting at a constant shear rate for 300 seconds. The shear rate was varied between 0.01 s^{-1} and 100 s^{-1} with each experiment at a constant rotational speed. The yield stress, or characteristic stress, was defined as the maximum stress observed during the experiment¹¹⁵. For comparison, the shear rate in the pin mixer was calculated with eqn. 3.19:

$$\gamma = \frac{v_{tip}}{d_{gap}} \quad (3.19)$$

where γ is the shear rate and d_{gap} is gap distance between the pin tip and the wall of the pin mixer.

The room temperature yield stress was characterized by squeeze test using an Instron E1000. Sample pellets were produced at room temperature of $22 \text{ }^{\circ}\text{C}$ using a cylindrical mold with a diameter and height of 2.5 cm. The surfactant was scooped into the mold and then pressed to remove air pockets from the surfactant. Excess surfactant was trimmed from the top of the mold and the pellet was removed. Pellets were then placed on the load cell and compressed at a constant plate velocity in unconfined uniaxial compression. The velocity of the plate was varied between 0.05 mm/s and 10 mm/s. The

compaction ended when the distance between plates reached 1 cm. All surfactant material remained between the plates for the duration of the test. Results were analyzed similar to Tardos et. al.¹¹⁶ The yield stress was calculated by assuming a Brigham fluid rheological model for the surfactant using the analysis developed by Adams and Edmondson¹¹⁷ and implemented by Tardos et. al.:

$$\frac{p}{\tau_0} = \sqrt{3} + \frac{2R_0}{3h_0}(1-L)^{-1.5} + \frac{3\mu U_0}{8\tau_0 h_0} \left[\frac{2R_0}{h_0} \right]^2 (1-L)^{-4} \quad (3.20)$$

where p is the pressure on the plate, τ_0 is the yield stress, R_0 and h_0 is the initial pellet radius and height respectively, μ is the fluid viscosity constant, U_0 is the compaction velocity and L is the current height to initial height ratio defined as $L = d/h_0$.

The yield stress was determined by linearizing eqn. 3.21:

$$p(1-L)^4 = \left[\sqrt{3}(1-L)^4 + \frac{2R_0}{3h_0}(1-L)^{2.5} \right] \tau_0 + \frac{3\mu U_0}{8h_0} \left[\frac{2R_0}{h_0} \right]^2 \quad (3.21)$$

and calculating τ_0 by linear regression.

3.3.2 Mechanical Dispersion Experiments

Granulation experiments are conducted in a Processall Inc. Tilt-A-Pin granulator.

The granulator is a batch stainless steel 6L cylindrical pin mixer. The pin mixer is a horizontal high shear granulator 0.2m in diameter and 22 cm deep. The details of the pin mixer are proprietary. Annular flow of the powder is desired. Annular flow fully develops between 600 and 900 RPM corresponding to Froude numbers, Fr , between 18 and 40 calculated using eqn. 3.22 where R is the length from the axis of rotation to the pin tip, ω is the impeller angular velocity, and g is the gravitational constant.

$$Fr = \frac{R\omega^2}{2g} \quad (3.22)$$

The surfactant binder is injected through a 1 cm internal diameter pipe using a piston pump much like a large syringe. Surfactants were preheated in a convection oven until they reached the desired injection temperature. The experiment was conducted within one minute of removing the surfactant from the oven to minimize cooling. Surfactants were kept in sealed partially insulated containers to minimize moisture and heat loss.

Table 3.2 shows the granulation conditions used for the mechanical dispersion study. Experiments were designed to study mechanical dispersion alone by limiting the other rate processes. This was accomplished by using a low binder content granulation with a small amount of paste injected in a short period of time creating a pulse of binder into the granulator. The low binder content makes coalescences of granules negligible. The short granulation time and pin configuration minimize consolidation of granules by immersion nucleation. With these rate processes eliminated, the dominant rate processes are breakage and mechanical dispersion.

Table 3.2 Operating Conditions for Mechanical Dispersion Experiments

Parameter	Value Range
Paste Injection Temperature (T_i)	40 °C – 60 °C \pm 2 °C
Jacket Temperature (T_j)	22 °C \pm 1 °C
Impeller Speed	600 RPM – 1200 RPM \pm 10 RPM
Mixing Time	0 s – 10 s \pm 0.5 s
Powder Phase Mass	700 g \pm 2 g
Binder Mass	28 g \pm 1 g

Figure 3.3 depicts the experimental schedule for the mechanical dispersion pulse experiments. 50 g of binder was placed in the injection syringe and heated to the appropriate temperature. Next, the granulator was preloaded with 700 g of zeolite. The powder phase was then pre-mixed for 2 to 4 seconds. Next, 28g of the surfactant binder was injected over 1s. Finally, the granulator was allowed to run for a mixing time between 0 and 10 seconds and then shut off. The impeller speed ramped down to zero in less than one second. The total number of revolutions, N , was calculated using eqn. 3.23:

$$N = 2\pi\omega(t_{mix} + 1 \text{ sec}) \quad (3.23)$$

where t_{mix} is the mixing time of the experiment as defined in figure 3.3. The additional second accounts for the ramp down time and the end of the binder injection step.

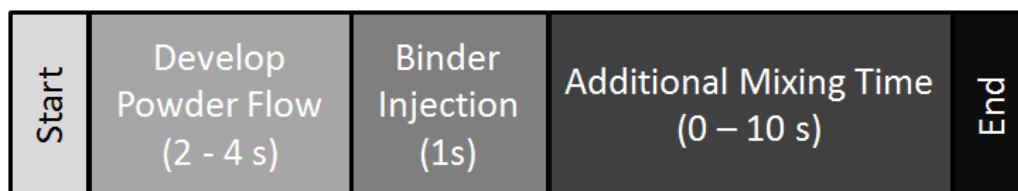


Figure 3.3.2 Experimental schedule for mechanical dispersion experiments.

3.3.3 Granule Characterization:

Granule size distribution was characterized using a W.S. Tyler Ro-Tap model E sieve shaker. The sieve stack is a $\sqrt{2}$ series sieve from 250 μm to 8.0 mm. The entire granulation batch for each experiment was used in the sieve analysis to eliminate sampling bias. Each batch was split into two sieve runs to prevent sieve blinding. The pan collects all of the zeolite which is smaller than the smallest sieve size. Because the primary particle size is less than about 10 microns, all particles that remain on the sieves

must contain surfactant. The size distributions were developed without the mass in the pan to examine the paste nuclei size distribution only.

The size distributions are shown as volume log frequency distributions $f_v(\ln(x))$ calculated using eqn. 3.24 where the index i indicates the distribution size bin, m_i is the mass in the bin, Δx_i is the width of the bin, and \bar{x}_i is the arithmetic mean size of the bin. Size distribution were further characterized by calculating the Sauter mean (d_{32}) and standard deviation (σ) from the moments of the distribution (μ_i) shown in eqn. 3.24 – 3.27.

$$f_v(\ln(\bar{x}_i)) = \frac{m_i}{\sum_{j=1}^N m_j} \frac{1}{\Delta x_i} \bar{x}_i \quad (3.24)$$

$$\mu_i = \sum_{j=1}^N \bar{x}_j^i f_j(\bar{x}_j) \Delta x_j \quad (3.25)$$

$$d_{32} = \frac{\mu_3}{\mu_2} \quad (3.26)$$

$$\sigma = \sqrt{\mu_2 - \mu_1^2} \quad (3.27)$$

3.4 Results

3.4.1 Surfactant Yield Stress:

Figure 3.4 shows typical results for the step transient stress growth of the surfactant. Over the course of the experiment the stress in the surfactant grows until reaching a peak value and then decays. The peak value of the experiments is used as an approximation for the yield stress of the surfactant.

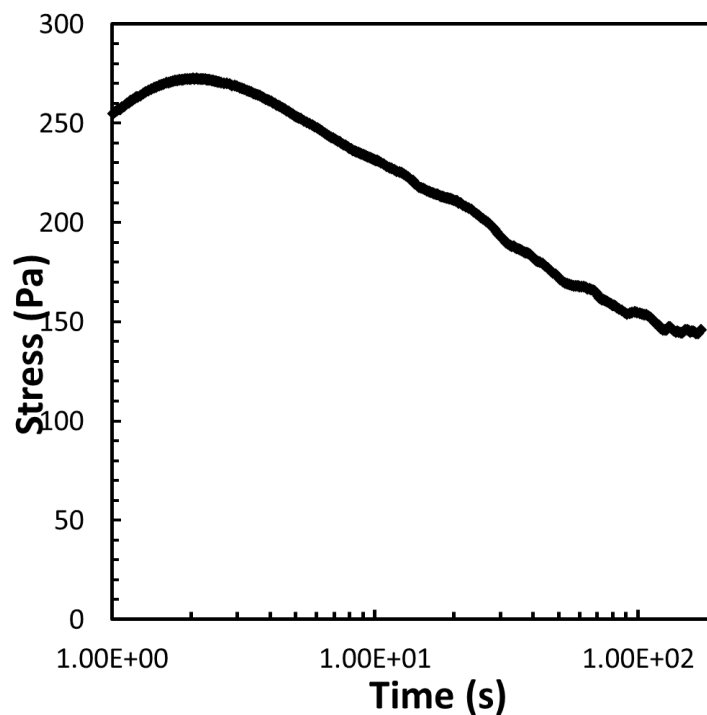


Figure 3.4.1 Typical results for step transient stress growth (surfactant A, 60 °C shear rate 1 s⁻¹).

Figure 3.5 shows the dependence of the measured maximum stress with shear rate. There is a modest increase in yield stress with shear rate with a dependence on shear rate of $\gamma^{0.14}$. For both surfactants, the effect of temperature on the yield stress was found to be negligible in the range of 50 °C to 60 °C. The yield stresses of surfactant A and B were compared at a shear rate of 0.01 s⁻¹. At these conditions, the yield stress of surfactant A was 160 Pa and the yield stress of surfactant B was 110 Pa indicating that surfactant B is “softer” than surfactant A at the injection temperatures.

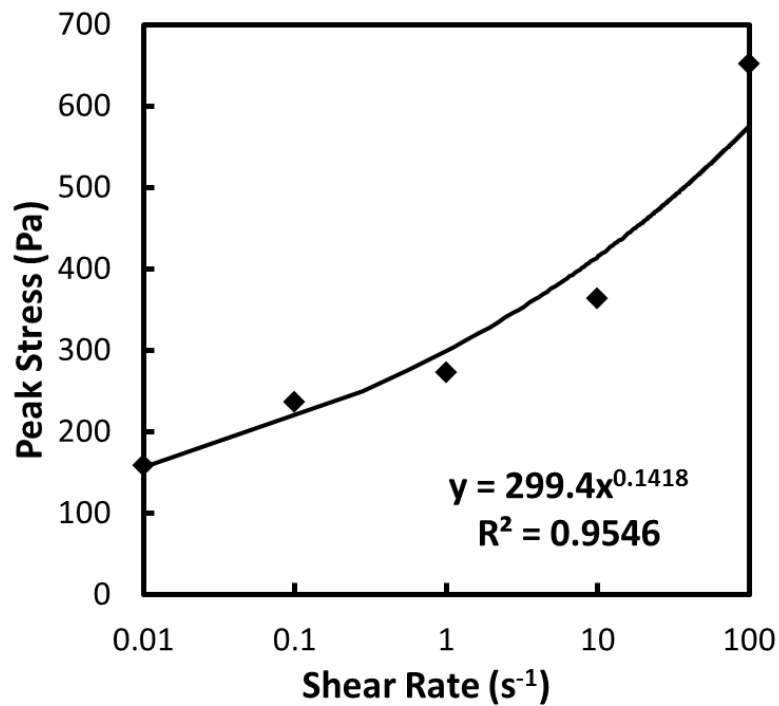


Figure 3.4.2 Dependence of measured peak stress on shear rate for Surfactant A at 60 °C.

Figure 3.6 shows typical regression results for the room temperature squeeze flow test. Fitting a linear regression to the plot in figure 3.6 provides the yield stress of the surfactant paste, in this case 420 Pa. The regression provides a good fit although from the residuals there is clearly variance in the data that is not explained by the linear model.

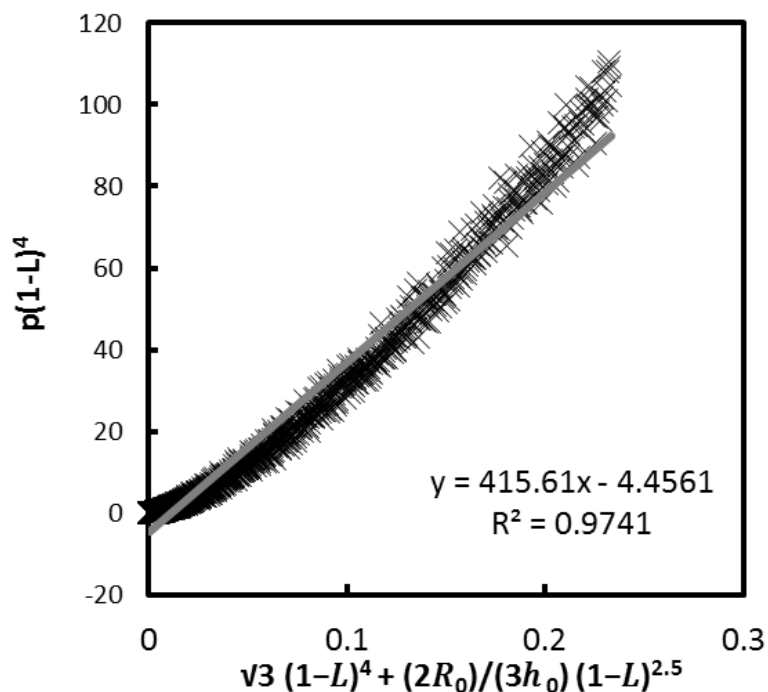
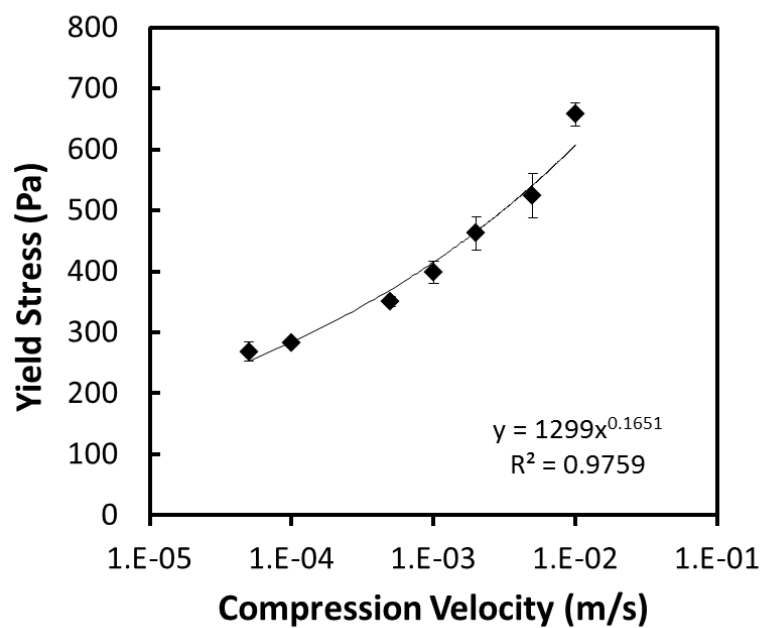


Figure 3.4.3 Regression of stress strain data the yield stress is the slope of the line (surfactant A), compression speed 10^{-3}ms^{-1} .

Figure 3.7 shows results for the squeeze test of both surfactants A and B. The results show that both materials exhibit a similar yield stress dependence on velocity of $v^{0.165}$, a similar dependence to that seen for the high temperature cup and vane shear tests. The yield stress for surfactant A is similar to that measured in the cup and vane test at high temperature. In contrast, surfactant B, which solidifies at approximately 40C, has a yield stress at room temperature that is 20 times higher than the value at 60C and 10 times higher than surfactant A. There is a transition in rheology as temperature decreases. surfactant B is softer than A at high temperatures. As the surfactants cool, the yield stress of surfactant B increases substantially above the yield stress of surfactant A.

a)



b)

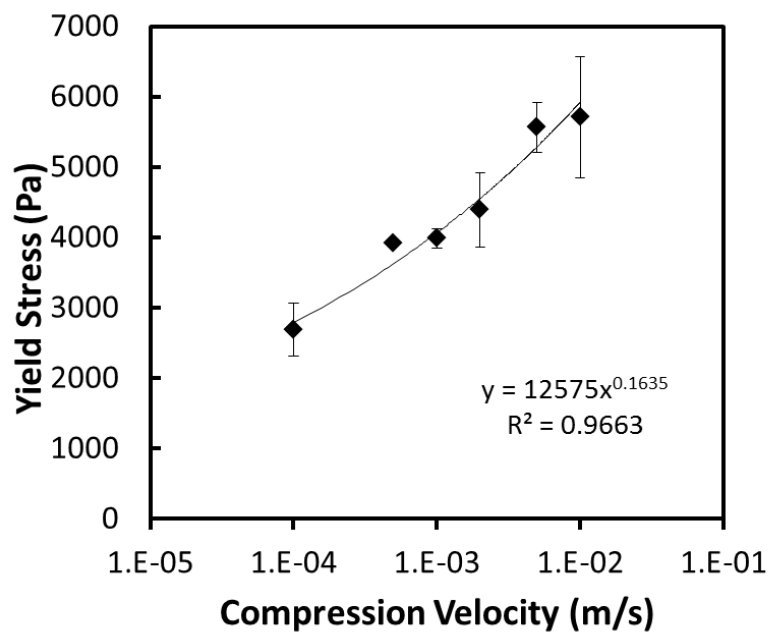


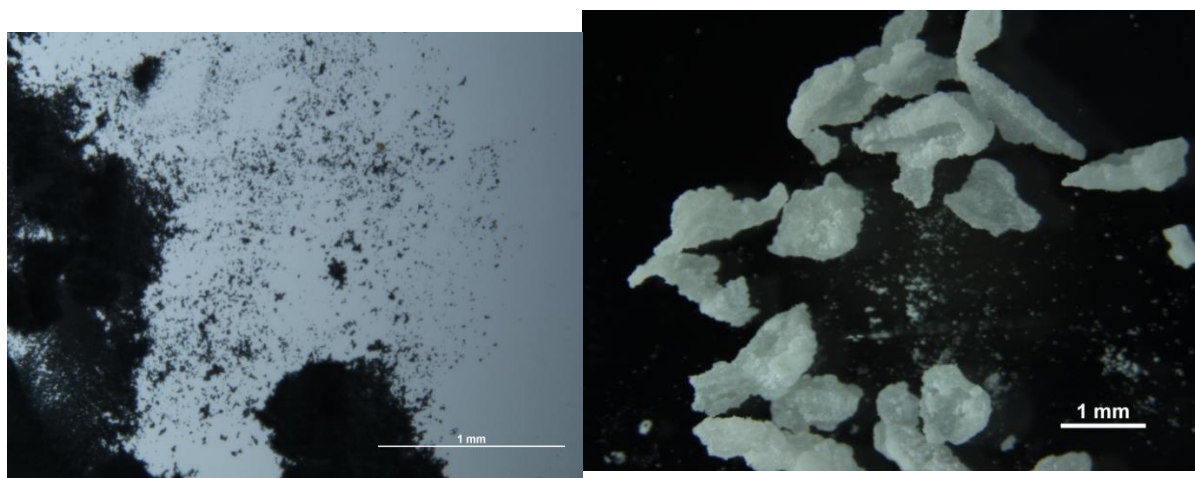
Figure 3.4.4 Yield stress for a) surfactant A and b) surfactant B for various compression velocities.

3.4.2 Mechanical Dispersion Kinetics:

A total of 160 mechanical dispersion experiments were conducted over a range of impeller speeds (600, 900, 1200 RPM), surfactant injection temperatures (40, 50, 60 °C), mixing times (0 – 10 secs), and type of surfactant (A, B). Replicate experiments were performed for a subset of the experiments to characterize the repeatability of the pulse experiments. The temperature range was chosen to be above the solidifying temperature of approximately 40 °C for surfactant B and below the decomposition temperature of approximately 70 °C.

For all experiments with impeller speeds of 900 and 1200 RPM ($Fr = 40, 71$), fully developed annular flow was achieved. At 600 RPM ($Fr = 18$), the flow was not truly annular as some material would fall away from the wall before completing a revolution.

The particle size distributions from sieve analysis do not include the material in the pan, only the material on the sieves. This is acceptable since the mechanical dispersion of the paste is occurring at the sieve sizes above the pan. Figure 3.8 shows a comparison of the material on the sieve and the material on the sieve. The paste fragments that are elongated and irregularly shaped. The surfactant fragments on the sieve consist almost entirely paste with a fine coating of powder that is mostly removed during sieve analysis. More than 90% of the total injected paste was recovered on the sieves.



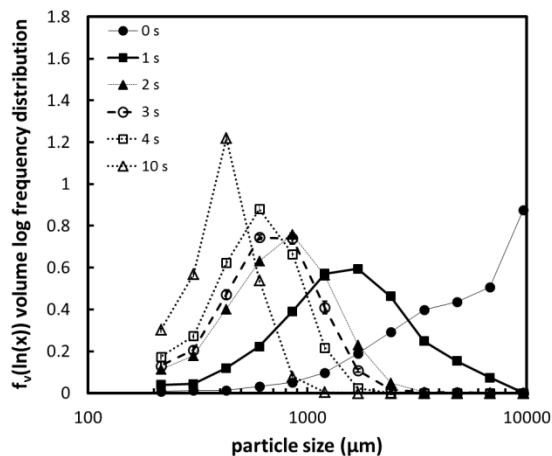
(a)

(b)

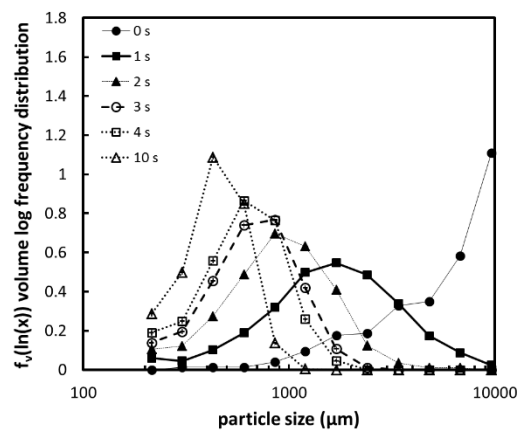
Figure 3.4.5 a) Material in Pan and b) material on sieve after sieve analysis for surfactant A

Figure 3.9 shows typical results of the breakage kinetics of the surfactant granulation for surfactant A at 60°C over the range of 0 to 10 seconds of mixing time. At 1200 RPM, the size distribution narrows and approaches a log normal distribution with a peak at approximately 500 μm after 10s. The granule size distribution continues to move to the left (finer sizes) throughout the dispersion experiment.

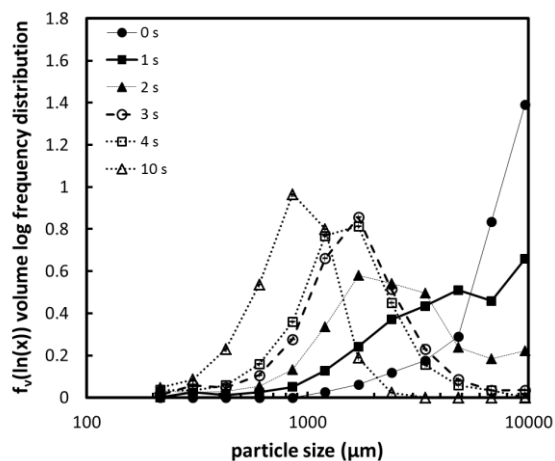
The same trend is observed in both the 900 and 600 RPM results. Both distributions narrow and approach log normal distributions. However, the mode size after 10s varies with impeller speed and is approximately 700 μm for the 900 RPM experiments and 900 μm for the 600 RPM experiments.



(a)



(b)

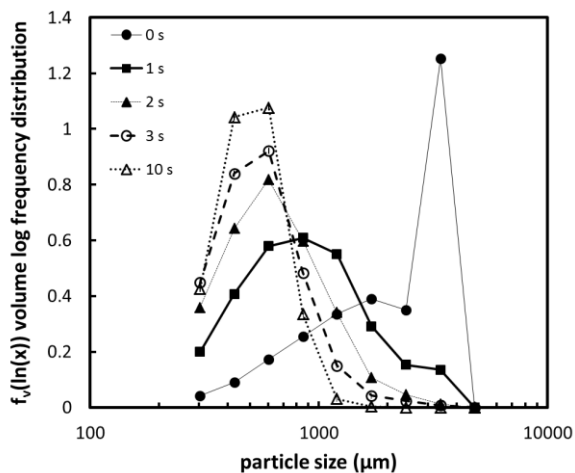


(c)

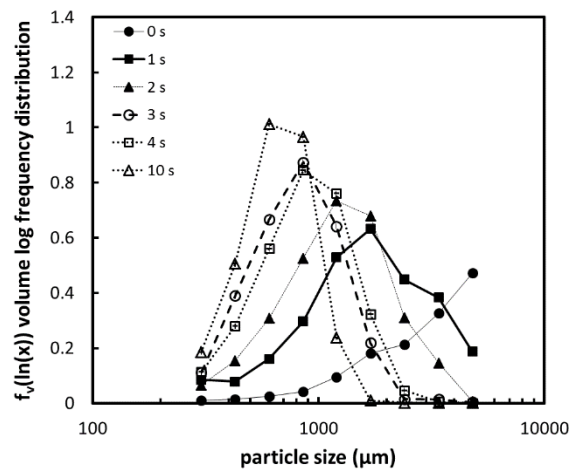
Figure 3.4.6 Volume log frequency distributions showing mechanical dispersion kinetics for surfactant A with an injection temperature of 60 °C at a) 1200 RPM, b) 900 RPM, c) 600 RPM.

Kinetic experiments for surfactant B are shown in Figure 3.10. As for surfactant A, the particle size distribution narrows over time approaching a log normal distribution. However, for surfactant B, the rate of change of the size distribution slows after the first

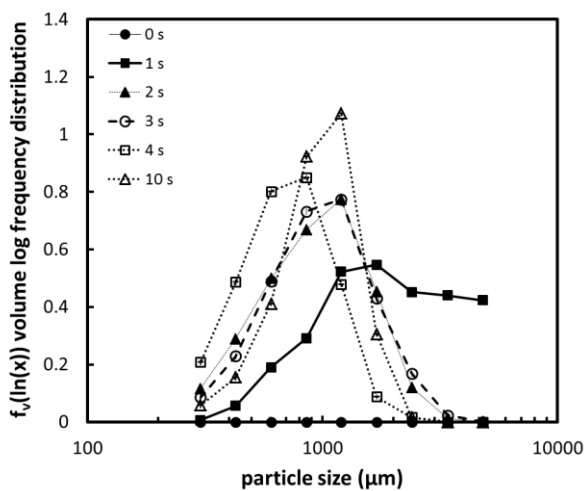
3-4s. The mode of the particle size distribution after 10s increases with decreasing impeller speed: 500 μm at 1200 RPM, 900 μm at 900 RPM and 1000 μm at 600 RPM.



(a)



(b)



(c)

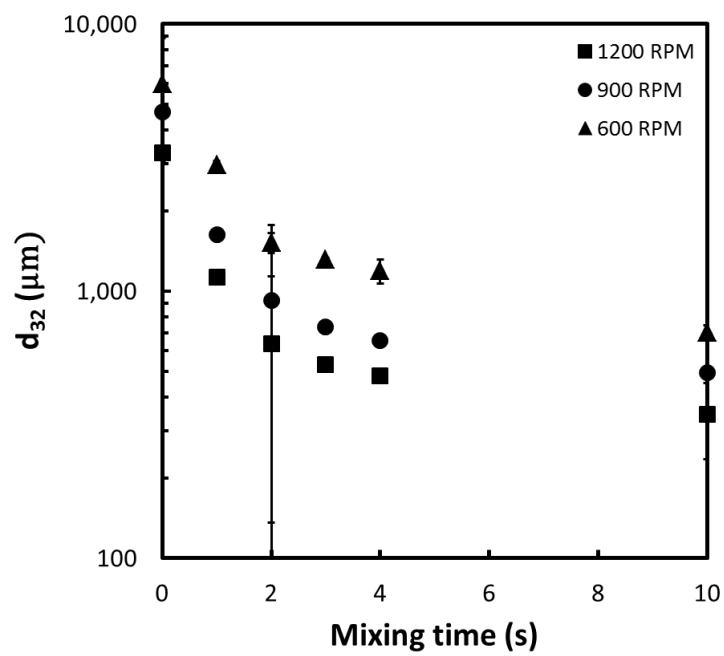
Figure 3.4.7 Volume log frequency distributions showing mechanical dispersion kinetics for surfactant B with an injection temperature of 60 °C at a) 1200 RPM, b) 900 RPM, c) 600 RPM.

Particle size distributions are characterized by the Sauter Mean (d_{32}) and normalized standard deviation (σ/d_{32}) of the distribution. Figure 3.11 shows the effect of

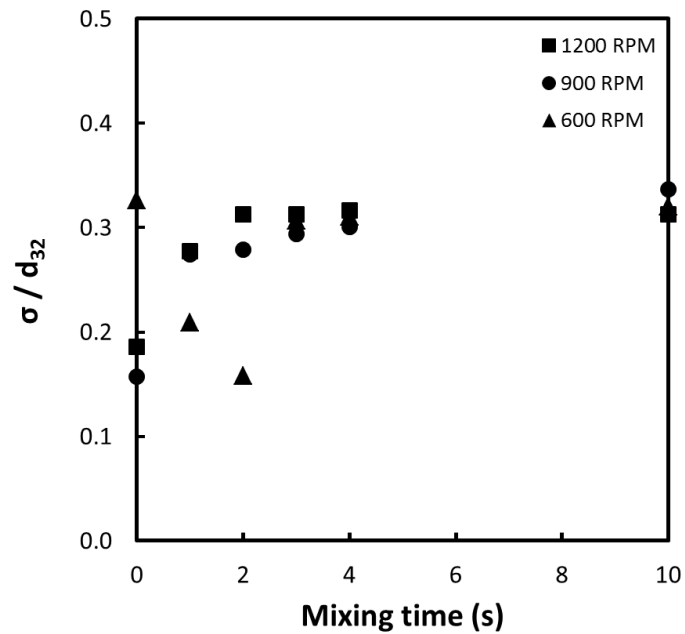
mixing time on the d_{32} and σ at 1200, 900, and 600 RPM. d_{32} decreases rapidly with time at the start of the experiment, with the rate of change decreasing as the experiment progresses. This indicates that the rate of breakage is a function of surfactant particle size with large particles breaking more quickly than smaller particles. The normalized standard deviation also reaches a steady value showing the distribution rapidly narrows and then maintains a consistent distribution shape.

Surfactant B also undergoes the same reduction in breakage rate with time (figure 3.12). However, unlike surfactant A, surfactant B reaches an asymptotic value for the final mean size that is reached after approximately three seconds. Note that the initial rate of change of d_{32} is actually higher for surfactant B than for surfactant A.

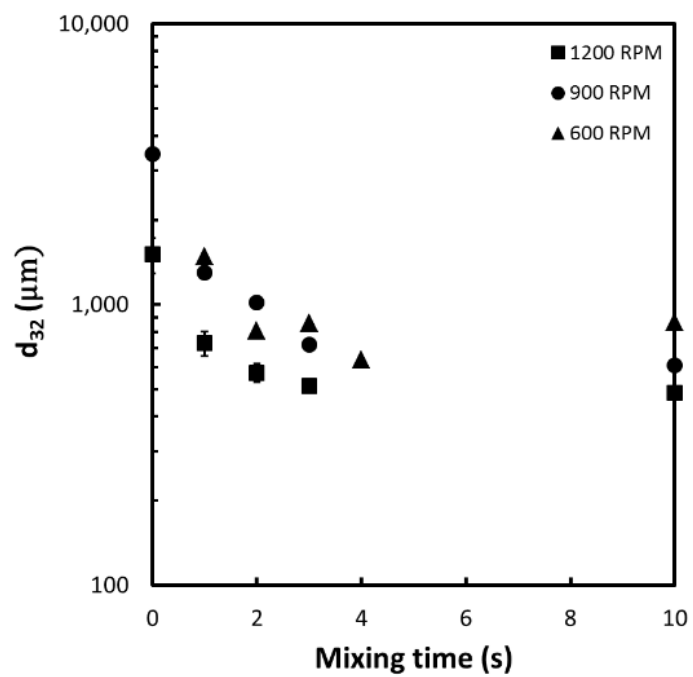
a)



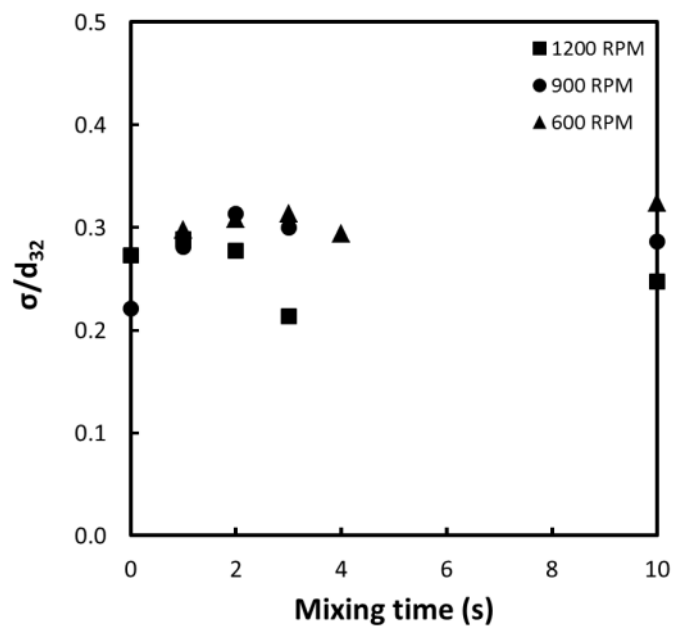
b)

Figure 3.4.8 a) d_{32} and b) σ / d_{32} for surfactant A kinetics at 60 °C

a)



b)

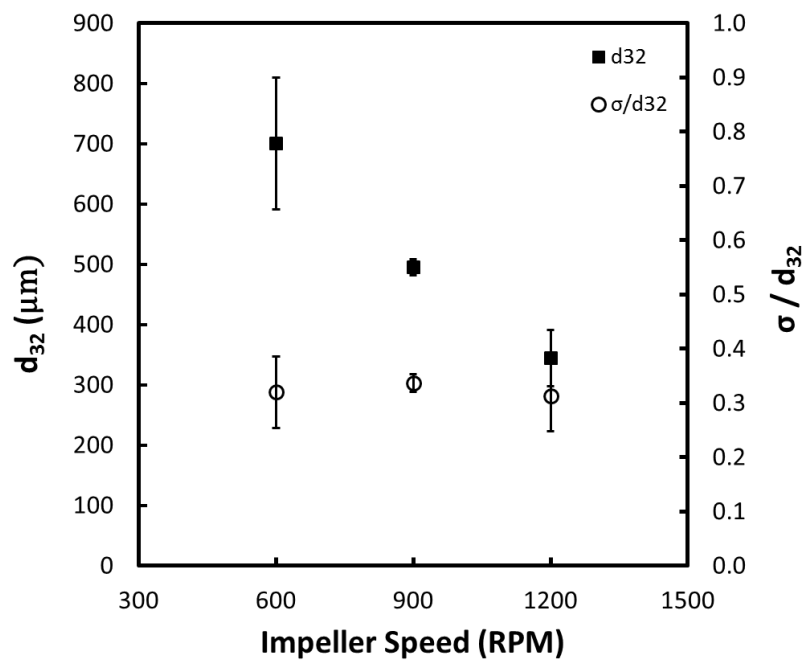
Figure 3.4.9 a) d_{32} and b) σ/d_{32} for surfactant B kinetics at $60\text{ }^\circ\text{C}$

3.4.3 System Parameter Effects on Mechanical Dispersion:

Figure 3.13 shows the effect of impeller speed on the Sauter mean size for an injection temperature of 60 °C and mixing time of 10s. Particle size decreases with increasing impeller speed for both surfactants.

Figure 3.14 shows the effect of surfactant injection temperature on the Sauter mean size for surfactant A and B. The particle mean size is independent of paste injection temperature at both short and long mixing times for surfactant A. However, the injection temperature does affect the Sauter mean size for surfactant B, especially at short mixing times. As the injection temperature increases, the Sauter mean size decreases.

a)



b)

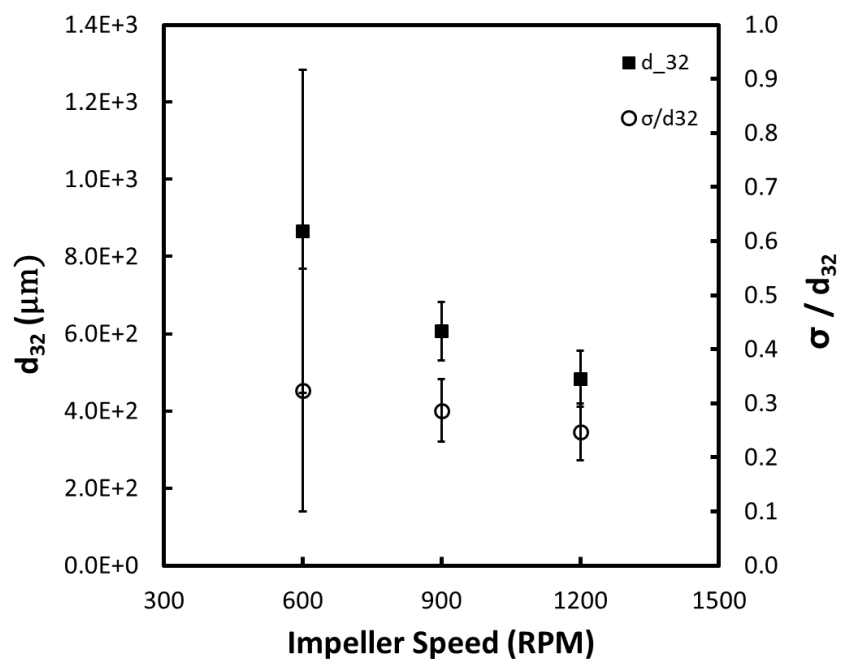


Figure 3.4.10 Impeller speed dependence of the d_{32} and σ / d_{32} at 60 °C injection temperature and 10 sec mixing time for (a) surfactant A and (b) surfactant B.

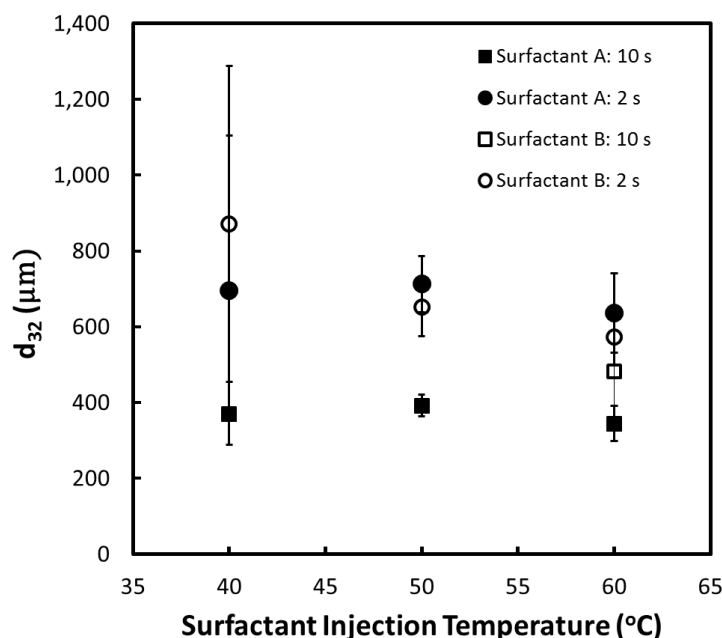


Figure 3.4.11 Temperature dependence of the d_{32} for surfactant A and B at 1200 RPM and 2 s and 10 s mixing time.

3.5 Discussion

The results of the mechanical dispersion pulse experiments show that the dispersion of the surfactant is similar to a breakage process. The dispersion is not instantaneous, but nuclei size distribution decreases with time. After 10 seconds of mixing time, the particle size distribution lies primarily below 1000 μm for high temperatures and impeller speeds. The desired particle size for product granules of the industrial process is typically between 300 μm and 1000 μm . After the mechanical dispersion of the surfactant into nuclei, no further agglomeration is necessary. All that is required is the incorporation of solids by immersion nucleation to achieve the desired granule assay. The detergent granulation process does not require agglomeration to achieve the desired particle size.

Agglomeration will produce a large amount of oversize granules that are unwanted and must be milled down to the appropriate size.

The results of the yield stress characterization produced an interesting result. Both the vane and cup rheometer and the squeeze test produced a power dependence on shear rate and velocity respectively. The dependence on shear rate in the vane and cup rheometer was found to be $\gamma^{0.14}$. The squeeze test used at room temperature showed a power dependence on velocity of $v^{0.16}$. These values of the powers are close indicating a consistent effect of velocity on yield stress. Although both characterization techniques were physically different, the consistency of the velocity dependence indicates the ability to compare the two techniques.

Additionally, the two methods showed a higher order effect of temperature between the two surfactants. In the range of the injection temperatures, both surfactants were of a similar order of magnitude with surfactant B being softer than surfactant A. However, at room temperature the squeeze test indicated that the yield stress of surfactant B is an order of magnitude higher than surfactant A. Surfactant A was found to have a yield stress at the injection temperature of about half an order of magnitude of the room temperature yield stress. This result indicates a temperature dependent transition for which past has the larger yield stress. Since the pin mixer was operated at room temperature it is expected that the surfactant would cool during the experiment thus changing their strength.

3.5.1 Stokes Deformation Number

Table 3.3 shows the calculated Stokes deformation number for the mechanical dispersion experiments. The Stokes deformation number is calculated using eqn. 3.14 for

both room temperature (22 °C) and the highest injection temperature (60 °C). The velocity is assumed to be the tip speed of the impeller. For the room temperature calculation, the yield strength is calculated using the regression from the squeeze test experiments. The room temperature yield stress represents the limiting case when the binder will begin to resist breakage. The yield strength for the 60 °C Stokes deformation number is determined using the regression of the vane and cup rheology experiments. The dependence on shear rate is determined for surfactant A and applied to surfactant B.

Table 3.3 Stokes deformation numbers using room temperature and injection temperature yield stress.

Surfactant	RPM	St_{def} (22°C)	St_{def} (60°C)
A	1200	31.6	83.2
A	900	18.7	48.6
A	600	8.87	22.8
B	1200	3.27	110
B	900	1.93	64.4
B	600	0.927	30.3

The Stokes deformation numbers for Surfactant A are several orders of magnitude above critical value of 0.45 determined by eqn. 3.14. The high values of the Stokes deformation number confirm that the probability of breakage given an impact has occurred is 1.

Surfactant B has similar values for the Stokes deformation numbers to surfactant A at 60C but much lower values at room temperature. This is a result of the order of magnitude difference in the yield stress between the two surfactants at room temperature. However, surfactant B is still larger than the literature value of the critical value. This indicates that the probability of breakage for surfactant B is also close to 1 for all experimental conditions.

The Stokes deformation numbers in table 3.3 were calculated using the tip speed of the impeller. However, not all impacts or shear events may occur at this velocity due to the motion of the powder bed. The probability of breakage for surfactant B could be less than one if the characteristic velocity is less than the tip speed.

The results of the Stokes deformation number predict that breakage of surfactant A will occur for all impeller speeds and injection temperatures. In this case, the breakage of the surfactant will only be a function of the number of revolutions of the impeller. Surfactant B is more complex. The Stokes deformation number for Surfactant B predicts that initially breakage will occur for all impeller speeds and will likely occur more rapidly than surfactant A. However, after cooling in the granulator, surfactant B may resist breakage for a significant the fraction of impact conditions below the tip speed. This behavior is clearly seen in particle size distributions and Sauter mean size which show that surfactant B initially breaks more rapidly than surfactant A, but does not continue to break after the first few seconds of mixing time.

3.5.2 Number of Impacts

The breakage of surfactant into granule nuclei occurs in the granulator by two proposed mechanisms. The first mechanism is by impeller impact. In the impact mechanism, surfactant particles are hit by the high velocity pin and broken into smaller fragments. The second mechanism is breakage by shear. In the shear mechanism, the high shear rate developed in the bulk powder, especially between the pin tip and granulator wall, put high strain on the surfactant. Under sufficiently high strain the particles to elongate and finally break. Impact and shear mechanisms are likely to both be important in the granulation. It is possible that one of the mechanisms is primarily responsible for

the mechanical dispersion of the surfactant, but the experimental setup did not allow for the each mechanism to be tested separately.

Figure 3.15 shows the Sauter mean size as a function of number of revolutions rather than time, so that comparisons are made at the same possible number of impacts N for all impeller speeds. The number of impacts is calculated using the RPM and the time plus one additional second to account for the injection time and ramp down time. Both surfactant A and surfactant B demonstrate a smaller particle size as the number of revolutions increase.

The results in figure 3.15 demonstrate that most of the difference in particle size can be accounted for by the difference in the number of revolutions. The effect of temperature and RPM are second order to the number of impact effect. The results can be broadly broken into two regions. The first region is at low impeller revolutions and large particle size, and the second region is at high impeller revolutions and small particle size. The dividing line between the two regions falls around 50 revolutions.

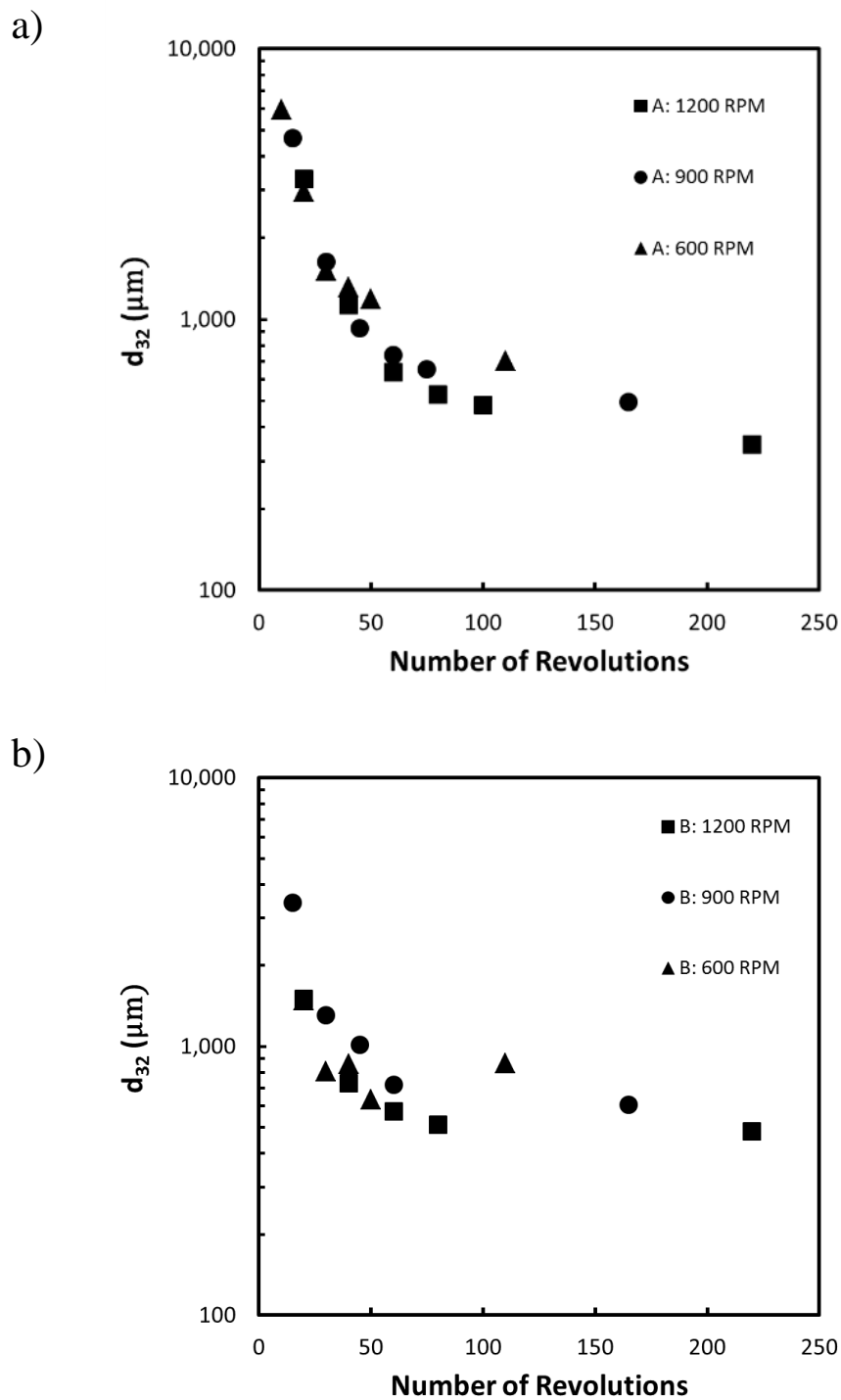


Figure 3.5.1 Sauter mean size at 60 °C versus number of impeller revolutions at 60 °C for (a) surfactant A and (b) surfactant B.

In the low impeller revolution region, the results show no dependence on particle size or impeller speed for surfactant A and a minimal dependence on impeller speed for surfactant B. In this region, the Sauter mean size is large and both P_{break} and η are nearly 1 for all conditions. Figure 3.16 shows the first 50 revolutions for all impeller speeds at 60 °C. In this region first order breakage is observed of the form:

$$d_{32} = Ae^{-kN} \quad (3.28)$$

where A and k are both constants. The breakage rate constants, k , are 0.046 rev^{-1} for surfactant A and 0.035 rev^{-1} for surfactant B.

Larger numbers of revolutions (seen in figure 3.15) and smaller particle sizes do exhibit an effect of the operation parameters for both surfactants. The mean particle size for more than 50 revolutions shows that higher impeller speeds produce a slightly smaller mean size. This is consistent with the impact efficiency model that predicts smaller particles size will produce fewer breakage events per revolution. In this region the breakage rate constant decreases with decreasing particle size. Additionally, the impact efficiency shows a dependence on velocity with higher impeller speeds producing a smaller mean size. The final three points corresponding to the 10 second mixing time experiments exhibit the greatest difference from the uniform size curve in the low revolution numbers region.

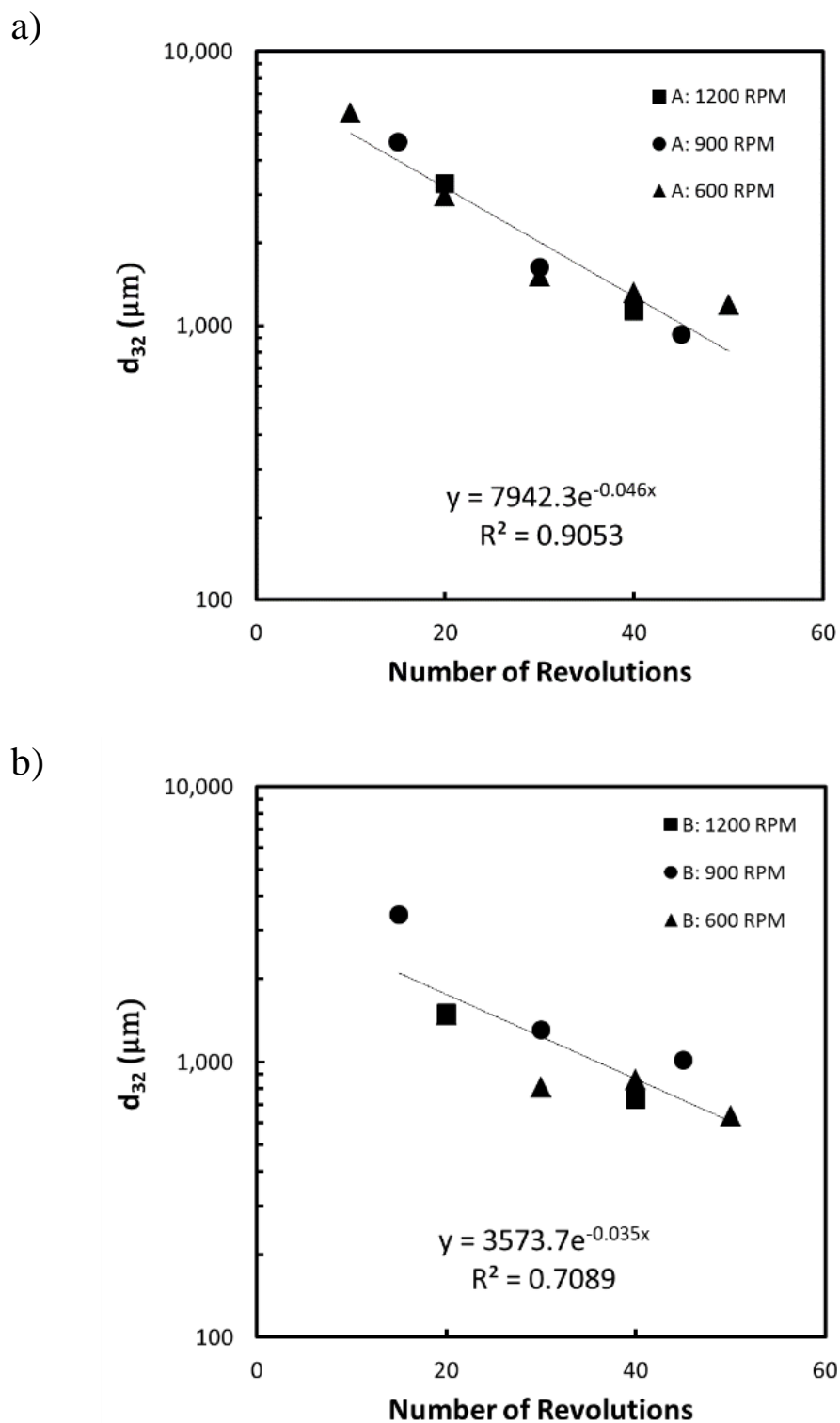


Figure 3.5.2 first 50 revolutions at all impeller speeds and 60 °C injection temperature for (a) surfactant A and (b) surfactant B.

Surfactant B exhibits a greater reduction in breakage than surfactant A due to changing yield stress. The changing yield stress is not accounted for in the number of revolutions model, but has a clear effect on the breakage kinetics. As seen in figure 3.16, the initial breakage rate constant is lower for surfactant B than for surfactant A. However, the actual particles sizes are smaller than those observed for surfactant B. This indicates that breakage occurs very rapidly for surfactant B during the first second of mechanical dispersion. Additionally, the high revolution number region shows nearly no additional breakage producing a breakage rate constant of approximately $k = 0$.

3.6 Conclusions

The results show that the mechanical dispersion of semi-solid binders can be treated as a breakage process. The breakage rate and resulting particle size of mechanical dispersion are dependent primarily on operating conditions and partially on the surfactant properties. The Stokes deformation number for this system is much greater than the critical value to prevent breakage. For this reason, it is expected that all impacts in the pin mixer will be successful making the impact efficiency the dominant mechanism. However, breakage by shear rather than direct impact with pins could contribute the size reduction of the surfactant. This is supported by the result that surfactant B does not experience the same amount of breakage as surfactant A after long mixing times due to surfactant B's higher yield stress.

The results demonstrate that the breakage of semi-solid surfactant pastes is dependent on the number of revolutions. The number of revolutions is proportional to the number of impacts that or breakage events that can occur. Effects such as material strength and impeller speed are second order to the number of revolutions. In this case,

modeling of the granulator requires the derivation of an efficiency equation that describes the likelihood of a particle being impacted by an impeller.

The results also show that detergent granulation is a breakage limited process. After the surfactant is broken into nuclei, the size distribution is similar to the desired product range. Further granulation only requires the immersion granulation mechanism to incorporate the bulk powder into the granule. Additional agglomeration is unnecessary and should be avoided if possible.

CHAPTER 4. POPULATION BALANCE MODELING OF SEMI-SOLID BINDER MECHANICAL DISPERSION AS A MILLING PROCESS

4.1 Introduction

In this chapter, the experimental results described in Chapter 3 are modeled using a 1D population balance model. The description of the experimental methods is not reiterated in this chapter. The objective of this chapter is to develop a semi-empirical mechanistic model for the mechanical dispersion of the semi-solid binder. The objective is achieved by:

1. Determine mechanistic basis to model the impact efficiency of the binder in the pin mixer. The incorporates the operating conditions of the pin mixer.
2. Use experimental data to determine fitting parameters in the model.
3. Compare the experimental particle size distributions with the distributions predicted by the model.

The results of chapter 3 demonstrated that the mechanical dispersion of surfactant is a breakage only process. As discussed in chapter 2, breakage only processes can be sufficiently described by a 1D population balance model. The 1D breakage only population balance model takes the form:

$$\frac{dy_i(t)}{dt} = -K_{break,i}y_i(t) + \sum_{j=i}^N K_{break,j}b_{i,j}y_j(t) \quad (4.1)$$

where i is the index variable indicating the current particle size bin, y_i is the mass fraction of particles of size i , $K_{break,i}$ is the selection function, and $b_{i,j}$ is the product distribution function. The choice of selection function and product distribution together is referred to as the breakage kernel.

4.2 Theory

The nucleation of the semi-solid binder by mechanical dispersion is modeled as a breakage process. The breakage selection function describes the mass fraction of particles that a particle undergoing a breakage event breaks into. In the pin mixer system, the breakage selection function was previously described as:

$$K_{break} = N * \eta(x, \omega) * P_{Break}(St_{def}) \quad (4.2)$$

where N is the maximum number of impacts per time, η is the impact efficiency which is a function of particle size x and impeller angular velocity ω , and P_{Break} is the probability of material breakage given an impact has occurred which is a function of the Stokes deformation number St_{def} .

The derivation found in chapter 3 reduced eqn. 4.2 to:

$$K_{Break} = 8\pi\omega * \eta(x, \omega) \quad (4.3)$$

Therefore, the breakage selection function is primarily dependent on the impeller speed and the impact efficiency.

Binder particles in the real pin mixer may not undergo 4 impacts in one rotation. Particles may be in a position where they are not in the pin path. Alternatively, binder particles may be able to bypass the pin by remaining in a streamline of the bulk material as it “bends” around the pin. The ability for particles to avoid pin impacts is described by the impact efficiency term.

It is hypothesized that the pin mixer can be analyzed in a similar way to predicting the capture efficiency of a gas-solid filter. In a gas-solid filter, particles suspended in a fluid impact with a cylindrical fiber if the particle streamline takes it on a collision path. It is assumed that the binder material is similar to the solid particles in the gas stream. The binder nuclei flow in the streamlines of the continuous zeolite bed phase and gets impacted by the pins, analogous to the inertial interception of the solid particles in a gas phase on the bag filter fibers.

The aerated powder bed is not a simple Newtonian fluid. Nevertheless, continuum models which treat moving powder beds as a fluid phase or multi-phase have been used with some success to model granular flow. The Eulerian-Eulerian two fluid method in CFD has shown success in capturing the primary attributes of dense granular flow¹¹⁸⁻¹²⁰. However, characterizing granular flow viscosity remains very difficult. Darelus et. al.¹²⁰ found that a bulk viscosity on the order of 0.1 Pa*s provided good agreement between high shear granulation velocity data and the CFD model. In contrast, Zhang et. al.¹²¹ experimentally characterized the apparent viscosity of fine metal powders. The authors found that powders with a size of less than 10 μm had an apparent viscosity of order 10 Pa*s. The two cases vary by orders of magnitude and do not provide certainty about the true viscosity of the powder flow. For this reason, viscosity will be incorporated as part of a fitting parameter.

Davies and Peetz¹²² determined numerical solutions of the continuum equations for the collision efficiency between particles and the filter fiber as a function of particle size to fiber ratio and the Stokes number Stk (not to be confused with St_{def}) and defined as:

$$Stk = \frac{\rho x^2 v}{18\mu d} \quad (4.4)$$

where ρ is the density of the particle, x is the size of the particle, v is the velocity of the particle in the fluid, μ is viscosity of the fluid, and d is the diameter of the filter fiber cylinder. The Stokes number is the ratio of particle inertia to the viscous drag force from the fluid on the particle. In this case study, v is the tip speed of the pin, d is the diameter of the pin, ρ is the density of the surfactant, and μ is the viscosity of the bulk powder flow. The authors demonstrated that as the Stokes number increased, the impact efficiency also increased since fewer particle streamlines avoided the fibers. The numerical results were shown graphically for several Reynolds numbers.

Based on the graphical results of Davies and Peetz, it is assumed that for high Reynolds numbers, as is the case of the high speed pin mixer, the collision efficiency of particles can be approximated using an exponential distribution function dependent on the Stokes number of the form:

$$\eta = 1 - \exp(-\lambda_1(Stk - Stk^*)) \quad (4.5)$$

where λ_1 and Stk^* are parameters of the distribution. The fitting parameter λ_1 also accounts for the viscosity of the bulk material since the value is difficult to measure and can vary by orders of magnitude depending on the system. The critical Stokes Number, Stk^* , represents the minimum particle size that undergoes an inertial impact with the pins of the mill. Mathematically this value also accounts for nuclei that travel in a stream line far from the pin and are not impacted regardless of particle size. Stk^* , is a material constant, but is expected to vary with geometry. For example, an impeller with closely packed pins will have fewer no impact streamlines than an impeller with pin spaced far apart.

Substituting η from eqn. 4.5 into eqn. 4.3 produces the final form of the breakage selection function.

$$S = 8\pi\omega[1 - \exp(-\lambda_1(Stk - Stk^*))] \quad (4.6)$$

or in expanded form:

$$S = 8\pi\omega \left[1 - \exp \left(-\lambda_1 \left(\frac{\rho x_i^2 v}{18\mu d} - Stk^* \right) \right) \right] \quad (4.7)$$

Eqn. 4.6 predicts that the selection function and therefore the breakage and particle size distribution are dependent on the impeller speed and the Stokes number. Eqn. 4.6 is also a 1D equation in terms of particle size. The remaining parameters are either experimentally measurable or fit to the particle size distributions. Eqn. 4.7 can be converted into the discretized form of the selection function S_i :

$$S_i = 8\pi\omega \left[1 - \exp \left(-\lambda_1 \left(\frac{\rho x_i^2 v}{18\mu d} - Stk^* \right) \right) \right] \quad (4.8)$$

The mathematical form of eqn. 4.8 is similar to that of the Vogel and Peukert model for particle breakage. Both are exponential and functions of particle size and impact velocity. However, the two models describe different breakage mechanisms. The Vogel and Peukert model describes breakage by crack propagation as the dominate mechanism and is a function of x^l and v^2 . Eqn. 4.8 describes breakage by efficiency of impact between the impeller and the nuclei. Eqn. 4.8 is a function of the Stokes number and thus x^2 and v^l . As a result, eqn. 4.8 predicts a stronger dependence on particle size and a weaker dependence on velocity than the Vogel and Peuket model.

The breakage distribution function represents the size distribution of the daughter particles once the mother particle undergoes a breakage event. For simplicity, it is

assumed that the volume based cumulative breakage distribution, B , is a power law equation and is represented by:

$$B_{i,j} = \left(\frac{x_i}{x_j}\right)^q \quad (4.9)$$

where x_i is the size of the initial particle, x_j is the size of the daughter particles, and q is a fitting parameter. The convention used is that $i = 1$ represents the largest size fraction in the distribution. Eqn. 4.9 is then used to calculate the breakage distribution function which in discretized form is:

$$b_{i,j} = B_{i,j} - B_{i,j+1} \quad (4.10)$$

Eqn. 4.8 and 4.10 combine to form the breakage kernel. This kernel is semi-empirical and combines physical understanding with three fitting parameters that are determined from experimental data. Table 4.1 summarizes the parameters that must be experimentally measured or estimated to fully describe the model.

Table 4.1 Description of breakage model parameters.

Parameter	Description	Determined by:
λ_l ,	Efficiency fitting parameter Estimates viscosity in Stokes number Expected function of: <ul style="list-style-type: none"> Material Properties 	Estimated
Stk^*	Critical Stokes Number Accounts for nuclei not on impact streamline Expected function of: <ul style="list-style-type: none"> operating conditions equipment geometry 	Estimated
q	Breakage distribution parameter Expected function of: <ul style="list-style-type: none"> material Properties 	Estimated
ρ	Surfactant nuclei density (kg/m^3)	Measured
v	Pin tip speed (m/s)	Measured
d	Pin diameter (m)	Measured
ω	Impeller angular velocity (1/s)	Measured

4.3 Model Solution

The dynamic model for the breakage only process is analyzed as a population balance model using commercially available gSOLIDS 4.0.0 (Process Systems Enterprise Ltd, UK), by implementing the breakage kernel, as described in eqns. 4.8 and 4.10. Being an equation oriented software, it provides for a seamless integration of experimental data for building, validating, and executing first principal models in a flow sheet framework¹²³ thereby being inherently dynamic and suitable for simulation of a solids operation batch process¹²⁴.

The process flowsheet is developed as a custom 1D population balance model size in gSOLIDS, as shown in Figure 1. The dimension used in the model is nuclei particle size. The system is defined by specifying the material properties of the semi-solid binder, as it is the material phase of interest. The model is setup to mimic the experimental procedure (figure 3.3) and determine the mechanical dispersion kinetics of the semi-solid binder.

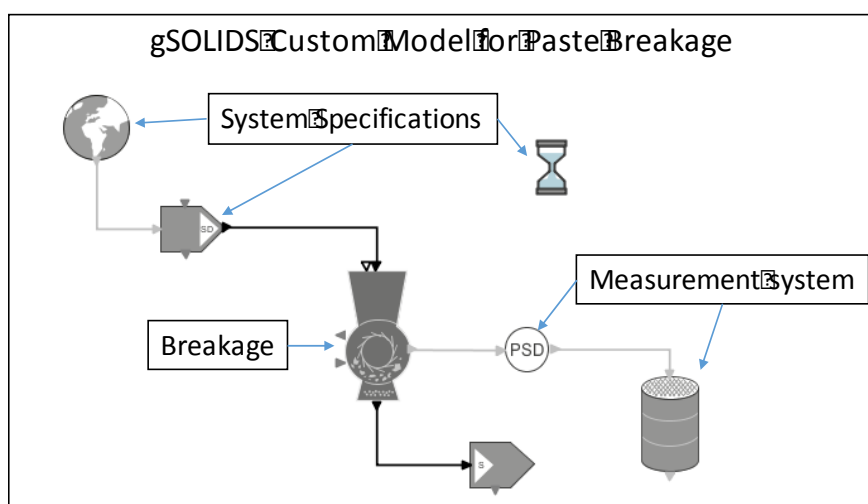


Figure 4.3.1 gSOLIDS process flow sheet for the breakage process.

Pulse experiments (described in Chapter 3) are used to estimate the parameters that characterize the dynamics of the breakage process. The duration of the dynamic simulation of the process is kept at 12 seconds in accordance to the experimental conditions. The dynamic simulation duration is 2 seconds greater than the actual experimental duration to observe the behavior of the system after 10 seconds.

The nuclei size dimension of the population balance equation is discretized to match the sieve analysis from the experimental results. The sieve analysis data at 0 seconds is used as the initial conditions for the simulation. Parameter estimation is conducted by comparing the experimental sieve mass fractions with those predicted by the model. The variation in the sieve analysis measurement is considered to have a constant variance. The frequency based calculations for the Sauter Mean Diameter (d_{32}) is recorded using a holdup sensor model.

4.3.1 Parameter Estimation

Parameter estimation in gSOLIDS is based on the maximum likelihood formulation, which provides simultaneous estimation of parameters in both the physical model of the process as well as the variance model of the measuring instruments, given by:

$$\Phi(\theta) = \frac{N}{2} \ln(2\pi) + \frac{1}{2} \min_{\theta} \sum_{i=1}^{NE} \sum_{j=1}^{NV_i} \sum_{k=1}^{NM_{ij}} \left[\ln(\sigma_{ihk}^2) + \frac{(\bar{z}_{ijk} - z_{ijk})^2}{\sigma_{ihk}^2} \right] \quad (4.11)$$

where N stands for the total number of measurements taken during all the experiments, θ is the set of model parameters to be estimated over the specified bounds, NE is the number of experiments performed, NV_i is the number of variables measured in the i^{th} experiment, and NM_{ij} is the number of measurements of the j^{th} variable in the i^{th} experiment. σ_{ijk}^2 is the variance of k^{th} measurement of variable j in experiment i . \bar{z}_{ijk} is

the k^{th} measured value of variable j in experiment i and z_{ijk} is the k^{th} model predicted value of the variable j in experiment i . For this case study, the values of z are particle size mass fraction and are compared for each experimental.

4.3.2 Parameter Estimation Strategy

The process model used in this work is a semi-empirical population balance equation with efficiency parameters λ_l , Stk^* , and distribution parameter q . These parameters are fit to a subset of the pulse experiments. The parameter estimation strategy is summarized in Figure 3. Three sets of parameter estimations are completed, two for surfactant A and one for surfactant B.

The results of the pulse experiments demonstrated that surfactant A, was temperature independent. For this reason, surfactant A is selected as the base case for the parameter estimation. The aim is to perform the minimum number of experimental runs in order to characterize the system. The Paste A 1200 RPM subset of experiments are used for the first parameter estimation. The three fitting parameters λ_l , Stk^* , and q are estimated along with the measurement variance σ_{ijk}^2 . Using these estimated values, the process variables ν and ω are changed to the corresponding operating conditions at 900 and 600 RPM. The model is run at the new conditions and the resulting predicted size distributions are compared to the respective experimental size distributions.

The fitted parameters are assumed to be dependent on material properties or equipment geometry, but not on impeller speed. The dependence on impeller speed is incorporated in the Stokes number. The second parameter estimation tests this by estimating the three fitting parameters using data for surfactant A at all three impeller speeds. The fitted model size distributions are then compared with the experimental data.

Additionally, the results of the first and second parameter estimation are compared to determine the models ability to capture the effect of velocity.

Parameter q is hypothesized to be material parameter. A change in the semi-solid binder material should result in a change in q , but not in λ_l or Stk^* . The third parameter estimation tests this by using the first parameter estimation values for λ_l and Stk^* , and refitting q to surfactant B data at 1200 RPM. Just as with the first parameter estimation, the size distributions at 900 and 600 RPM are predicted. The size distributions between the model and experiment are then compared. Additionally, the results of the first and third parameter estimation are compared to determine if the q parameter accurately captures the effect of material properties.

The sieve analysis for surfactant B did not have the same number of sieves as surfactant A. For this reason, the model data would appear to over predict breakage by assigning mass to unmeasured sieves. To compare equal masses, it was assumed that the sum of model mass fractions in the experimentally measured sieve trays would equal 1. This was accomplished by increasing the mass fraction of all model sieves trays by the same proportion until the experimental sieve stack summed to 1. This technique allowed for a closer comparison of the experimental and model results.

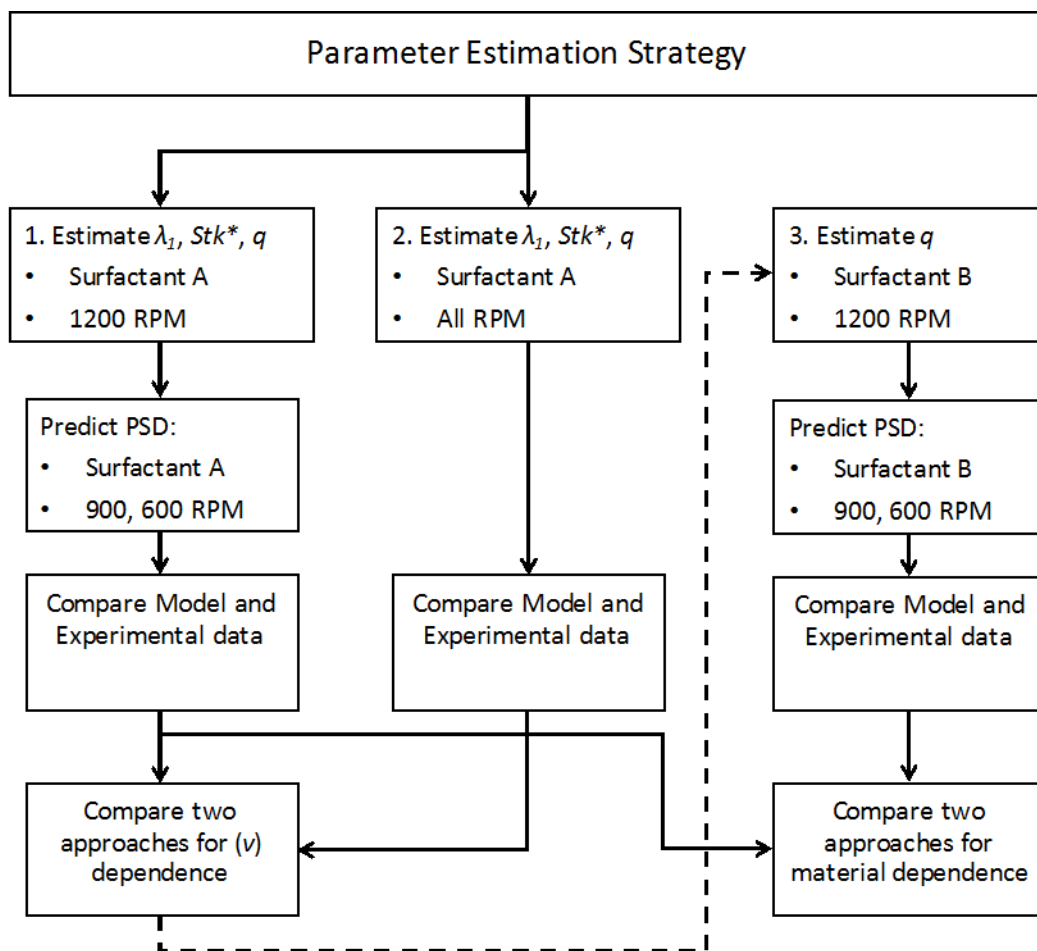


Figure 4.3.2 Flow sheet for parameter estimation of surfactant A and B.

4.3.3 Measure of Success

95% confidence intervals and the standard deviations for the estimated parameters is reported from the parameter estimation entity results of gSOLIDS. The particle size distributions are represented as Sauter Mean diameter d_{32} and normalized coefficient of variation σ/d_{32} . These are calculated for both experimental and model sieve analyses

A two sample paired t-test is performed for the Sauter mean diameter, d_{32} , by comparing the set of the d_{32} values of the model with the calculated d_{32} for the

experimental observations. The distributions are accepted at 95% confidence for Paste A and 90% confidence for Paste B.

4.4 Results and Discussion

The three sets of parameter estimations are presented in the same order and number as figure 4.2. Each parameter estimation is compared to the full size distributions.

However, for simplicity, the Sauter mean size d_{32} and normalized variance σ/d_{32} are compared for impeller speeds other than 1200 RPM. Full size distributions not shown here can be found in Appendix B.

4.4.1 Parameter Estimation 1

The first model parameter estimation was completed using experimental data for surfactant A from only the highest impeller speed (1200 RPM). Results for 900 and 600 RPM were obtained by changing the velocity in the breakage kernel and executing the simulation with the new values. Table 4.2 shows the value of the three estimated parameters along with the 95% confidence interval. The parameter values all pass the 95% t test indicating a good fit of the model and the model parameters..

Table 4.2 Estimated parameters using only 1200 RPM experiments for surfactant A.

Parameter	Estimated value \pm 95% CI	95% T (ref T: 1.654)
λ_1	0.00330 ± 0.00054	6.152
Stk^*	0.603 ± 0.173	3.484
q	-2.452 ± 0.299	8.21

Figure 4.3 shows the model and experimental results for the first parameter estimation at 1200 RPM. Overall, the model provides a very good fit of the experimental data. The main discrepancy between the model and experiment is at 1 second of mixing time where the model slightly over predicts the amount of breakage. Additionally, at 10

seconds of mixing time the model slightly under predicts the amount of breakage.

However, at intermediate mixing times, the model does an almost perfect job of matching the full size distribution. Figure 4.4 shows the d_{32} and σ/d_{32} parameters of the distributions in figure 4.3. As is seen in figure 4.3, the model is able to match the average particle size for all times after 1 second of mixing time.

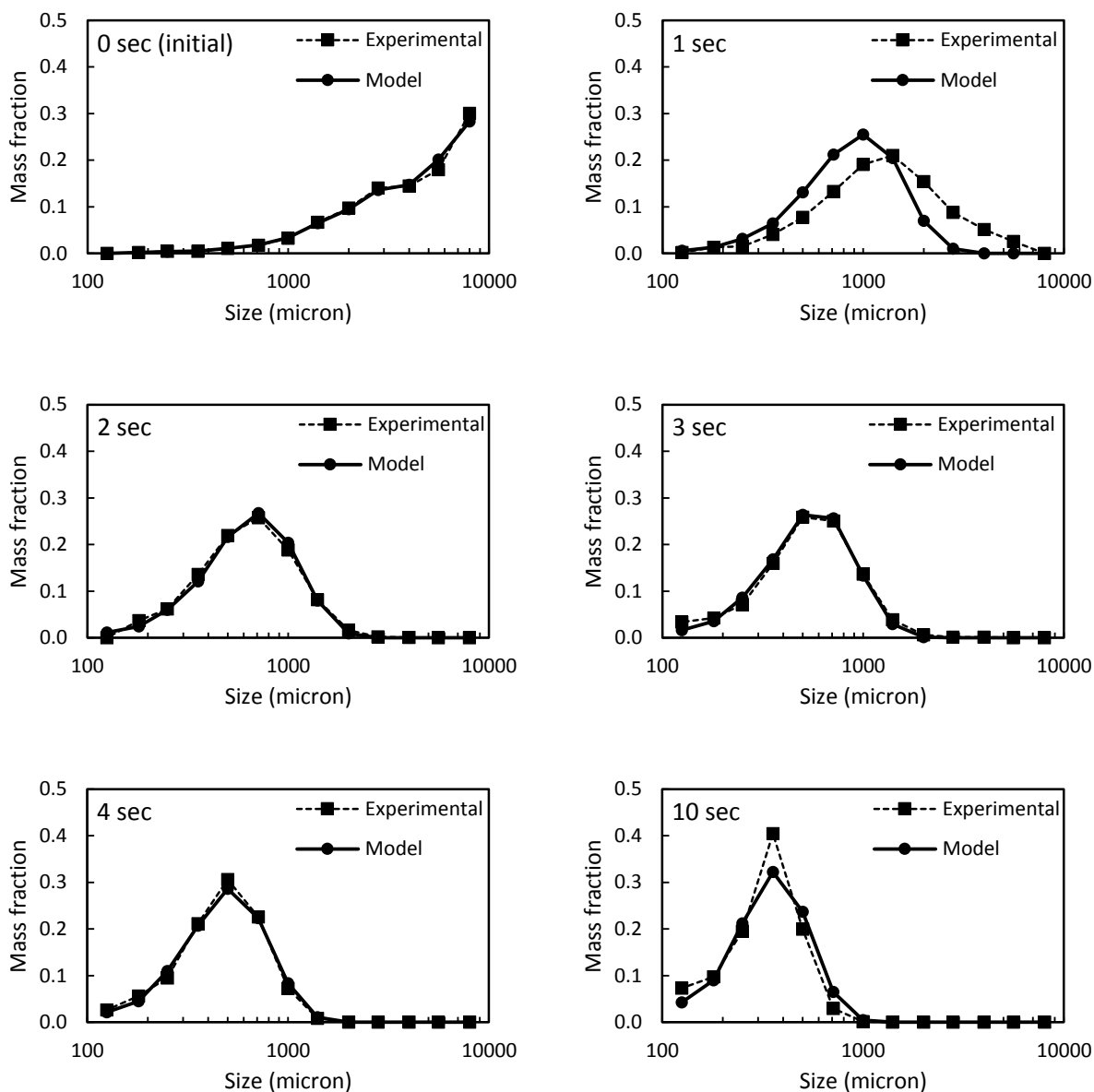


Figure 4.4.1 Particle size distributions of model and experiments for Surfactant A at 1200 RPM fit to 1200 RPM experiment data.

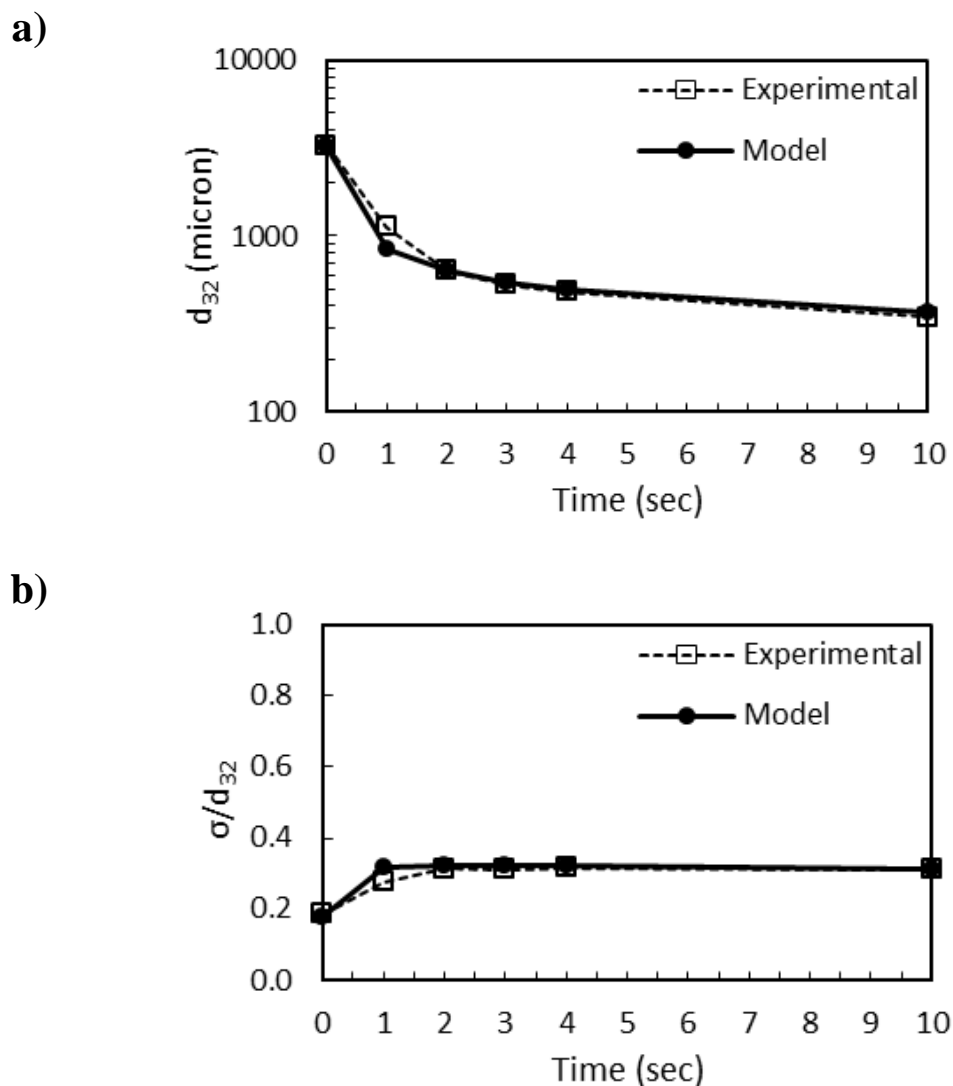
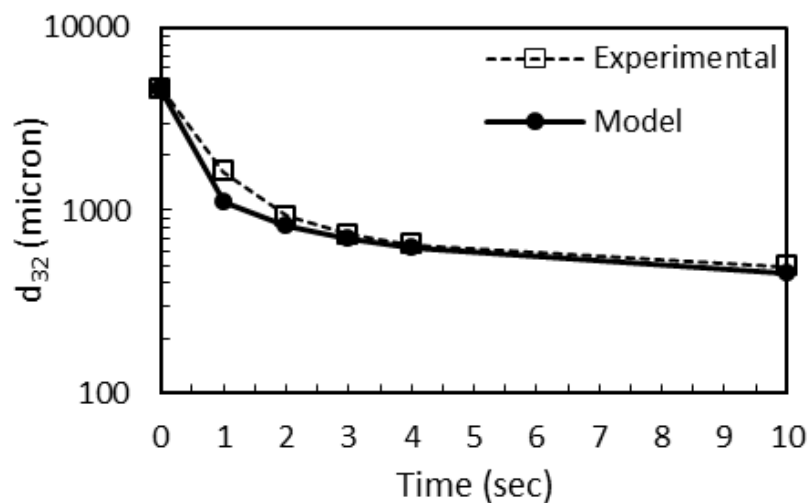


Figure 4.4.2 a) d_{32} and b) σ/d_{32} for surfactant A at 1200 RPM fit to 1200 RPM experimental data.

Figure 4.5 shows the d_{32} and σ/d_{32} parameters of the distribution for both the model prediction and experiments for surfactant A at 900 RPM. The results are similar to those at 1200 RPM showing a good fit at all mixing times other than 1 second. The model also slightly over predicts the normalized variance. The results demonstrate that the

model is able to accurately describe the effect of pin tip speed on the particle size distribution.

a)



b)

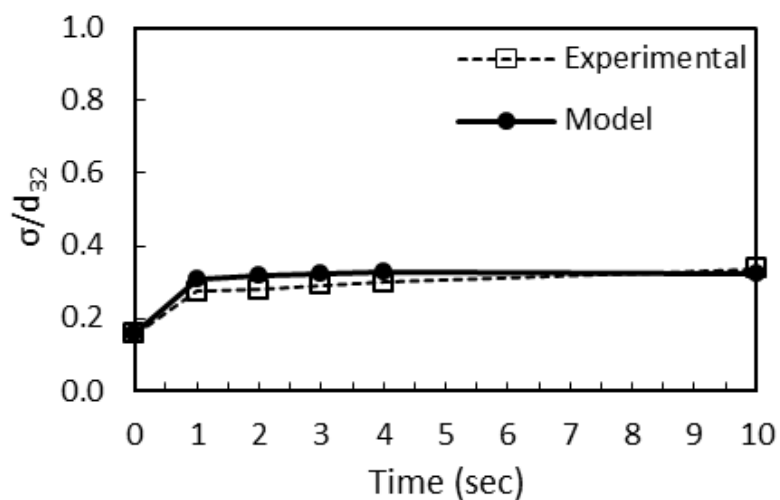
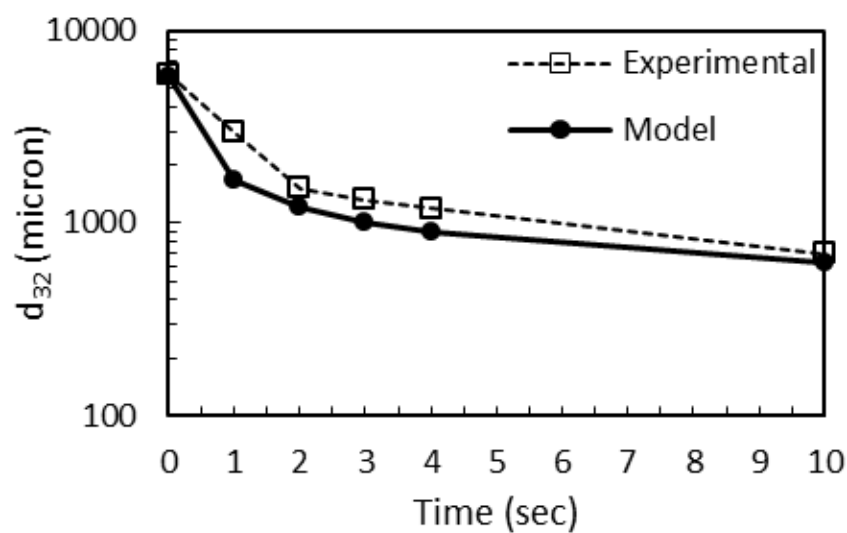


Figure 4.4.3 a) d_{32} and b) σ/d_{32} for surfactant A at 900 RPM fit to 1200 RPM experimental data.

Figure 4.6 shows the d_{32} and σ/d_{32} parameters of the distribution for both the model and experiments for surfactant A at 600 RPM. The model prediction is not as good as the 900 RPM case. The model consistently over predicts the amount of breakage for all

mixing times at the low RPM. The model is unable to capture the normalized variance at low mixing times. This is because the 600 RPM impeller speed has a greater experimental variation than the higher impeller speeds. In the 600 RPM case, the desired annular flow may not be fully developed increasing the inconsistency of the experimental results.

a)



b)

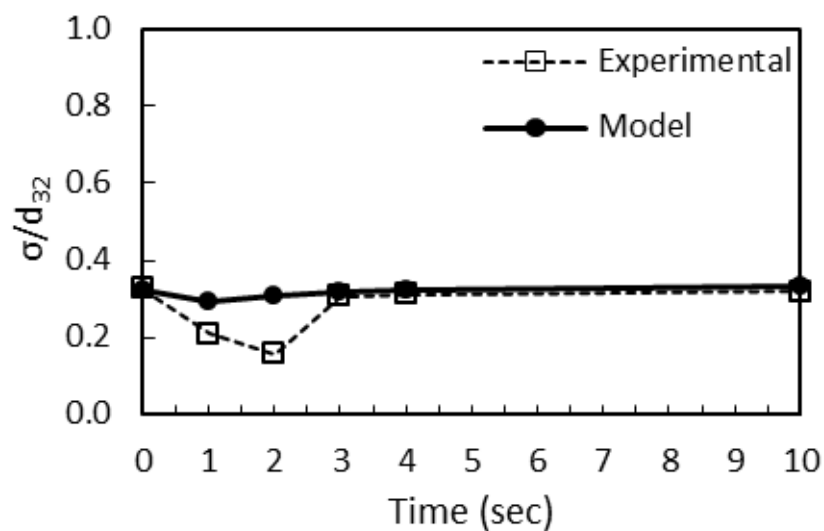


Figure 4.4.4 a) d_{32} and b) σ/d_{32} for surfactant A at 600 RPM fit to 1200 RPM experimental data.

The model results of the parameter estimation using only 1200 RPM data for surfactant A show strong agreement with the experimental results. Changing the impeller speed in the breakage kernel is all that is necessary to accurately predict the size distributions at an impeller speeds of 900 RPM and to a lesser degree, 600 RPM. The accurate prediction and low confidence intervals on the fitted parameters indicates that the breakage kernel accurately describes the mechanical dispersion of surfactant A.

4.4.2 Parameter Estimation 2

The second parameter estimation case used surfactant A experiments at all impeller speeds. Table 4.3 shows the values of the three estimated parameters. The results show no appreciable difference in the value of λ_1 for both estimation cases. However, the value of the critical stokes number, Stk^* , has decreased, and the magnitude of q has increased. The confidence interval is again small and all parameters pass the T test.

Table 4.3 Estimated parameters using all surfactant A experiments.

Parameter	Estimated value \pm 95% CI	95% T (ref T: 1.649)
λ_1	0.00298 ± 0.00036	8.325
Stk^*	0.481 ± 0.176	2.734
q	-2.734 ± 0.244	11.23

Figure 4.7 shows the model and experimental results for surfactant A at 1200 RPM. Just as with the previous parameter estimation, the model produces a good fit of the experimental data. The fit of the 1200 RPM data is not as good as the first estimation. This is because the model performed the parameter estimation with the experimental results for surfactant A at all impeller speeds. Just as with the previous parameter estimation, the model slightly over breaks the nuclei at short mixing times and slightly under breaks nuclei at long mixing times. Figure 4.8 shows the d_{32} and σ/d_{32} parameters

of the distributions in figure 4.7. The 1 second mixing time is shows the most deviation between the model and experiment.

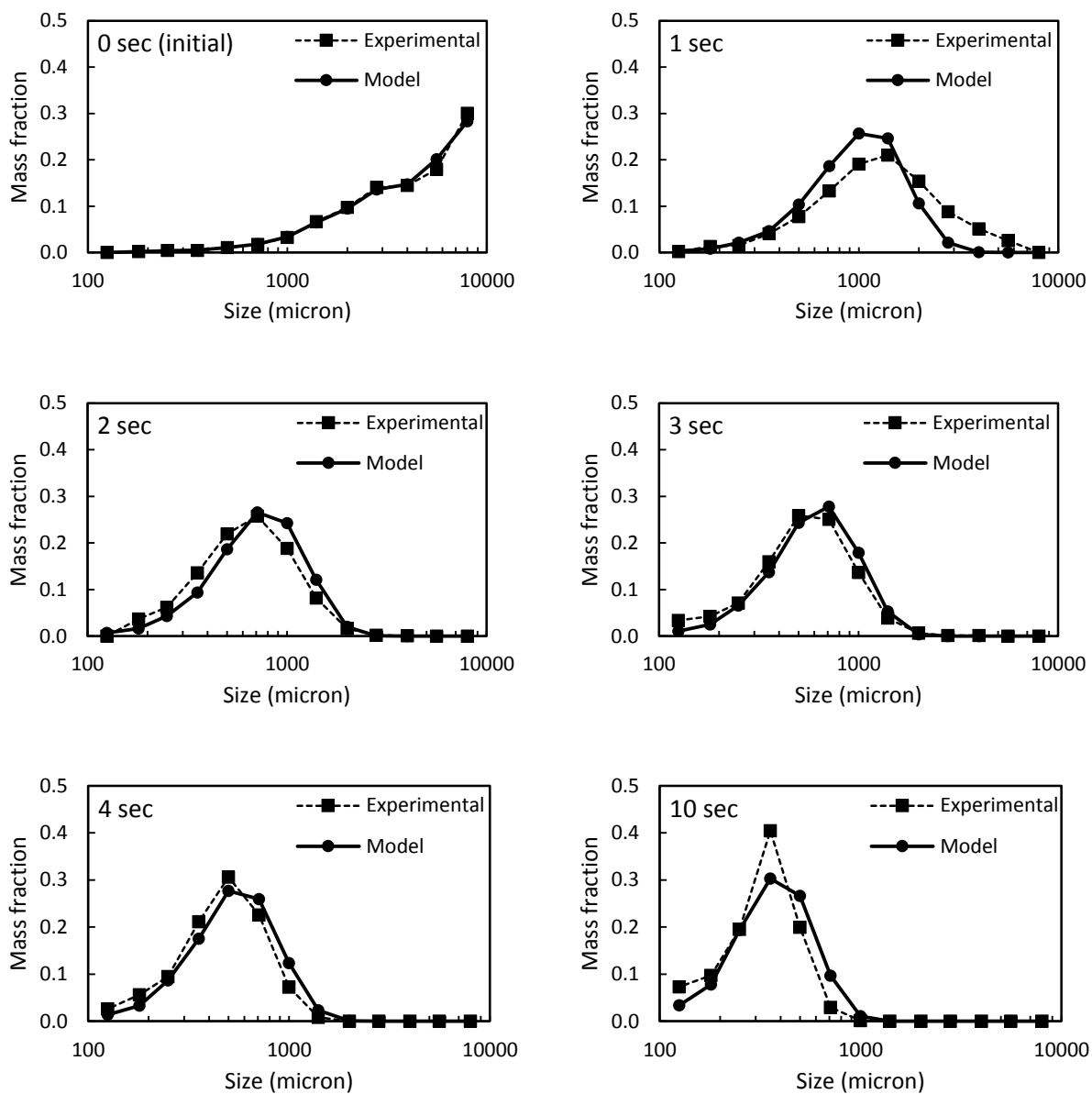


Figure 4.4.5 Particle size distributions for model and experiments for Surfactant A at 1200 RPM fit using all experiments.

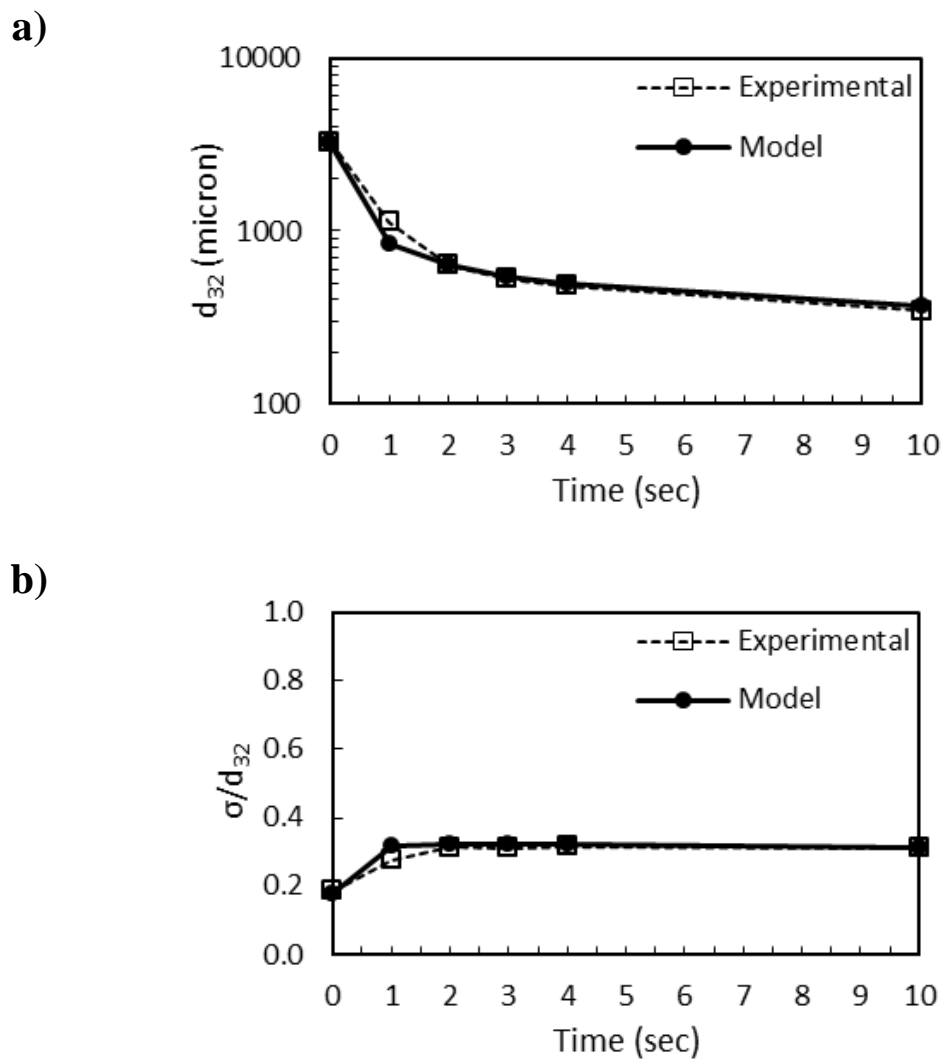


Figure 4.4.6 a) d_{32} and b) σ/d_{32} for surfactant A at 1200 RPM fit using all surfactant A experiments.

Figure 4.9 shows the d_{32} and σ/d_{32} parameters of the distribution for both the model and experiments for surfactant A at 900 RPM. The model produces a good fit for all mixing times. However, the fitted model shows only a slight improvement over the predicted values from parameter estimation 1. The fitted data slightly over predicts the normalized variance parameter indicating the model expects a slightly wider distribution than is actually observed.

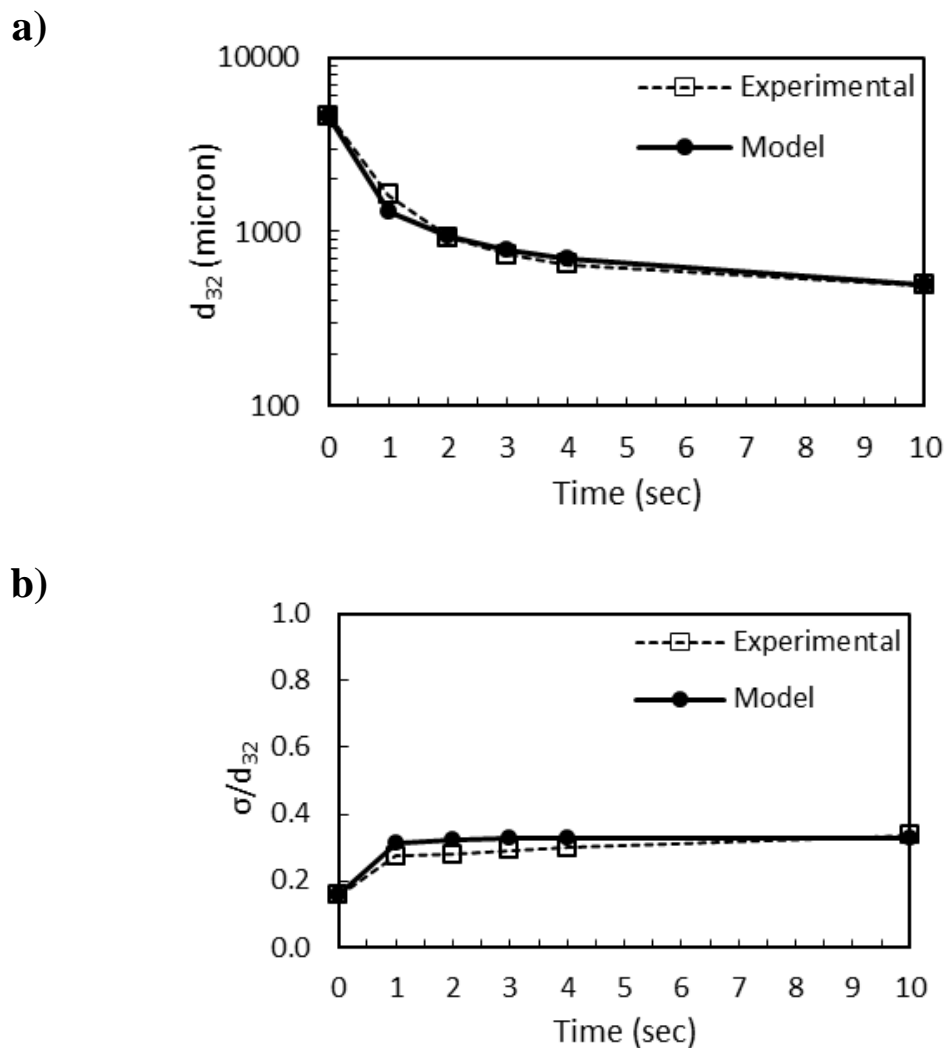
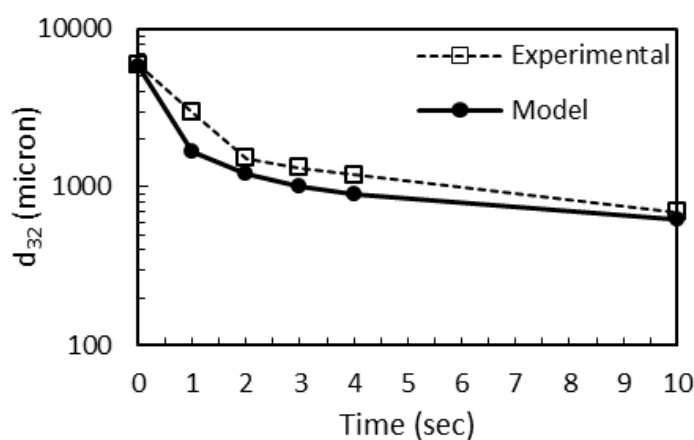


Figure 4.4.7 a) d_{32} and b) σ/d_{32} for surfactant A at 900 RPM fit using all surfactant A experiments.

Figure 4.10 shows the d_{32} and σ/d_{32} parameters of the distribution for both the model and experiments for surfactant A at 600 RPM. The results show almost no improvement of the fit when compared to the predicted values from parameter estimation 1. Both cases over predict the amount of breakage for mixing times below 10 seconds. Additionally, both cases are unable to predict the normalized variance at short mixing times.

a)



b)

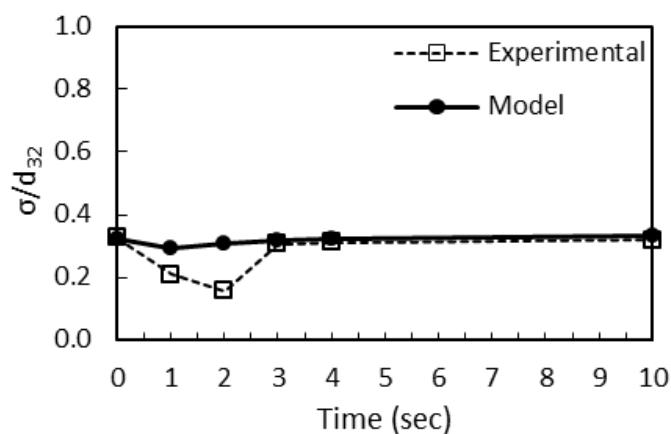


Figure 4.4.8 a) d_{32} and b) σ/d_{32} for surfactant A at 600 RPM fit using all surfactant A experiments.

The results of the full experimental fit for surfactant A show that the population balance model does an excellent job fitting the experimental data. The largest deviations between the model and experiments occur at low mixing times where the model overbreaks the material. The results indicate that the breakage kernel may slightly overemphasize particle size. The impact efficiency model uses the Stokes number as the characteristic dimensionless group. The x^2 term in the Stokes number predicts a strong

dependence on particle size. An over emphasis of particle size would increase the breakage rate at short mixing times when particles are large.

The results of parameter estimation 1 and 2 demonstrate that the model correctly accounts for the effect of impeller tip speed on the breakage kinetics. Fitting the entire experimental data set shows almost no improvement in the model compared to fitting to only the 1200 RPM data and predicting the size distributions at lower impeller speeds. However, the two parameter estimations produce different values of Stk^* and q that lie outside of each other's 95% confidence intervals. The results demonstrate that covariance exists between the fitted parameter. Additionally, the variation in the fitted parameters between the two cases is not as strong as the variation due to changing impeller tip speed.

Figure 4.11 shows the results of the efficiency function (eqn. 4.5) as a function of particle size and velocity. The three curves represent the experimental conditions for parameter estimation 1 and parameter estimation 2. The results show that the difference in the fitting parameters between the two cases has a very small effect on the impact efficiency. For the parameter range of interest, the impact efficiency is never higher than approximately 0.65. For particles of a size below 1000 μm the impact efficiency is around 0.01. The efficiency curve demonstrates that under the experimental conditions, less than 2% of possible impacts occur. The nuclei are almost entirely carried in the streamlines of the bulk powder and do not impact the impeller pins.

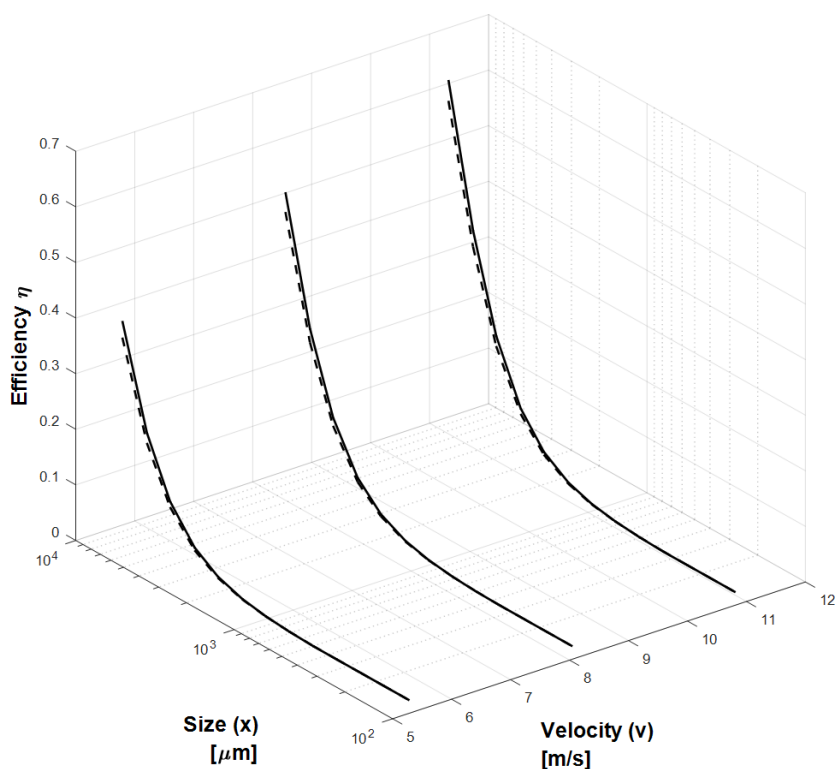


Figure 4.4.9 Efficiency plot as a function of particle size and velocity. Solid line is values from parameter estimation 1 and dotted line is values from parameter estimation 2.

4.4.3 Parameter Estimation 3

The results from paste A demonstrated that it is sufficient to perform parameter estimation using only the 1200 RPM impeller speed experiments. Based on the definition of the breakage kernel, the estimated parameters λ_l and Stk^* are not material dependent. The third estimated parameter q is expected to be material dependent. Surfactant B has a similar density to surfactant A. Therefore, the only parameter that must be estimated is the power law parameter q . The values of λ_l and Stk^* are kept the same as the values found in parameter estimation 1 for surfactant A.

Table 4.4 shows the value of the estimated parameters for surfactant B. The value of λ_1 and Stk^* are taken from table 4.2. The value of q is estimated using the 1200 RPM experimental data for Surfactant B. The result shows that the value of q is a lower negative value than that of surfactant A. This indicates that surfactant B breaks into larger particles than surfactant A. This is consistent with the higher yield stress of surfactant B at room temperature after the surfactant has cooled.

Table 4.4 Surfactant B estimated parameter q using 1200 RPM data. Other parameters are from parameter estimation 1.

Parameter	Estimated value \pm 95% CI	95% T (ref T: 1.653)
λ_1	0.00330	-
Stk^*	0.603	-
q	-1.816 ± 0.085	21.47

Figure 4.12 shows the model prediction and experimental results for surfactant B at 1200 RPM. The model does not predict that experimental distribution as well as for surfactant A. The predicted values at low mixing times show stronger agreement with experiments than the predictions for longer mixing time. This is in contrast to the results for surfactant A which showed model prediction improve at longer mixing times. At longer mixing times the model initially under predicts the amount of breakage but then over predicts the breakage for the 10 second experiments. However, the model is able to distinguish different mixing times and provides an acceptable prediction of the experimental data. Figure 4.13 shows the d_{32} and σ/d_{32} parameters of the distributions in figure 4.12. The results show that the experimental mean size stops decreasing around 3 seconds of mixing time. The model on the other hand continues to decrease and over predict the normalized variance.

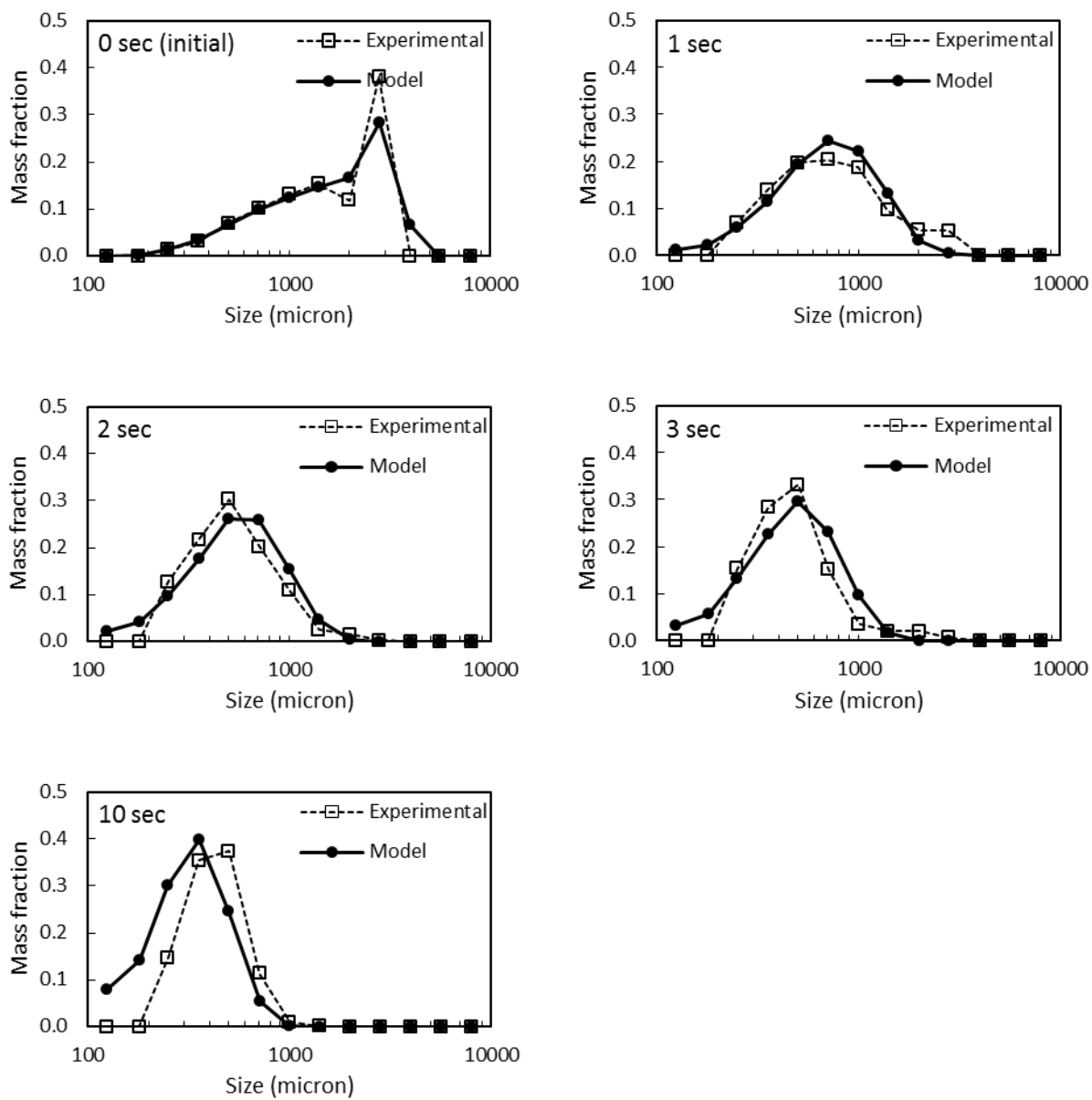


Figure 4.4.10 Particle size distributions for model and experiments for Surfactant B at 1200 RPM fit using all experiments.

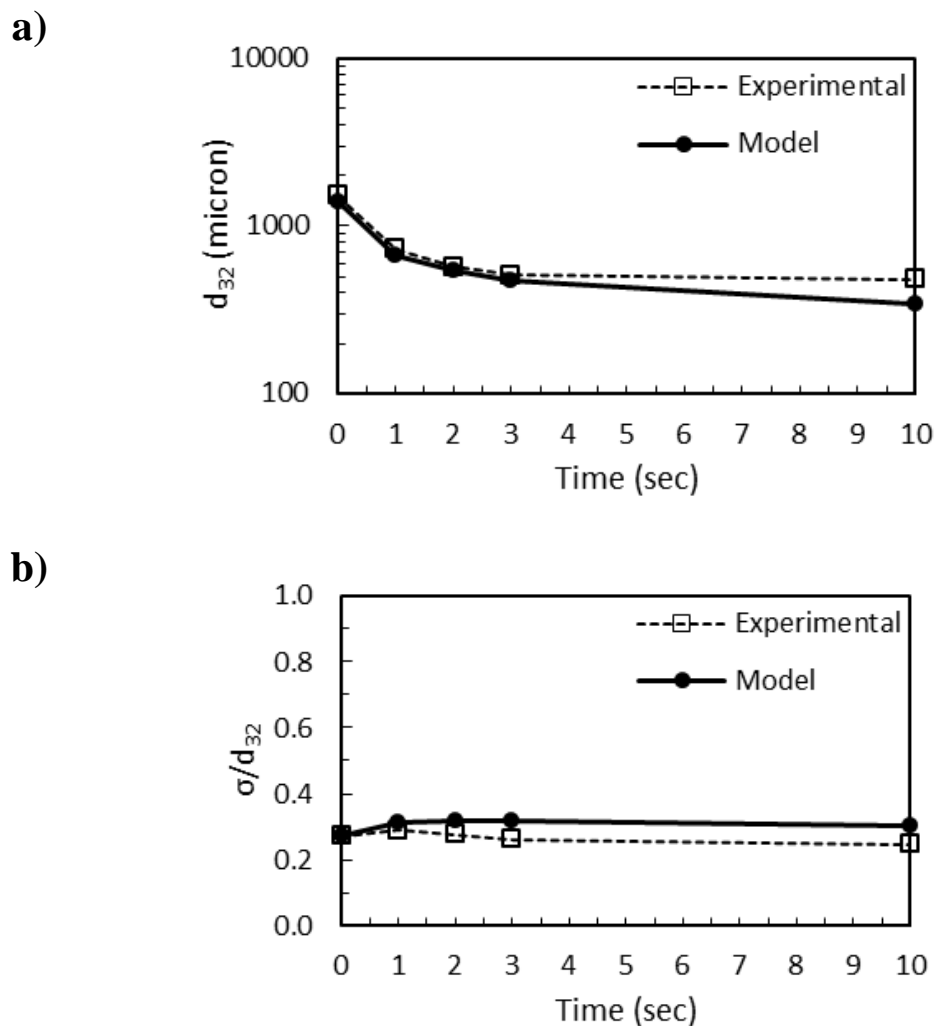
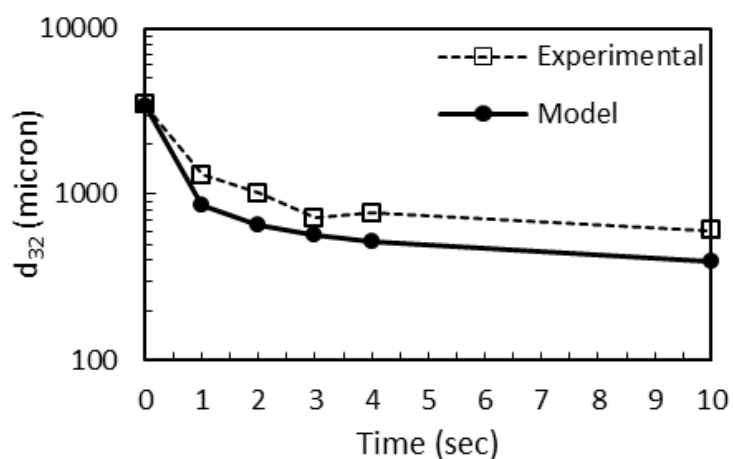


Figure 4.4.11 a) d_{32} and b) σ/d_{32} for surfactant B at 1200 RPM with λ_l and Stk^* from parameter estimation 1 and q estimated from surfactant B experiments at 1200 RPM.

Figure 4.14 shows the model prediction and experimental results for surfactant B at 900 RPM. At this impeller speed, the model over predicts breakage at all mixing times, but accurately predicts the normalized variance. The mean size results are over predicted at the first second of mixing time. After the first second, the results continue to decrease but at close to the same rate as the experiment. Improving the prediction of the first second may allow the model to accurately model this experimental condition.

a)



b)

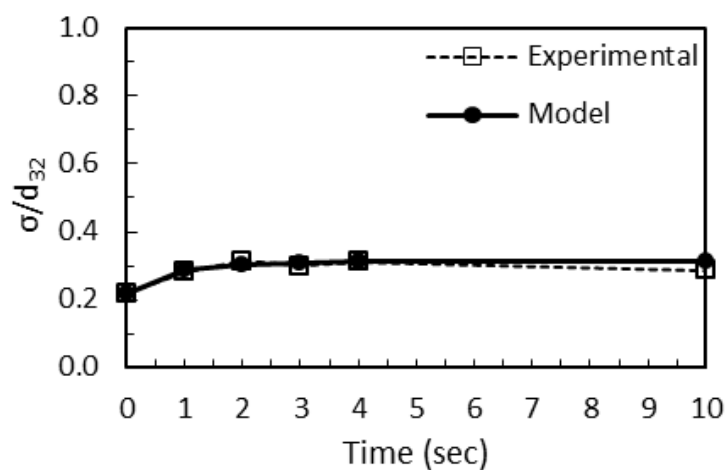
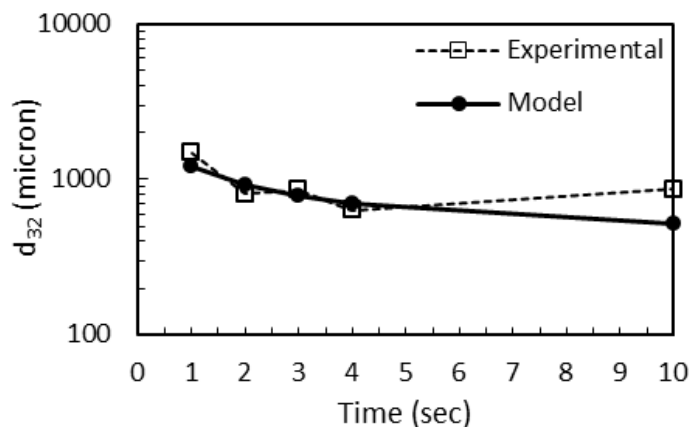


Figure 4.4.12 a) d_{32} and b) σ/d_{32} for surfactant B at 900 RPM with λ_l and Stk^* from parameter estimation 1 and q estimated from surfactant B experiments at 1200 RPM.

Figure 4.15 shows the model prediction and experimental results for surfactant B at 600 RPM. The results for 600 RPM are similar to those of the 1200 RPM case. The model initially under predicts breakage but over predicts at long mixing times. The experimental results show almost no change in particle size between the 4 second and 10 second mixing times. This result cannot be captured by the breakage kernel proposed

which predicts the breakage rate to reduce but still be non-zero for the conditions in the granulator. Interestingly, the normalized variance was able to be predicted by the model.

a)



b)

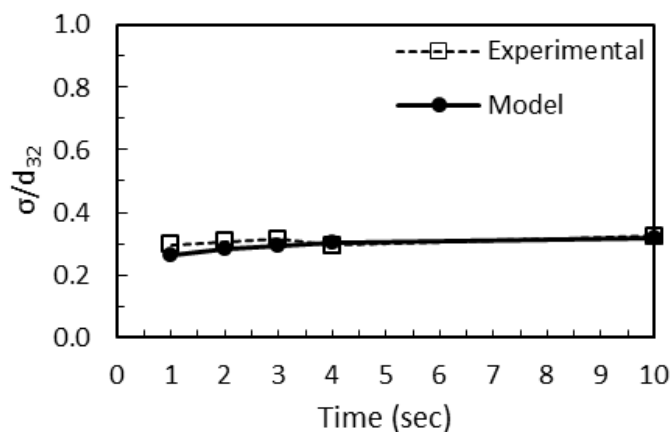


Figure 4.4.13 a) d_{32} and b) σ/d_{32} for surfactant B at 900 RPM with λ_l and Stk^* from parameter estimation 1 and q estimated from surfactant B experiments at 1200 RPM.

The results of the parameter estimation of q for surfactant B show a qualitative and somewhat quantitative agreement with experiments. In general, the results of the surfactant B parameter estimation do a good job predicting the particle size distribution at low mixing times but over predict the amount of breakage observed in the experiment as mixing time increases.

The longer mixing times show a greater deviation between the model and experiment. One reason for this is the large reduction in breakage rate observed in the experimental results. The change in particle size between 4 seconds and 10 seconds of mixing time is much lower for surfactant B than surfactant A. This is due to the difference in rheology of the surfactants. The yield stress of surfactant B increases by an order of magnitude more than surfactant A during cooling. As the material cools in the granulator and increases in yield stress, weak impacts that previously broke the nuclei are no longer sufficient to continue breakage. In this case the initial assumption that $P_{break} = I$ may no longer be valid.

The efficiency based breakage kernel cannot account for the second order reduction in breakage observed in surfactant B. However, the model is able to accurately predict the particle size distribution at lower mixing times before surfactant cooling has occurred. In order to improve the model for surfactant B, the model will need to take into account the cooling rate of the granule nuclei. The temperature dependence of surfactant yield stress would then be characterized and implemented into the model.

4.5 Conclusions

A new semi-empirical breakage kernel has been introduced that uses collision frequency and efficiency instead of granule strength to predict granule nuclei breakage. The model is based off of filtration theory using the Stokes number. The kernel incorporates several physically measurable parameters and is dependent on impeller geometry, impeller speed, and particle size.

The results of the fitting parameters indicate that the impact efficiency of the granulator is less than 0.02 for particle below 1000 μm in size. This means that the pin

mixer geometry is actually very inefficient at breaking small nuclei. However, the pin mixer is very effective at breaking large oversized nuclei.

The parameter estimations determined the three fitting parameters with narrow confidence intervals, indicating a high confidence in the parameter values. Additionally, the model was demonstrated to accurately account for the effect of impeller tip speed. The results determined by predicting the particle size distribution using data from a single impeller were found to match the experiments just as well as results obtained using the entire experiment set. The model also was able to capture the breakage of a different surfactant, surfactant B, by only fitting the breakage distribution parameter, q , leaving the other two parameters the same as for surfactant A.

The collision efficiency based breakage kernel has been demonstrated to accurately depict the physics of the pin mixer. Improvement of the breakage model should account for the effect of material strength on the breakage rate. Changing material strength cannot be accounted for in the current model. A functional form for P_{break} dependent on the Stokes deformation number will be necessary for cases where P_{break} is no longer equal to 1. However, the addition of another equation to the breakage model will also introduce additional fitting parameters. Increasing the number of fitting parameters in the model reduces the predictability of the model and requires more experiments to calibrate.

CHAPTER 5. PREDICTING LOCAL SHEAR IN POWDER FLOW USING DEM: EFFECT OF SIMULATION PARAMETERS

5.1 Introduction

In chapter 3 and 4 the mechanical dispersion of surfactant was evaluated in the high shear pin mixer. The results indicated that the primary variable governing surfactant breakage is the number of revolutions of the impeller. However, breakage of surfactant could occur by both impact and shear forces within the granulator. In order to determine whether breakage by shear is an important mechanism in the pin mixer, the shear rate within the granulator must be characterized. However, due to the complex nature of the pin mixer it is difficult to decouple impact and shear effects within the pin mixer.

In chapter 2 DEM simulations were shown to be useful in characterizing granular flow. Work by Hare et. al.^{107,108} characterized the shear stress within a vertical high shear mixer. However, for the case of mechanical dispersion of the surfactant the stress of interest is not just the stress profile in the bed, but also the stress on the larger surfactant nuclei.

This chapter focuses on the stress transmission between a bed of primary particles and a single larger particle with the same properties as the bed. The objective is to characterize the unit shear cell system, and the stress applied to a large surfactant sphere in the bulk material. The objective is accomplished by:

1. Building a DEM simulation based on a unit shear cell with a single large ‘surfactant’ sphere surrounded by a bed of smaller bulk particles.
2. Characterizing the actual shear flow and stress within the shear cell.
3. Characterizing the stress applied to the large particle from the bulk material.
4. Evaluating the effect of simulation parameters on the results to determine sensitivity of the stress to the material properties input to the model.

Special attention is given to the material properties and the effects that they have on the stress profile of the larger particle. The stress profile on a large particle is important in determining the difference between the macroscopic shear rate and the actual shear rate observed on the larger particle. This stress on the particle can then be used to determine how a particle of the same size would deform or break in shearing environment using criteria such as von Mises yield criterion.

5.2 Methods

DEM simulations were constructed in LIGGGHTS open source DEM software. The simulation results were then characterized using custom code to derive information concerning the velocity profile and stress inside the unit cell.

5.2.1 Simulations

The model geometry was a shear unit cell similar to that used by Kholá and Wassgren¹²⁵ as seen in figure 5.1. The shear cell contained one large particle of interest and 1500 bulk particles of a fixed size ratio. The volume of particles was chosen to form a shear cell region in the approximate shape of a cube with a side length, L , of 12 bulk particle diameters. The walls of the cell consisted of an upper and lower wall made of particles with the same properties as the bulk particles. The upper and lower wall was

oriented with gravity in the $-y$ direction. The x and z direction had periodic boundaries, and shear flow was in the x direction. Shear flow was developed by moving the upper and lower wall in the x direction with opposite but equal velocity (v_{wall}). Each wall was a 12×12 lattice with 4 fins each one particle diameter high spaced three particle diameters apart. The fins promote particle flow in the bulk material. The lower wall was fixed in the y and z direction and moved in the $-x$ direction. The upper wall was fixed in the z direction and moved in the $+x$ direction. To allow the particle bed to expand and contract during flow, the y direction was not fixed and instead a constant force, F_c , was applied to the top wall in the $-y$ direction.

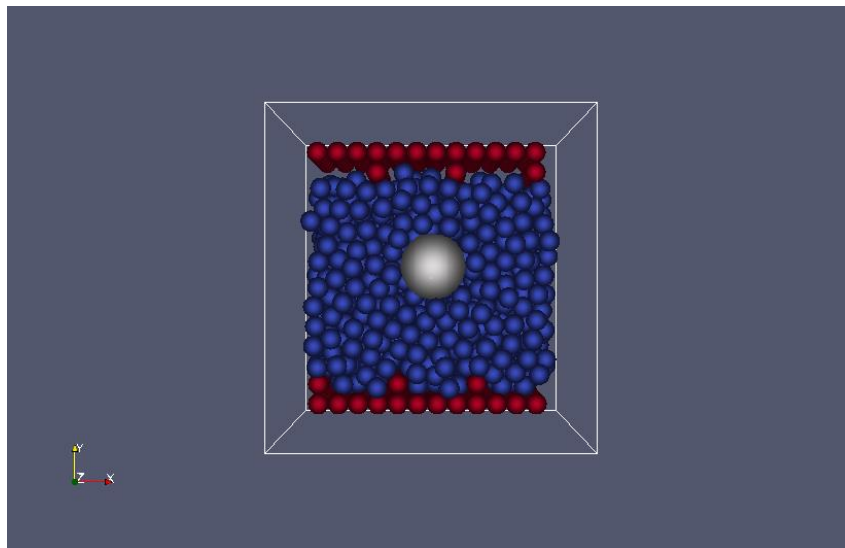


Figure 5.2.1 Shear unit cell model based on Khola and Wassgren¹²⁵. Large particle of interest can be seen in the center of the bed in white, the bulk particles in blue, and the wall particles in red.

DEM simulations were carried out using the open source software package LIGGGHTS version 3.0.2. The simulation used the Hertz pair interaction calculated from assumed material properties with tangential interaction enabled and using the constant directional torque (CDT) rolling friction model. DEM parameters used in the simulation

are summarized in table 5.1 and 5.2. Table 5.1 contains the parameters used to define the shear unit cell and were not varied between simulations. The size of the large particle of interest was 0.01 m which corresponds to the largest size of surfactant particles in the pin mixer. However, the bulk material size was 3000 μm which is much greater than the 10 μm zeolite size. This large size was used to reduce the number of particles and the simulation time. Table 5.2 contains the varied simulation parameters and material properties of the particles.

The shear cell model was built in 5 steps. First the lower wall was added. Second a number fraction, χ , of the bulk particles was added and allowed to fall under gravity on top of the lower wall. Third, the particle of interest was added in the center of both the x and z directions of the cell and allowed to fall onto the bed. Fourth the remaining fraction $(1 - \chi)$ of bulk particles were added and allowed to fall on top of the particle of interest and the bed. Fifth, the upper wall was added and compressed onto the top of the shear using a consolidation force (F_c).

Table 5.1 Constant parameters of the unit cell model design.

Unit Cell Parameter	Value
Diameter Ratio (ξ)	0.3
Large Particle Diameter (D)	0.01 m
Primary Particle Diameter (d)	0.003 m
Shear Cell Length (L)	12*d
Number of primary particles (n_p)	1500
Gravity (g) in $-y$ direction	1*g
Consolidation Force per particle (F_c)	$-5 \cdot 10^{-3}$ N
Shear time steps (t_{shear})	1000000

Table 5.2 Varied Simulation parameters and material properties.

Simulation Parameter	Parameter Range	Base Case
Target shear rate (γ)	0.1 – 10 s ⁻¹	1 s ⁻¹
Bed fraction below particle of interest (χ)	0.3 – 0.6	0.4
Particle density (both particle types) (ρ)	2000 kg/m ³	2000 kg/m ³
Young's modulus (particle of interest) (E_i)	1*10 ⁷ Pa	1*10 ⁷ Pa
Young's modulus (bulk particles) (E_{bulk})	1*10 ⁶ - 1*10 ⁸ Pa	1*10 ⁷ Pa
Poisson's ratio (both particle types) (ν)	0.25	0.25
Coefficient of restitution all interactions (ϵ)	0.75	0.75
Coefficient of friction (all interactions) (μ)	0.5	0.5
Coefficient of Rolling Friction (all interactions) (μ_r)	0.1	0.1
Time step (Δt)	maximum 5*10 ⁻⁶ s	5*10 ⁻⁶ s

The diameter ratio, ξ , is defined in eqn. 5.1 as the ratio between the bulk particle diameter (d) and the particle of interest diameter (D).

$$\xi = \frac{d}{D} \quad (5.1)$$

The target shear rate in the unit cell was used to determine the wall velocity using eqn. 5.2:

$$v_{wall} = \frac{1}{2}(\gamma * L) \quad (5.2)$$

where L is the length, depth, and assumed height of the shear cell, and v_{wall} is magnitude the velocity applied to both the upper and lower wall but in opposite directions.

The simulation time step was calculated to keep the Raleigh time below 15% using eqn. 5.3:

$$\Delta t = \begin{cases} 5 \times 10^{-6} \text{ s}, & \gamma < 1 \text{ s}^{-1} \\ (5 \times 10^{-6} \text{ s}) * (1 \text{ s}^{-1}/\gamma), & \gamma \geq 1 \text{ s}^{-1} \end{cases} \quad (5.3)$$

where Δt is the time step length and γ is the shear rate of the cell. The maximum time step length was set to $5 \times 10^{-6} \text{ s}$ due to the compression force on the top wall. For shear rates greater than 1 s^{-1} , the time step was reduced. The number of time steps was not increased with varying time steps producing different total simulation times at different shear rates. However, the total distance traveled by the walls is constant for all shear rates except 0.1 s^{-1} .

Several material parameters were varied to determine their effect on the shear flow of the system and stress on the particle of interest. The varied parameters included the Young's Modulus of the bulk particles, E_{bulk} , the coefficient of restitution, ε , which was the same for all particle interaction types, the coefficient of friction, μ , and coefficient of rolling friction μ_r which were the same for all particle interaction types.

For each simulation, data was collected every 1000 time steps in two reports. The first report contained particle information such as position, velocity, and angular velocity. The second report contained all pair wise interactions in the simulation.

5.2.2 Post Processing

Simulation results were characterized using a combination of python scripts, pizza.py, and MatLab. The characterization included the actual shear profile in the unit cell, the stress in the unit cell, and the stress observed on the particle of interest.

The actual shear profile was characterized by dividing the unit cell vertically into slices with a height equal to the diameter of the bulk particles. In each slice the velocity in the x direction was averaged over all the particles in the slice. The velocity profile was then normalized to the produce a velocity profile from 0 to 1.

The hydrostatic and deviatoric stress in the unit cell was characterized by combining the approach described by Hare et. al.¹⁰⁷ and Göncü et. al.¹²⁶. The pressure and deviatoric stress was calculated for each vertical slice used in the actual shear profile. The normal stress was calculated for each cell using eqn. 5.4:

$$\sigma_{ij} = \frac{1}{V} \sum_{k=1}^N n_{i,k} f_{j,k} r_p \quad (5.4)$$

where σ_{ij} is the ij component of the stress tensor, V is the volume of the cell, N is the total number of interactions in the cell, $n_{i,k}$ is the normal vector of the k^{th} contact, $f_{j,k}$ is the k^{th} contact force, and r_p is the mean radius of the two particles in the interaction. From the stress tensor, the pressure (p) is then:

$$p = -\frac{\sigma_{xx} + \sigma_{yy} + \sigma_{zz}}{3} \quad (5.5)$$

and the deviatoric stress, τ_D , is:

$$\tau_D = \frac{\sqrt{(\sigma_{xx}-\sigma_{yy})^2 - (\sigma_{xx}-\sigma_{zz})^2 - (\sigma_{yy}-\sigma_{zz})^2}}{\sqrt{6}} \quad (5.6)$$

where σ is the Cauchy stress tensor.

The stress tensor of the large particle of interest was calculated from eqn. 5.7:

$$\sigma_{ij} = \sum_{k=1}^N \frac{n_{i,k} f_{j,k}}{A_k^{contact}} \quad (5.7)$$

where $A_k^{contact}$ is the contact area of the interaction. The stress tensor was then used to determine the hydrostatic and deviatoric stress on the particle with eqns. 5 and 6.

The von Mises stress was determined to compare the predicted necessary yield stress to predict breakage in the shear cell. The von Mises stress is defined as:

$$\sigma_y = \sqrt{3J_2} \quad (5.8)$$

where σ_y is the yield stress required to resist deformation and J_2 is the second invariant of the stress tensor defined as:

$$J_2 = \frac{1}{2} s_{i,j} s_{j,i} \quad (5.9)$$

where $s_{i,j}$ is the i,j^{th} component of the deviatoric stress tensor defined as:

$$s_{i,j} = \sigma_{ij} - p\delta_{i,j} \quad (5.10)$$

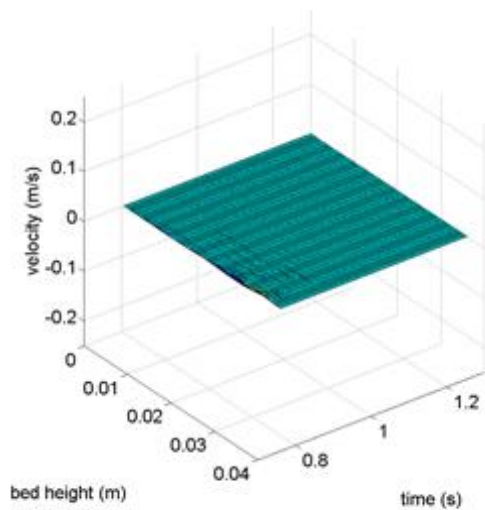
where $\delta_{i,j}$ is the kronecker delta.

5.3 Results and Discussion

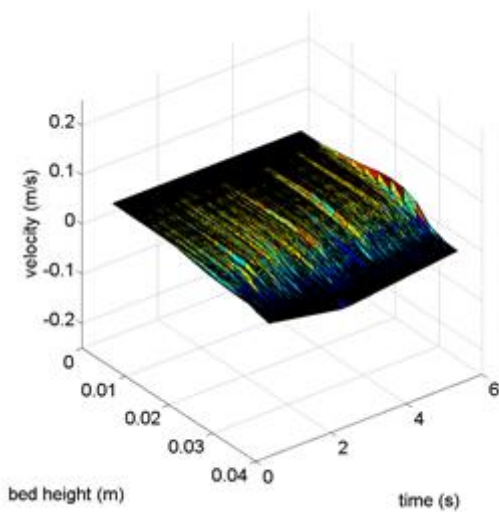
5.3.1 Shear Flow

Typical results for the shear profile of the unit cell throughout the simulation are shown in figure 5.2. The shear profile is calculated every 5000 time steps and shows the variation in the shear profile. Even at low shear rates, particle velocity can rapidly shift from one sampling time to another. This is consistent with the particle bed building up a stress network and then failing inducing particle flow. Additionally, it is observed that the

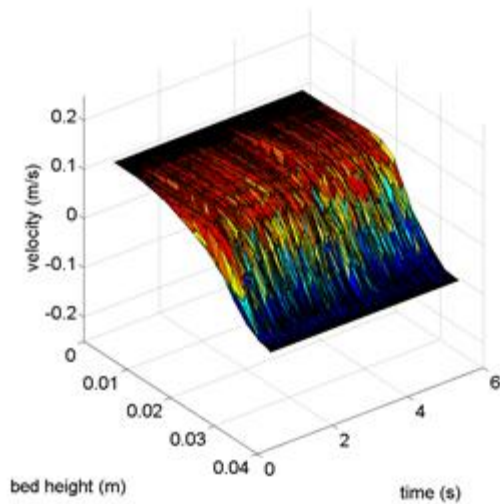
shear profile is not linear. Instead, the shear profile displays a shear band that is produced near the top of the shear cell. The top wall of the cell generates the shear band for two reasons. Firstly, the gravitational load is lower on the top particles, and secondly, it is not fixed in the y direction but instead can allow the bed to dilate.



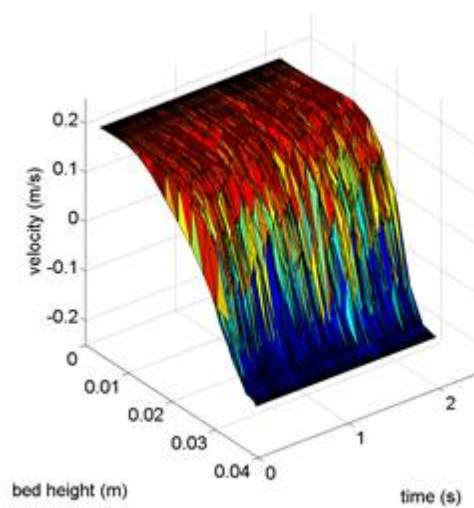
a)



b)



c)



d)

Figure 5.3.1 Shear profile every 5000 time steps for the base case conditions at shear rates a) 0 s^{-1} b) 1 s^{-1} c) 5 s^{-1} d) 10 s^{-1}

Figure 5.3-5.6 shows the parameter effects on the shear profile of the shear cell.

The figures demonstrate shear band formation towards the unfixed upper wall of the

shear cell as seen in figure 2. The dimensionless bed heights of 0 and 1 correspond to the lower and upper walls respectively and move at a known fixed velocity. The lower wall is the reference point for zero velocity.

Figure 5.3 shows the effect of shear rate on the velocity profile at the base case conditions. As the shear rate increase, momentum is transferred farther onto the shear cell. Additionally, the higher shear rates show a lower difference in velocity between the upper wall and the bed. However, the height of the shear band is consistent for all shear rates and is produced at dimensionless heights between 0.5 and 0.85. This is clearly seen in figure 5.3 b which shows how the actual shear rate in the bed is a function of both bed height and the overall shear rate.

Figure 5.4 shows the effect of the bed fraction below the particle of interest on the velocity profile at the base case conditions. As the bed fraction increases, momentum does not propagate as far into the bulk material. This effect is the result of the large particle of interest physically blocking motion in the bed. Momentum that would normally cause the bulk material to flow is instead used to move the large particle of interest through the bed. Additionally, the shear band forms between dimensionless bed height of 0.5 to 0.85 similar to the previous case. The location of the shear band decreases with decreasing height of the large particle.

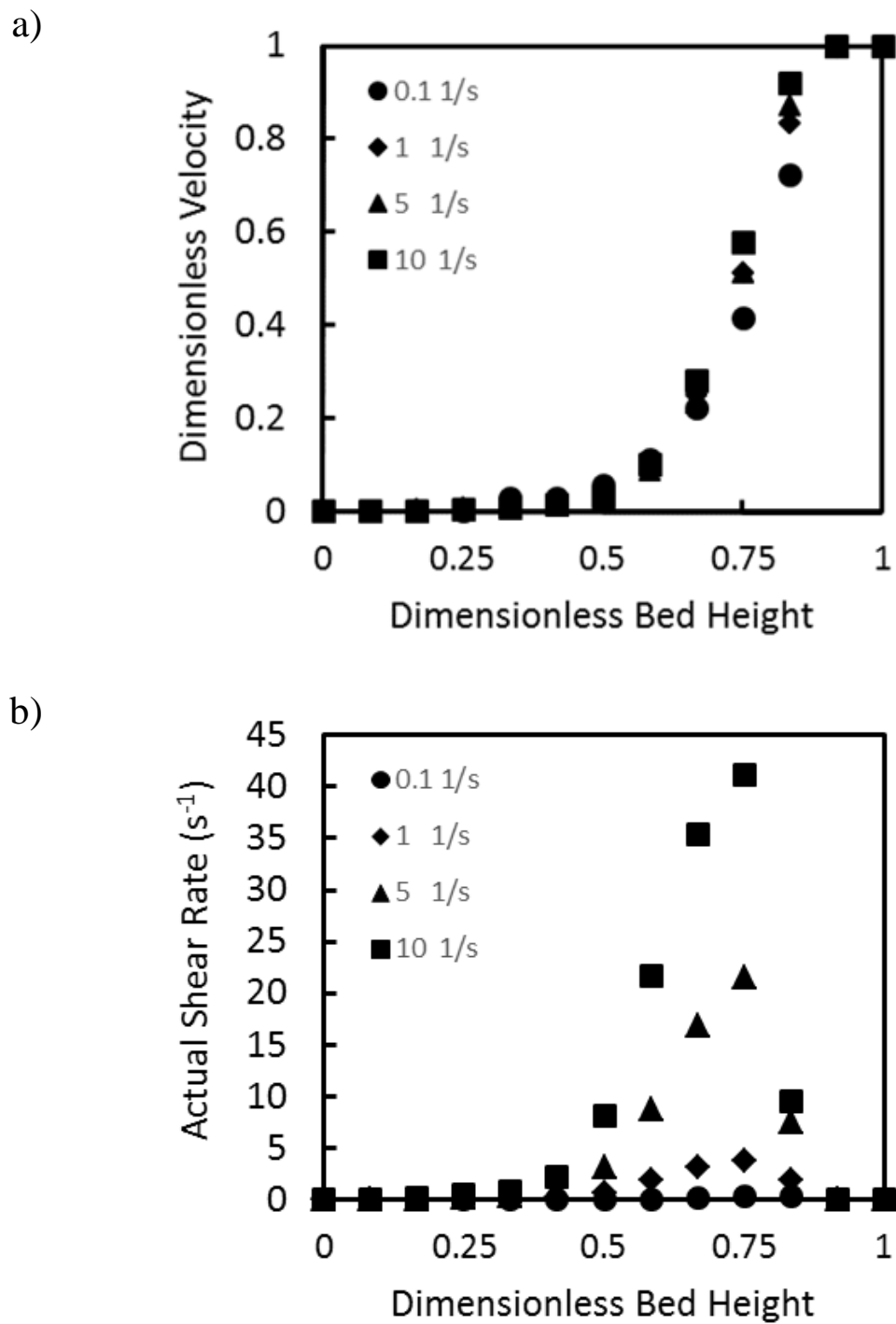


Figure 5.3.2 a) Dimensionless velocity and b) actual shear rate versus dimensionless bed height as a function of shear rate (γ) with the remaining parameters at base case conditions.

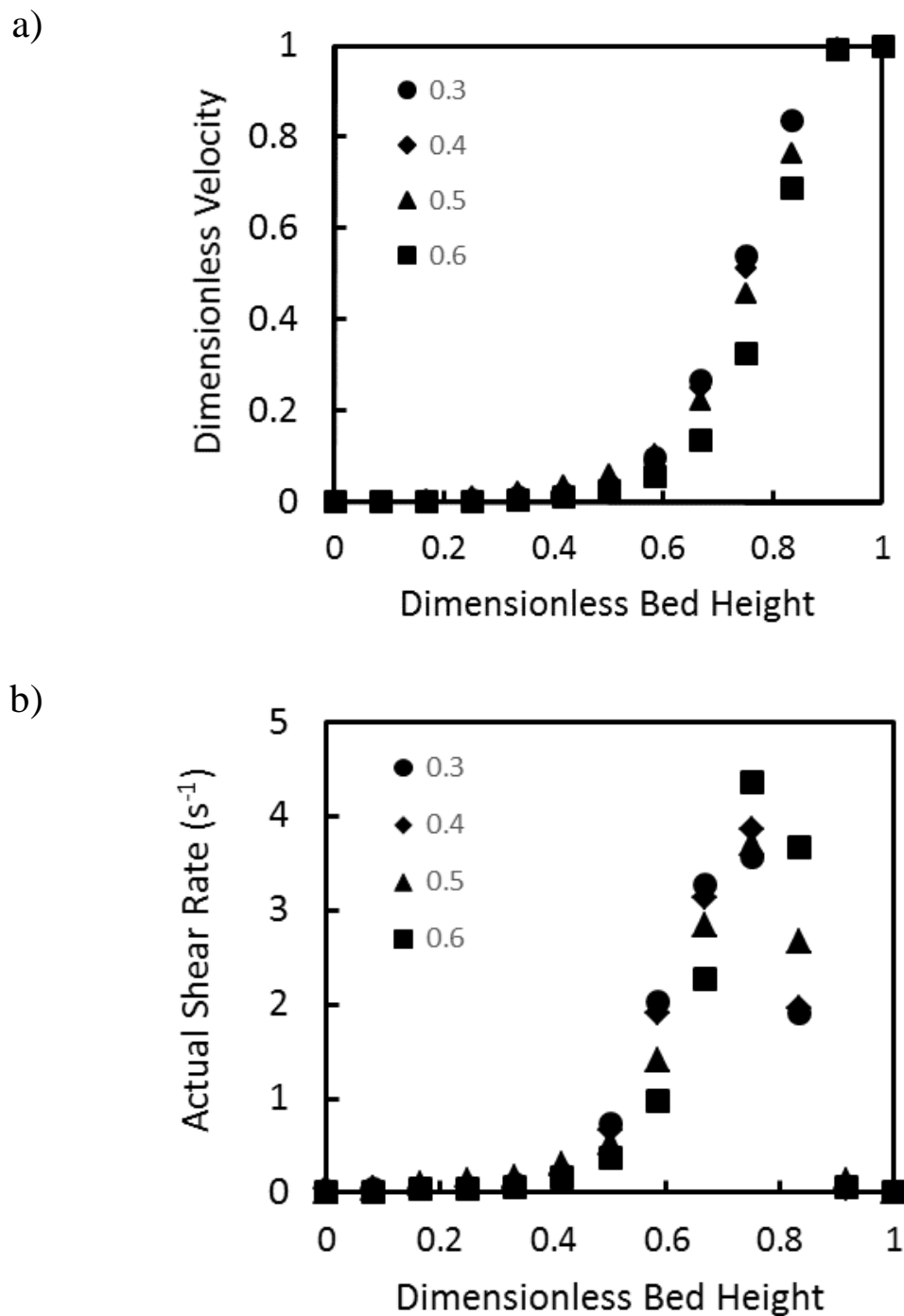


Figure 5.3.3 a) Dimensionless velocity and b) actual shear rate versus dimensionless bed height as a function of bed fraction(χ) with the remaining parameters at base case conditions.

Figure 5.5 shows the effect of the Young's modulus of the bulk particles on the velocity profile at the base case conditions. As the Young's modulus decrease, velocity propagates further into the shear cell. This is explained by the higher Young's modulus bed reducing deformation and causing the upper wall to slip across the surface of the bed. Wall slip is clearly seen at a dimensionless bed height of 0.85. At this height, the lowest Young's modulus particle bed is moving at nearly the same velocity as the upper wall. The stiffer particles at 1×10^8 Pa show a much greater decrease in velocity with height. The results at 5×10^7 Pa and 1×10^8 Pa are nearly consistent indicating that a critical value of the Young's modulus has been reached and the failure plane is near the upper wall.

Figure 5.6 shows the effect of the coefficient of friction on the velocity profile at the base case conditions. The coefficient of friction has the most dramatic of the parameters over the range explored in this study. Lower friction coefficients allow particles to flow more freely. As a result, the velocity profile at low friction coefficients shows the furthest propagation of momentum. At a friction coefficient of 0.1, the top quarter of the bed moves almost as plug flow before reducing in velocity. In this case the shear band is deeper into the bed extending from a dimensionless bed height of 0.75 down to 0.5. The large particle of interest is less effective at impeding the flow of bulk material at the low friction coefficients. High friction coefficients result in slip of the upper wall resulting in the top of the bed moving at only half the wall velocity.

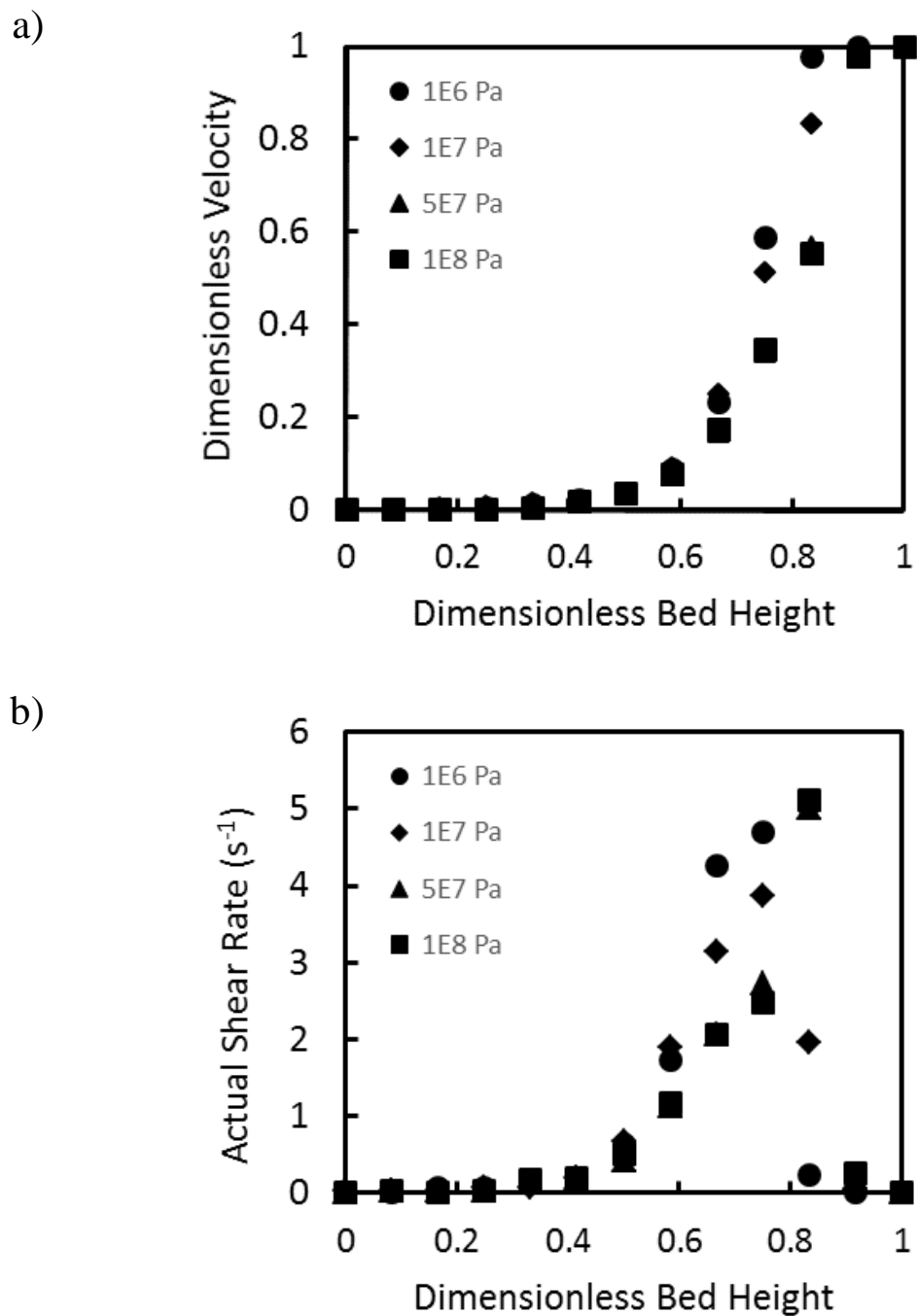


Figure 5.3.4 Dimensionless velocity and b) actual shear rate versus dimensionless bed height as a function of Young's Modulus (E) with the remaining parameters at base case conditions.

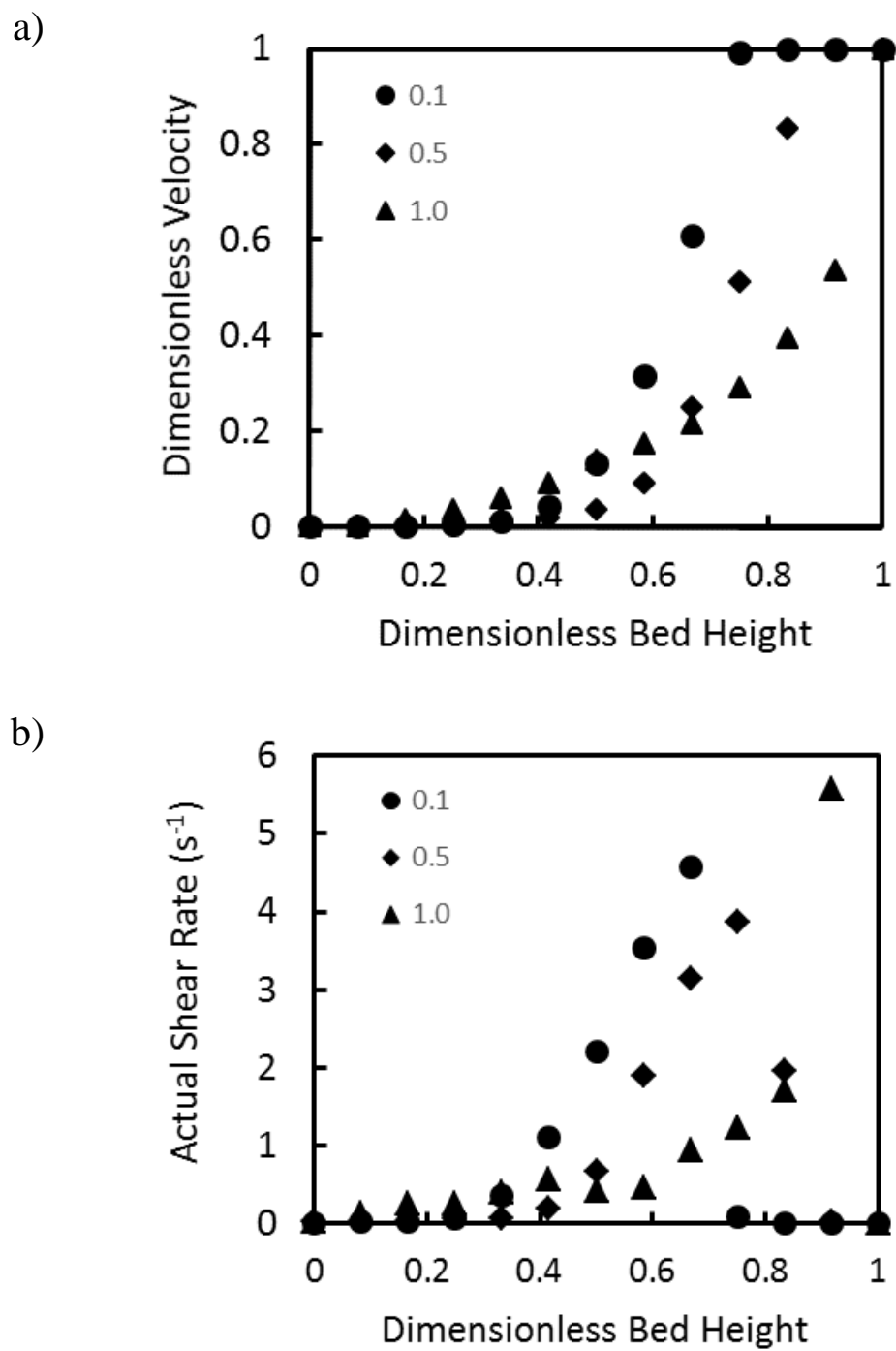


Figure 5.3.5 Dimensionless velocity and b) actual shear rate versus dimensionless bed height as a function of the friction coefficient (μ) with the remaining parameters at base case conditions.

For all velocity profiles, the results showed the formation of a shear band in the upper third of the shear cell. The material at the bottom of the shear cell moved in unison with the lower wall exhibiting almost no shear behavior. The results indicate that the location of the particle of interest is important in the shear cell since if it is near bottom it will simply move in plug flow and experience only a normal stress. Additionally, the actual shear rate in the bed reached a peak value of approximately 5 times the overall target shear rate of the unit cell.

5.3.2 Shear Cell Stress

Figures 5.7 – 5.10 show the effect of parameters on the pressure and deviatoric stress in the shear cell. The stress is calculated using eqn. 4. The results at the top and bottom of the shear cell are omitted because they correspond to the upper and lower wall.

Figure 5.7 shows the effect of shear rate on the average pressure and deviatoric stress in the shear cell at base case conditions. The results show that pressure and deviatoric stress are not strong functions of bed height. The effect of increasing shear rate shows a large difference between 0.1 s^{-1} and the higher shear rates. At a shear rate of 0.1 s^{-1} the deviatoric stress and pressure are much lower than at the higher shear rates between 1.0 and 10 s^{-1} . The result is similar to the effect on the velocity profile which demonstrated a large change between shear rates of 0.1 s^{-1} and 1 s^{-1} but a smaller change for shear rates above that value.

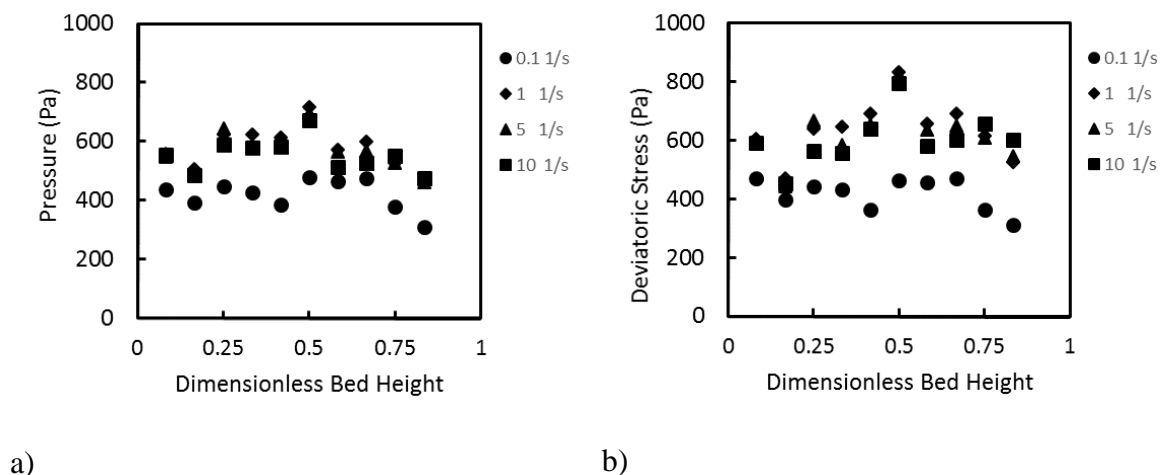


Figure 5.3.6 a) Pressure and b) deviatoric stress versus dimensionless bed height as a function of shear rate with the remaining parameters at base case conditions.

Figure 5.8 shows the effect of bulk bed fraction below the particle of interest on the average pressure and deviatoric stress in the shear cell at base case conditions. Once again the effect of bed height is not as strong with pressure slightly reducing near the top of the shear cell. However the effect of bed height fraction shows an interesting result. For each bed height, the largest pressure and deviatoric stress is found at the approximate location of the large particle. For example at a bed fraction of 0.6 the peak stress is at the dimensionless bed height of 0.66, and at a bed fraction of 0.3 the peak stress is at the dimensionless bed height of 0.42. The result indicates that the placement of the largest particle corresponds with an increase in pressure and deviatoric stress as momentum is transferred by the largest particle deeper into the bed. The peak stress is typically 200 Pa higher than the stress in the nearby height bins. Additionally, higher placement of the large particle corresponded with lower pressure and deviatoric stress. This is a result of the large particle residing almost entirely in the shear band and promoting motion of plug flow seen in figure 5.4 in the top of the shear cell. Additionally without the weight of

additional bulk material acting on the large particle, the pressure experienced by the large particle is lower, the higher it is in the shear cell.

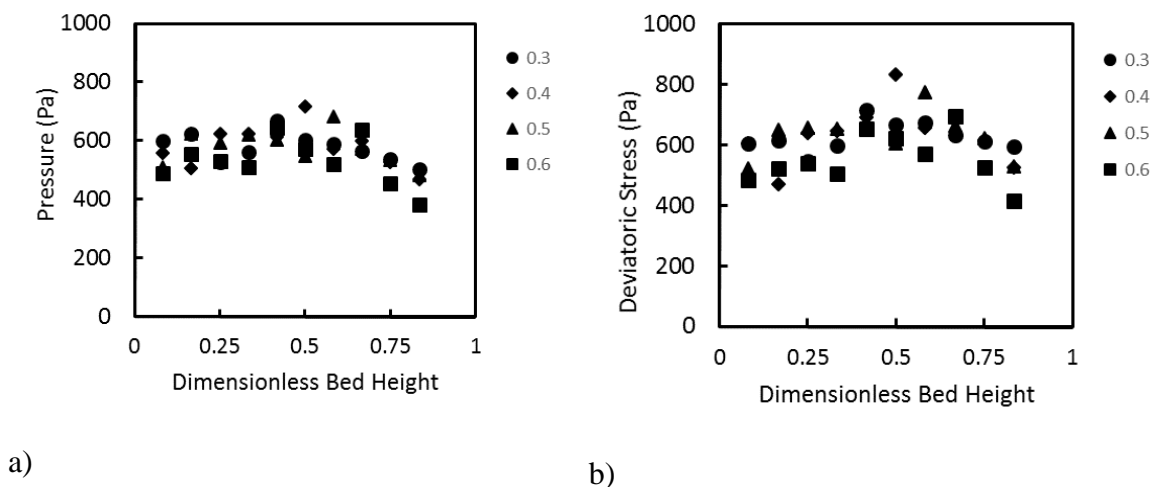


Figure 5.3.7 a) Pressure and b) deviatoric stress versus dimensionless bed height as a function of bed fraction below the particle of interest with the remaining parameters at base case conditions.

Figure 5.9 shows the effect of Young's modulus of the bulk material on the average pressure and deviatoric stress in the shear cell at base case conditions. In general, higher Young's modulus of the bulk material corresponds with lower pressure and deviatoric stress. In the shear band, the pressure and deviatoric stress steadily decrease as bed height increases. At a Young's modulus of 1×10^6 Pa, the results show a drop of about 400 Pa in deviatoric stress and pressure at a bed height of 0.83. This corresponds with the large decrease in shear rate observed in figure 5.5 b. The shear rate in the bed appears to have a strong effect on both the pressure and deviatoric stress. The relationship shows the expected trend with lower shear rates generating lower stress.

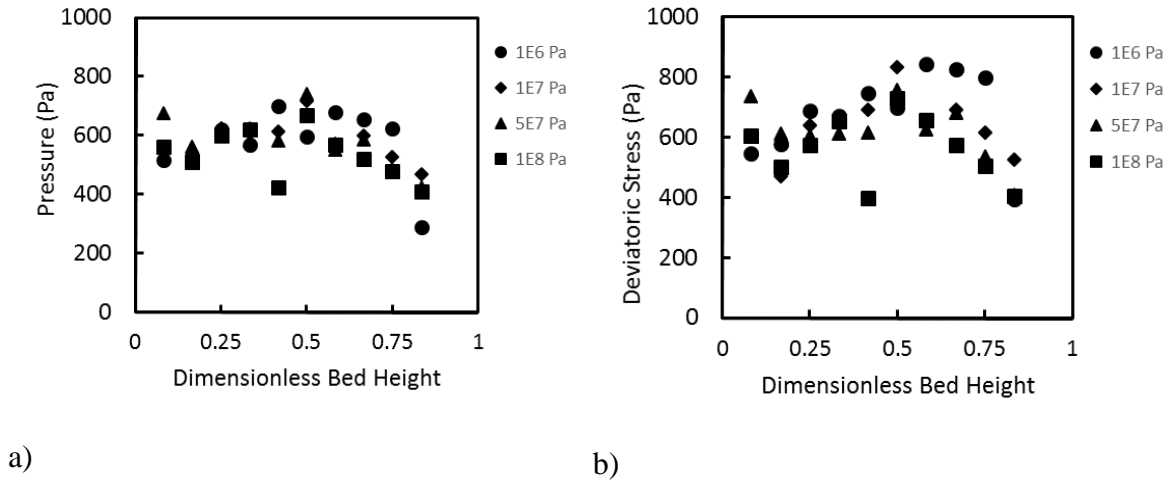


Figure 5.3.8 a) Pressure and b) deviatoric stress versus dimensionless bed height as a function of Young's Modulus with the remaining parameters at base case conditions

Figure 5.10 shows the effect of the friction coefficient on the average pressure and deviatoric stress in the shear cell at base case conditions. Friction coefficient is strongly correlated with the measured stresses. As the coefficient of friction increases from 0.1 to 1, the stress increases. This is expected since the friction in the bed allows for greater stress to build up in the bed before the stress network breaks down and induces motion. An order of magnitude change in the friction coefficient from 0.1 to 1 produces an increase from approximately 20 to 200 Pa in pressure and approximately 200 to 3000 in deviatoric stress. The effect of bed height and shear rate does not produce a trend that can be observed due to the overwhelming effect of the friction coefficient.

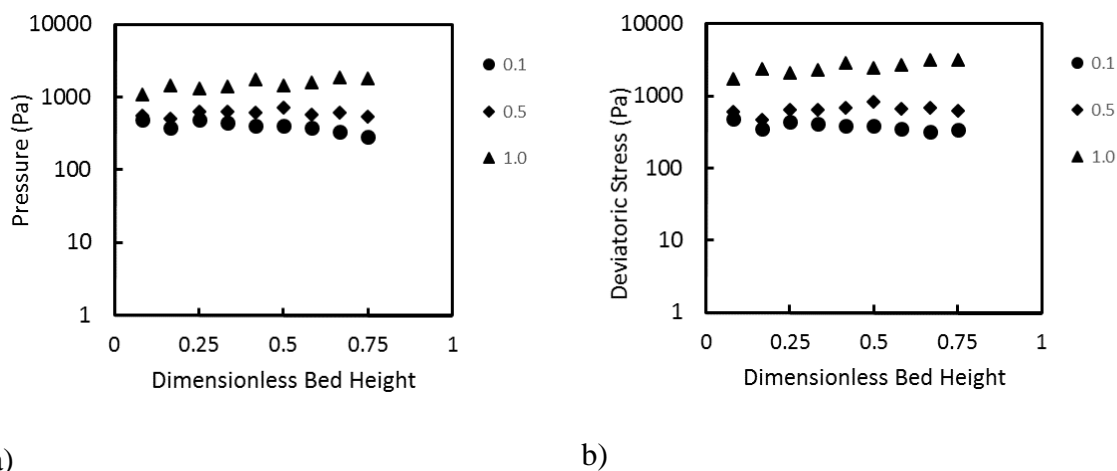


Figure 5.3.9 a) Pressure and b) deviatoric stress versus dimensionless bed height as a function of the friction coefficient with the remaining parameters at base case conditions

The pressure and deviatoric stress in the shear cell are highly sensitive to many of the material parameters in the model. The Young's modulus and especially the friction coefficient cause large variations in the calculated stress. Additionally, the location of the large particle changes the stress network within the bed and changes the location of the peak pressure and deviatoric stress in the bed. The location of the large particle typically coincides with the peak pressure and stress within the bed. Finally, the shear rate in the bed also affects the stress. The shear band at the top of the unit cell shows the greatest variation in stress as a function of bed height.

5.3.3 Particle of Interest Stress

The stress tensor of the large particle of interest is calculated with eqn. 5.7. The pressure and deviatoric stress are determined using eqn. 5.5 and 5.6. For each value, the error bars represent the estimated standard deviation of the average stress for all sampled time steps. Figure 5.11 – 5.13 shows the result of the stress on the large particle of interest.

Figure 5.11 shows the pressure and deviatoric stress on the large particle as a function of shear rate for each location of the large particle. The effect of shear rate is negligible within the standard deviation of the measurement and has a value of around 250 Pa for the pressure and 275 Pa for the deviatoric stress. Figure 5.4 demonstrated that the location of the shear band varied with the location of the large particle and figure 5.8 demonstrated that the peak stress was also a function of the location of the large particle. The combined results indicate that the large particle itself has a stronger effect on the stress in the shear cell than the shear cell does on the large particle. That is to say that the maximum stress in the shear cell is at the location of the large particle regardless of the location of the large particle in the bed.

Figure 5.12 shows the effect of the Young's modulus of the bulk material on the particle of interest stress. Figure 5.12 a shows the effect at a bed fraction of 0.4 and figure 5.12 b shows the effect at a bed fraction of 0.5. In both cases, the stress transmitted to the large particle increases from 100 to 400 Pa with increasing Young's modulus from 1×10^6 to 1×10^8 Pa. At low Young's modulus, the more elastic materials transmit less stress to the large particle than the stiffer bulk material at high Young's modulus. The bed height of the large particle does not have an appreciable effect on stress profile. This is consistent with the results for the shear profile and stress described earlier. The results show that over the two order of magnitude range of Young's modulus used in the simulation the stress profile increases by a factor of 4.

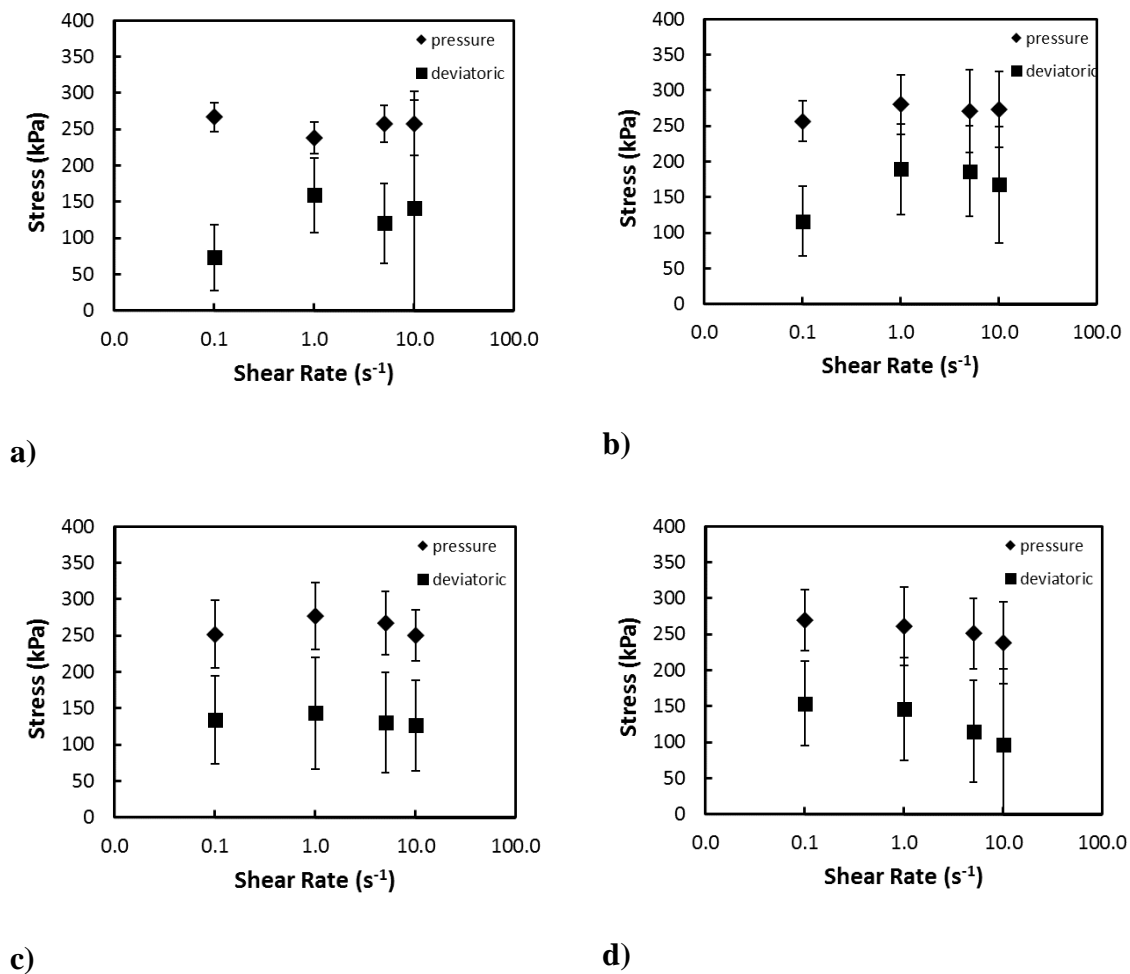


Figure 5.3.10 Effect of shear rate on pressure and deviatoric stress at a shear rate of 1 s⁻¹ and bed fractions of a) 0.3 b) 0.4 c) 0.5 and d) 0.6

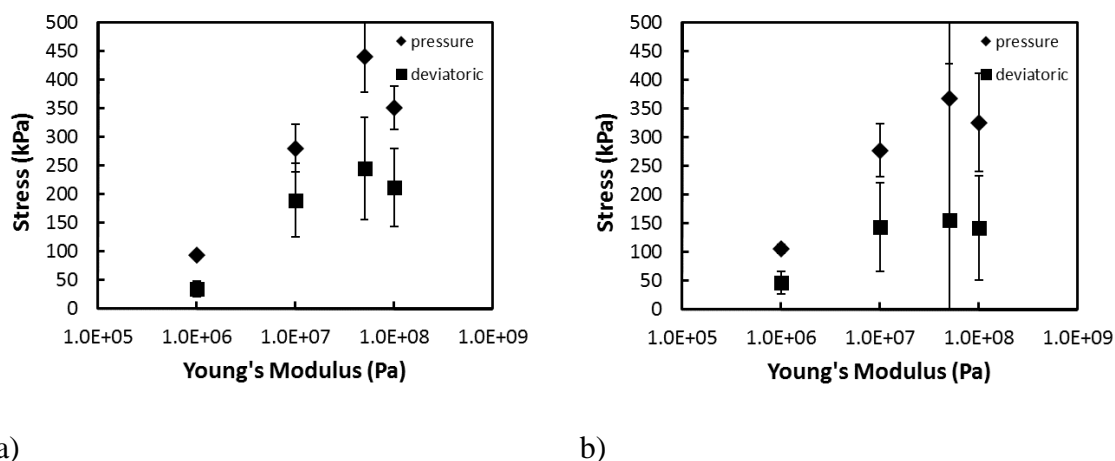


Figure 5.3.11 Effect of the young's modulus of the bulk material on the stress experienced by the particle of interest at a shear rate of 1 s⁻¹ and bed fraction of a) 0.4 and b) 0.5

Figure 5.13 demonstrate the effect of the coefficient of friction on the stress applied to the large particle. The pressure applied to the large particle does not show a strong dependence on the coefficient of friction at a value of approximately 300 Pa. However, the deviatoric stress shows a very strong dependence. The deviatoric stress increases from about 25 to 300 Pa, an order of magnitude, for an order of magnitude increase in the friction coefficient. This result is due to the ability of the bulk material to more easily move around the large particle of interest rather than apply a deviatoric stress.

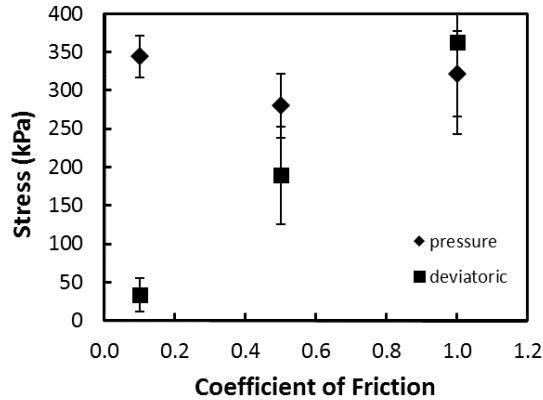


Figure 5.3.12 Effect of the coefficient of friction on pressure and deviatoric stress at a shear rate of 1 s⁻¹

The results of the stress applied to the large particle show the same effects that were observed for the stress and velocity profiles. In all cases, the effect of material properties was demonstrated to have a much large effect on the stress than the shear rate.

5.3.4 von Mises yield criterion

Tables 5.3 – 5.5 show the calculated results of the von Mises yield criteria for the large particle of interest. The von Mises yield criteria is the critical yield stress that below which an object will deform under the applied stress. Table 5.3 shows the critical yield stress to resist deformation obtained by varying the design parameters of the unit cell. Table 5.4 shows the result as a function of Young's modulus, and Table 5.5 shows the result of the friction coefficient. The results show that for all cases other than the lowest Young's modulus, the critical yield stress is on the order of 1000 kPa. Based on the results of the yield stress measurements in chapter 3 (0.1 – 1 kPa), the stress applied to the large particle will be enough to cause deformation and potentially breakage for all shear conditions in the shear cell. Even though the material parameters have an effect on

the critical yield stress value, the values is still several order of magnitude above the measured yield stress.

Table 5.3 von Mises yield criterion varying shear cell parameters

Yield Stress (kPa)		Shear Rate (s ⁻¹)			
		0.1	1	5	10
bed fraction	0.3	1170	1060	1140	1160
	0.4	1140	1250	1230	1240
	0.5	1150	1250	1210	1140
	0.6	1230	1190	1150	1110

Table 5.4 von Mises yield criterion varying Young's modulus

Yield Stress (kPa)	Young's modulus			
	1E+06	1E+07	5E+07	1E+08
	409	1250	1950	1570

Table 5.5 von Mises yield criterion varying friction coefficient

Yield stress (kPa)	Friction coefficient		
	0.1	0.5	1.0
	1250	1470	1510

5.4 Conclusions

The shear unit cell demonstrated the importance of large particle placement and material properties on the shear flow within the cell. The actual shear rate in the shear cell was found to a factor of 4 times greater in the shear band than the macroscopic target shear rate. The shear profile and propagation of momentum depended strongly on the Young's modulus, coefficient of friction, and large particle placement and less on the actual shear rate.

The DEM unit shear cell demonstrated that the effect of varying shear cell parameters such as the placement of the large particle and the shear rate had a much lower effect on the stress than the material properties. Obtaining quantitative results from the DEM simulations requires very careful characterization of material properties and validating them with experiments. However the results demonstrated that for all conditions in the shear cell, the von Mises yield criteria was much greater than the yield stress of the surfactant experimentally determined in chapter 3.

The shear unit cell needs to be validated against a physical unit cell to determine if the yield conditions predicted by the model are achieved in a real system. Important validation points include the flow profile and whether or not a material deforms in the shear band. Material of various yield stress will allow for the calibration of the model.

CHAPTER 6. CONCLUSIONS AND RECOMENDATIONS

6.1 Major Conclusions

The major conclusions of this work are summarized below.

In chapter 3:

1. Mechanical dispersion of semi-solid surfactant binders in a pin mixer is a breakage process where the breakage rate is dominated by the number of potential impacts of the pin with surfactant nuclei particles;
2. Due to the high impact velocity in the pin mill, the Stokes deformation number of collisions substantially exceeds the critical value required for failure, except for extremely stiff pastes. Therefore, the rate of mechanical dispersion is not controlled by the rheology of the paste.
3. Breakage rate does decrease as paste nuclei size decreases below 1mm, likely due to the reduced probability that a small particle will be hit by the pin as it passes. At short times, breakage rate is independent on impeller speed when normalized by the number of revolutions. At long times, the nuclei size decreases as impeller speed increases;
4. Achieving the required detergent granule size distribution relies on efficient mechanical dispersion (breakage) of the paste nuclei with granule growth via immersion nucleation (layering). Agglomeration of granules or paste nuclei should be avoided.

In chapter 4:

1. The full size distribution breakage of semi solid surfactants in the pin mixer can be modeled using an impact efficiency term times the number of revolutions of the impeller. As expected from the results in Chapter 3. The efficiency term uses the Stokes number as the dimensionless group describing breakage efficiency.
2. The model accurately predicts the effect of number of revolutions and tip speed. By fitting the model to a single impeller speed, the remaining impeller speeds are accurately predicted by only varying the impeller speed and angular speed in the model.
3. The properties of different surfactants can be mostly captured in the breakage distribution function fitting parameter. The efficiency fitting parameters are equipment dependent and do not need to be re-estimated for new formulations.

In Chapter 5:

1. The results of particle flow and stress are far more sensitive to the material parameters of the particles than to the macroscopic shear cell parameters. The coefficient of friction has the greatest effect on both the velocity profile and stress on the particle.
2. The location of the shear band and the location of the large particle are important in describing the shear flow but not as important in describing the stress on the particle. The maximum stress in the shear cell corresponds with the location of the large particle.

3. The von Mises yield criteria predicts that for all shear cases investigated in the shear cell, the surfactants in Chapter 3 will deform. The surfactants would need to have a yield stress of approximately 1000 kPa to resist deformation.

The three chapters of the thesis demonstrate a robust understanding of mechanical dispersion in the pin mixer. The rate processes has been mechanistically described using a semi-empirical model. The results show that the effect of the operating conditions has been accurate accounted for in the model. However, the higher order effect of changing surfactant rheology cannot be incorporated in the current model.

6.2 Recommendations for Further Study

This thesis was able to successfully model one rate process in detergent granulation. However the number of impeller rotations and efficiency approach to modeling mechanical dispersion may not be applicable to different geometries. Mechanical dispersion experiments in a vertical high shear mixer or pow mixer would allow for further understanding of the important mechanisms in mechanical dispersion. The results of the population balance model were also unable to predict the effect of changing yield stress on the particle size distribution. The model can be improved by performing additional experiments at a constant number of rotations but varying yield strength to appropriately identify the functional form of the Stokes deformation number. Additionally, the model population balance model developed is a 1D model. Although this is sufficient for surfactant breakage, describing additional rate processes will require more dimensions. The model will need to be converted into a multi-dimensional model so that it will be compatible with future models.

Many additional studies are needed before the entire granulation process can be modeled. While the mechanical dispersion of the surfactant has been described, the additional rate processes of consolidation and coalescences have not been evaluated. Further modeling of graduation will require isolating additional rate processes using the existing experiment as an end point. Detergent granulation uses a pin and plow mixer to produce granules and so characterizing the plow mixers effect on the pin mixer size distribution is an important next step in modeling the entire processes.

The DEM simulations have shown that careful experimental validation is necessary before any quantitative information can be extracted from the model. Shear cell experiments that correspond to the DEM simulators will allow for model validation. Once validated, further situations could be performed on the pin or plow mixer geometries. The results of these simulations could be used to predict the extent of surfactant breakage.

REFERENCES

REFERENCES

1. Iveson SM, Litster JD, Hapgood K, Ennis BJ. Nucleation, growth and breakage phenomena in agitated wet granulation processes: a review. *Powder Technol.* 2001;117(1-2):3–39. doi:10.1016/S0032-5910(01)00313-8.
2. Litster, Jim, Ennis B. *The Science and Engineering of Granulation Processes.* Dordrecht, The Netherlands: Kluwer Academic Publishers; 2004.
3. Ingram GD, Cameron IT. Challenges in Multiscale Modelling and its Application to Granulation Systems. *Dev Chem Eng Miner Process.* 2004;12(3):293–308.
4. Kayrak-Talay D, Dale S, Wassgren C, Litster J. Quality by design for wet granulation in pharmaceutical processing: Assessing models for a priori design and scaling. *Powder Technol.* 2013;240:7–18. doi:10.1016/j.powtec.2012.07.013.
5. Kumar A, Gernaey K V, Beer T De, Nopens I. Model-based analysis of high shear wet granulation from batch to continuous processes in pharmaceutical production - A critical review. *Eur J Pharm Biopharm.* 2013;85(3):814–32. doi:10.1016/j.ejpb.2013.09.013.
6. Rough S., Wilson D., Bayly a, York D. Tapping characterisation of high shear mixer agglomerates made with ultra-high viscosity binders. *Powder Technol.* 2003;132(2-3):249–266. doi:10.1016/S0032-5910(03)00075-5.

7. Forrest S, Bridgwater J, Mort PR, Litster J, Parker DJ. Flow patterns in granulating systems. *Powder Technol.* 2003;130(1-3):91–96. doi:10.1016/S0032-5910(02)00232-2.
8. Rowe RC. Binder-substrate interactions in granulation : a theoretical approach based on surface free energy and polarity. *Int J Pharm.* 1989;52:149–154.
9. Eshtiaghi N, Liu JS, Shen W, Hapgood KP. Liquid marble formation: Spreading coefficients or kinetic energy? *Powder Technol.* 2009;196(2):126–132. doi:10.1016/j.powtec.2009.07.002.
10. Hapgood KP, Farber L, Michaels JN. Agglomeration of hydrophobic powders via solid spreading nucleation. *Powder Technol.* 2009;188(3):248–254. doi:10.1016/j.powtec.2008.05.004.
11. Hapgood KP, Litster JD, Smith R. Nucleation regime map for liquid bound granules. *AIChE J.* 2003;49(2):350–361. doi:10.1002/aic.690490207.
12. Tardos GI, Khan MI, Mort PR. Critical parameters and limiting conditions in binder granulation of fine powders. *Powder Technol.* 1997;94:245–258.
13. Schaafsma SH, Vonk P, Kossen NW. Fluid bed agglomeration with a narrow droplet size distribution. *Int J Pharm.* 2000;193(2):175–87. Available at: <http://www.ncbi.nlm.nih.gov/pubmed/10606780>.
14. Emady HN, Kayrak-Talay D, Schwerin WC, Litster JD. Granule formation mechanisms and morphology from single drop impact on powder beds. *Powder Technol.* 2011;212(1):69–79. doi:10.1016/j.powtec.2011.04.030.
15. Hapgood KP, Khanmohammadi B. Granulation of hydrophobic powders. *Powder Technol.* 2009;189(2):253–262. doi:10.1016/j.powtec.2008.04.033.

16. Wildeboer WJ, Koppendraaier E, Litster JD, Howes T, Meesters G. A novel nucleation apparatus for regime separated granulation. *Powder Technol.* 2007;171(2):96–105. doi:10.1016/j.powtec.2006.09.008.
17. Wildeboer WJ, Litster JD, Cameron IT. Modelling nucleation in wet granulation. *Chem Eng Sci.* 2005;60(14):3751–3761. doi:10.1016/j.ces.2005.02.005.
18. Hapgood KP, Tan MXL, Chow DWY. A method to predict nuclei size distributions for use in models of wet granulation. *Adv Powder Technol.* 2009;20(4):293–297. doi:10.1016/j.appt.2008.09.004.
19. Tan MXL, Hapgood KP. Foam granulation: Liquid penetration or mechanical dispersion? *Chem Eng Sci.* 2011;66(21):5204–5211. doi:10.1016/j.ces.2011.07.012.
20. Tan MXL, Hapgood KP. Foam granulation: Effects of formulation and process conditions on granule size distributions. *Powder Technol.* 2012;218:149–156. doi:10.1016/j.powtec.2011.12.006.
21. Zhai H, Li S, Andrews G, Jones D, Bell S, Walker G. Nucleation and growth in fluidised hot melt granulation. *Powder Technol.* 2009;189(2):230–237. doi:10.1016/j.powtec.2008.04.021.
22. Hounslow MJ, Oullion M, Reynolds GK. Kinetic models for granule nucleation by the immersion mechanism. *Powder Technol.* 2009;189(2):177–189. doi:10.1016/j.powtec.2008.04.008.
23. Schaefer T, Mathiesen C. journal of Melt pelletization in a high shear mixer . VIII . Effects of binder viscosity. 1996;5173(96).

24. Schaefer T, Taagegaard B, Thomsen LJ, Kristensen HG. Melt pelletization in a high shear mixer . IV . Effects of process variables in a laboratory scale mixer. *Eur J Pharm Sci.* 1993;1:125–131.
25. Schaefer T, Mathiesen C. Melt pelletization in a high shear mixer IX. Effects of binder particle size. *Int J Pharm.* 1996;5173(96):139–148.
26. Rough SL, Wilson DI, Bayly a. E, York DW. Influence of Process Parameters on the Tapping Characteristics of High Shear Mixer Agglomerates Made with Ultra-High Viscosity Binders. *Chem Eng Res Des.* 2005;83(1):7–23.
doi:10.1205/cherd.03175.
27. Rough SL, Wilson DI, Bayly a. E, York DW. Mechanisms in high-viscosity immersion–granulation. *Chem Eng Sci.* 2005;60(14):3777–3793.
doi:10.1016/j.ces.2005.02.013.
28. Rough SL, Wilson DI, York DW. A regime map for stages in high shear mixer agglomeration using ultra-high viscosity binders. *Adv Powder Technol.* 2005;16(4):373–386. doi:10.1163/1568552054194186.
29. Iveson SM, Litster JD, Ennis BJ. Fundamental studies of granule consolidation Part 1: Effects of binder content and binder viscosity. *Powder Technol.* 1996;88(1):15–20. doi:10.1016/0032-5910(96)03096-3.
30. Iveson SM, Litster JD. Fundamental studies of granule consolidation part 2: Quantifying the effects of particle and binder properties. *Powder Technol.* 1998;99(3):243–250. doi:10.1016/S0032-5910(98)00116-8.

31. Ennis BJ, Tardos G, Pfeffer R. A microlevel-based characterization of granulation phenomena. *Powder Technol.* 1991;65(1-3):257–272. doi:10.1016/0032-5910(91)80189-P.
32. Ouchiyama, N, Tanaka T. Stochastic Model for Compaction of Pellets in Granulation. *Am Chem Soc.* 1980;19:555–560.
33. Cameron IT, Wang FY, Immanuel CD, Stepanek F. Process systems modelling and applications in granulation: A review. *Chem Eng Sci.* 2005;60(14):3723–3750. doi:10.1016/j.ces.2005.02.004.
34. Liu LX, Litster JD, Associates G, Road HH. Coalescence of Deformable Granules in Wet Granulation Processes. 2000;46(3):529–539.
35. X. Liu L, D. Litster J. Population balance modelling of granulation with a physically based coalescence kernel. *Chem Eng Sci.* 2002;57(12):2183–2191. doi:10.1016/S0009-2509(02)00110-0.
36. Darabi P, Pougatch K, Salcudean M, Grecov D. A novel coalescence model for binary collision of identical wet particles. *Chem Eng Sci.* 2009;64(8):1868–1876. doi:10.1016/j.ces.2009.01.017.
37. Iveson SM, Litster JD. Growth regime map for liquid-bound granules. *AIChE J.* 1998;44(7):1510–1518. doi:10.1002/aic.690440705.
38. Iveson SM, Wauters P a. L, Forrest S, Litster JD, Meesters GMH, Scarlett B. Growth regime map for liquid-bound granules: further development and experimental validation. *Powder Technol.* 2001;117(1-2):83–97. doi:10.1016/S0032-5910(01)00317-5.

39. Reynolds G, Fu J, Cheong Y, Hounslow M, Salman a. Breakage in granulation: A review. *Chem Eng Sci.* 2005;60(14):3969–3992. doi:10.1016/j.ces.2005.02.029.
40. Rumpf H. Physical Aspects of Comminution and New Formulation of a Law of Comminution HANS RUMPF. 1973;7:145–159.
41. Vogel L, Peukert W. Breakage behaviour of different materials—construction of a mastercurve for the breakage probability. *Powder Technol.* 2003;129(1-3):101–110. doi:10.1016/S0032-5910(02)00217-6.
42. Vogel L, Peukert W. From single particle impact behaviour to modelling of impact mills. 2005;60:5164–5176. doi:10.1016/j.ces.2005.03.064.
43. Vogel L, Peukert W. Determination of material properties relevant to grinding by practicable labscale milling tests. 2004:329–338.
doi:10.1016/j.minpro.2004.07.018.
44. Meier M, John E, Wieckhusen D, Wirth W, Peukert W. Characterization of the grinding behaviour in a single particle impact device: Studies on pharmaceutical powders. *Eur J Pharm Sci.* 2008;34(1):45–55. doi:10.1016/j.ejps.2008.02.120.
45. Bika DG, Gentzler M, Michaels JN. Mechanical properties of agglomerates. *Powder Technol.* 2001;117(1-2):98–112. doi:10.1016/S0032-5910(01)00318-7.
46. Ramkrishna D. *Population Balances. Theory and Applications to Particulate Systems in Engineering.* New York: Academic Press; 2000.
47. Ramkrishna D, Mahoney AW. Population balance modeling. Promise for the future. *Chem Eng Sci.* 2002;57(4):595–606. doi:10.1016/S0009-2509(01)00386-4.
48. Pandya JD, Spielman LA. Floc breakage in agitated suspensions - effect of agitation rate. *Chem Eng Sci.* 1983;38(12):1983–1992.

49. Diemer RB, Olson JH. A moment methodology for coagulation and breakage problems: Part 2 moment models and distribution reconstruction. *Chem Eng Sci.* 2010;57(12):2211–2228.
50. Hill PJ, Ng KM. New discretization procedure for the breakage equation. *AIChE J.* 1995;41(5):1204–1216.
51. Kostoglou M, Karabelas AJ. Theoretical analysis of the steady state particle size distribution in limited breakage processes. *J Phys.* 1998;31(44):8905–8921.
52. Kostoglou M. Exact self-similar solutions to the fragmentation equation with homogeneous discrete kernel. *J Phys.* 2003;320:84–96.
53. Ramachandran R, Immanuel CD, Stepanek F, Litster JD, Doyle FJ. A mechanistic model for breakage in population balances of granulation: Theoretical kernel development and experimental validation. *Chem Eng Res Des.* 2009;87(4):598–614. doi:10.1016/j.cherd.2008.11.007.
54. Capece M, Bilgili E, Davé R. Insight into first-order breakage kinetics using a particle-scale breakage rate constant. *Chem Eng Sci.* 2014;117:318–330. doi:10.1016/j.ces.2014.06.019.
55. Klimpel RR, Austin LG. The back-calculation of specific rates of breakage from continuous mill data. *Powder Technol.* 1984;38(1):77–91. doi:10.1016/0032-5910(84)80036-4.
56. Iveson SM. Limitations of one-dimensional population balance models of wet granulation processes. *Powder Technol.* 2002;124:219–229.

57. Capece M, Bilgili E, Dave R. Identification of the breakage rate and distribution parameters in a non-linear population balance model for batch milling. *Powder Technol.* 2011;208(1):195–204. doi:10.1016/j.powtec.2010.12.019.
58. Poon JM-H, Immanuel CD, Doyle IFJ, Litster JD. A three-dimensional population balance model of granulation with a mechanistic representation of the nucleation and aggregation phenomena. *Chem Eng Sci.* 2008;63(5):1315–1329. doi:10.1016/j.ces.2007.07.048.
59. Hounslow J, Ryall RL, Marshall VR. A Discretized Population Balance for Nucleation, Growth, and Aggregation. *AIChE J.* 1988;34(11):1821–1832.
60. David C, Joseph F, Iii D. Solution technique for a multi-dimensional population balance model describing granulation processes. *Powder Technol.* 2005;156:213–225. doi:10.1016/j.powtec.2005.04.013.
61. Li J, Freireich BJ, Wassgren CR, Litster JD. Experimental validation of a 2-D population balance model for spray coating processes. *Chem Eng Sci.* 2012;(1993):1–6. doi:10.1016/j.ces.2012.02.036.
62. Poon JM-H, Ramachandran R, Sanders CFW, et al. Experimental validation studies on a multi-dimensional and multi-scale population balance model of batch granulation. *Chem Eng Sci.* 2009;64(4):775–786. doi:10.1016/j.ces.2008.08.037.
63. Barrasso D, Oka S, Muliadi A, Litster JD, Wassgren C, Ramachandran R. Population balance model validation and prediction of CQAs for Continuous milling processes: Toward QbD in pharmaceutical drug product manufacturing. *J Pharm Innov.* 2013;8:147–162. doi:10.1007/s12247-013-9155-0.

64. Börner M, Peglow M, Tsotsas E. Derivation of parameters for a two compartment population balance model of Wurster fluidised bed granulation. *Powder Technol.* 2013;238:122–131. doi:10.1016/j.powtec.2012.04.014.
65. Braumann A, Kraft M, Mort PR. Parameter estimation in a multidimensional granulation model. *Powder Technol.* 2010;197(3):196–210. doi:10.1016/j.powtec.2009.09.014.
66. Barrasso D, El Hagrasy A, Litster JD, Ramachandran R. Multi-dimensional population balance model development and validation for a twin screw granulation process. *Powder Technol.* 2015;270:612–621. doi:10.1016/j.powtec.2014.06.035.
67. Freireich B, Li J, Litster J, Wassgren C. Incorporating particle flow information from discrete element simulations in population balance models of mixer-coaters. *Chem Eng Sci.* 2011;66(16):3592–3604. doi:10.1016/j.ces.2011.04.015.
68. Li J, Freireich B, Wassgren C, Litster JD. A General Compartment-Based Population Balance Model for Particle Coating and Layered Granulation. *AIChE J.* 2011;00(0). doi:10.1002/aic.
69. XI YU. An in-silico model of granulation. 2012.
70. Bouffard J, Bertrand F, Chaouki J. A multiscale model for the simulation of granulation in rotor-based equipment. *Chem Eng Sci.* 2012;81:106–117. doi:10.1016/j.ces.2012.06.025.
71. Liu H, Li M. Two-compartmental population balance modeling of a pulsed spray fluidized bed granulation based on computational fluid dynamics (CFD) analysis. *Int J Pharm.* 2014;475(1-2):256–269. doi:10.1016/j.ijpharm.2014.08.057.

72. Chaudhury A, Armenante ME, Ramachandran R. Compartment based population balance modeling of a high shear wet granulation process using data analytics. *Chem Eng Res Des.* 2015;95:211–228. doi:10.1016/j.cherd.2014.10.024.
73. Barrasso D, Eppinger T, Pereira FE, et al. A multi-scale, mechanistic model of a wet granulation process using a novel bi-directional PBM–DEM coupling algorithm. *Chem Eng Sci.* 2015;123:500–513. doi:10.1016/j.ces.2014.11.011.
74. Hampel N, Bück A, Peglow M, Tsotsas E. Continuous pellet coating in a Wurster fluidized bed process. *Chem Eng Sci.* 2013;86:87–98. doi:10.1016/j.ces.2012.05.034.
75. Meyer K, Bü A, Tsotsas E. Dynamic Multi-Zone Population Balance Model of particle formulation in fluidized beds. *Procedia Eng.* 2015;102(111):111. doi:10.1016/j.proeng.2015.01.279.
76. Chaudhury A, Niziolek A, Ramachandran R. Multi-dimensional mechanistic modeling of fluid bed granulation processes: An integrated approach. *Adv Powder Technol.* 2013;24(1):113–131. doi:10.1016/j.appt.2012.03.005.
77. Zhu HP, Zhou ZY, Yang RY, Yu a. B. Discrete particle simulation of particulate systems: A review of major applications and findings. *Chem Eng Sci.* 2008;63(23):5728–5770. doi:10.1016/j.ces.2008.08.006.
78. Gantt J a., Cameron IT, Litster JD, Gatzke EP. Determination of coalescence kernels for high-shear granulation using DEM simulations. *Powder Technol.* 2006;170(2):53–63. doi:10.1016/j.powtec.2006.08.002.

79. Gantt J a., Gatzke EP. High-shear granulation modeling using a discrete element simulation approach. *Powder Technol.* 2005;156(2-3):195–212.
doi:10.1016/j.powtec.2005.04.012.
80. Lian G, Thorntons RC, Adams MJ. Discrete particle simulation of agglomerate impact coalescence. *Chem Eng Sci.* 1998;53(19):3381–3391.
81. Remy B, Khinast JG, Glasser BJ. Wet Granular Flows in a Bladed Mixer : Experiments and Simulations of Monodisperse Spheres. *AIChE J.* 2012;58(11):3354–3369. doi:10.1002/aic.
82. Moakher M, Shinbrot T, Muzzio FJ. Experimentally validated computations of flow, mixing and segregation of non-cohesive grains in 3D tumbling blenders. *Powder Technol.* 2000;109(1-3):58–71. doi:10.1016/S0032-5910(99)00227-2.
83. McCarthy JJ, Khakhar D V, Ottino JM. Computational studies of granular mixing. *Powder Technol.* 2000;109(1-3):72–82. doi:10.1016/S0032-5910(99)00228-4.
84. Pandey P, Song Y, Kayihan F, Turton R. Simulation of particle movement in a pan coating device using discrete element modeling and its comparison with video-imaging experiments. *Powder Technol.* 2006;161(2):79–88.
doi:10.1016/j.powtec.2005.09.003.
85. Ng BH, Kwan CC, Ding YL, Ghadiri M. Granular Flow Fields in Vertical High Shear Mixer Granulators. *AIChE J.* 2008;54(2):415–426. doi:10.1002/aic.
86. Tsuji Y, Kawaguchi T, Tanaka T. Discrete particle simulation of two-dimensional fluidized bed. *Powder Technol.* 1993;77(1):79–87. doi:10.1016/0032-5910(93)85010-7.

87. Naeini SE, Spelt JK. Development of single-cell bulk circulation in granular media in a vibrating bed. *Powder Technol.* 2011;211(1):176–186.
doi:10.1016/j.powtec.2011.04.018.
88. Nakamura H, Fujii H, Watano S. Scale-up of high shear mixer-granulator based on discrete element analysis. *Powder Technol.* 2012.
doi:10.1016/j.powtec.2012.03.009.
89. Cundall, P.A., Strack ODL. A discrete numerical model for granular assemblies. *Geotechnique.* 1979;29(1):47–65.
90. Kruggel-Emden H, Simsek E, Rickelt S, Wirtz S, Scherer V. Review and extension of normal force models for the Discrete Element Method. *Powder Technol.* 2007;171(3):157–173. doi:10.1016/j.powtec.2006.10.004.
91. Di Renzo A, Di Maio FP. Comparison of contact-force models for the simulation of collisions in DEM-based granular flow codes. *Chem Eng Sci.* 2004;59(3):525–541. doi:10.1016/j.ces.2003.09.037.
92. Stevens a. B, Hrenya CM. Comparison of soft-sphere models to measurements of collision properties during normal impacts. *Powder Technol.* 2005;154(2-3):99–109. doi:10.1016/j.powtec.2005.04.033.
93. Zhu HP, Zhou ZY, Yang RY, Yu a. B. Discrete particle simulation of particulate systems: Theoretical developments. *Chem Eng Sci.* 2007;62(13):3378–3396.
doi:10.1016/j.ces.2006.12.089.
94. Freireich B, Litster J, Wassgren C. Using the discrete element method to predict collision-scale behavior: A sensitivity analysis. *Chem Eng Sci.* 2009;64(15):3407–3416. doi:10.1016/j.ces.2009.04.019.

95. Walton OR. Viscosity, granular-temperature, and stress calculations for shearing assemblies of inelastic, frictional disks. *J Rheol (N Y N Y)*. 1986;30(5):949.
doi:10.1122/1.549893.
96. Lee J, Herrmann HJ. Angle of repose and angle of marginal stability: molecular dynamics of granular particles. *J Phys A Math Gen*. 1993;26(2):373–383.
doi:10.1088/0305-4470/26/2/021.
97. Taguchi Y-H. New Origin of a Convective Motion: Elastically Induced Convection in Granular Materials. *Phys Rev Lett*. 1992;69(9):1367–1370.
98. Zhou YC, Wright BD, Yang RY, Xu BH, Yu a. B. Rolling friction in the dynamic simulation of sandpile formation. *Phys A Stat Mech its Appl*. 1999;269(2-4):536–553. doi:10.1016/S0378-4371(99)00183-1.
99. Yang RY, Zou RP, Yu a. B. Microdynamic analysis of particle flow in a horizontal rotating drum. *Powder Technol*. 2003;130(1-3):138–146.
doi:10.1016/S0032-5910(02)00257-7.
100. Poschel T. Granular material flowing down an inclined chute: a molecular dynamics simulation. *J Phys II*. 1993;3(1):27–40.
101. G. K, Kono K. Restitution Coefficient in a Collision between Two Spheres. *Jpn J Appl Phys*. 1987;26(8):1230–1233.
102. Brilliantov N, Spahn F, Hertzsch J, Pöschel T. Model for collisions in granular gases. *Phys Rev E Stat Phys Plasmas Fluids Relat Interdiscip Topics*. 1996;53(5):5382–5392. Available at:
<http://www.ncbi.nlm.nih.gov/pubmed/9964870>.

103. Oden JT, Martins JA. Models and Computational Methods for Dynamic Friction Phenomena. *Comput Methods Appl Mech Eng*. 1985;52:527–634.
104. Johnson KL, Kendall K, Roberts AD. Surface energy and the contact of elastic solids. *Proc R Soc London*. 1971;A 324:301–313.
105. Derjaguin BV, Muller VM, Toporov YP. Effect of contact deformations on the adhesion of particles. *Prog Surf Sci*. 1974;45(1-4):131–143. doi:10.1016/0079-6816(94)90044-2.
106. Talu I, Tardos GI, Khan MI. Computer simulation of wet granulation. *Powder Technol*. 2000;110(1-2):59–75. doi:10.1016/S0032-5910(99)00268-5.
107. Hare CL, Ghadiri M. Influence of measurement cell size on predicted attrition by the Distinct Element Method. *Powder Technol*. 2013;236:100–106. doi:10.1016/j.powtec.2012.04.061.
108. Hare C, Ghadiri M, Dennehy R. Prediction of attrition in agitated particle beds. *Chem Eng Sci*. 2011;66(20):4757–4770. doi:10.1016/j.ces.2011.06.042.
109. Antony SJ, Ghadiri M. Size Effects in a Slowly Sheared Granular Media. *J Appl Mech*. 2001;68(September):772. doi:10.1115/1.1387443.
110. Pianko-Oprych P, Nienow a. W, Barigou M. Positron emission particle tracking (PEPT) compared to particle image velocimetry (PIV) for studying the flow generated by a pitched-blade turbine in single phase and multi-phase systems. *Chem Eng Sci*. 2009;64(23):4955–4968. doi:10.1016/j.ces.2009.08.003.

111. Yang Z, Fryer PJ, Bakalis S, Fan X, Parker DJ, Seville JPK. An improved algorithm for tracking multiple, freely moving particles in a Positron Emission Particle Tracking system. *Nucl Instruments Methods Phys Res Sect A Accel Spectrometers, Detect Assoc Equip.* 2007;577(3):585–594.
doi:10.1016/j.nima.2007.01.089.
112. Kousaka Y, Kikuo O, Atsuyoshi S, Tetsuo Y. Dispersion Mechanism of Aggregate Particles in Air. *J Chem Eng Japan.* 1979;12(2):152–159.
113. Tabor D. *The Hardness of Metals.* (Jackson W, Frohlich H, Mott NF, eds.). London, UK: Oxford: Clarendon Press; 1951.
114. Smith RM, Liu LX, Litster JD. Breakage of drop nucleated granules in a breakage only high shear mixer. *Chem Eng Sci.* 2010;65(21):5651–5657.
doi:10.1016/j.ces.2010.06.037.
115. Sun A, Gunasekaran S. *Yield Stress in Foods: Measurements and Applications.*; 2009. doi:10.1080/10942910802308502.
116. Tardos GI, Hapgood KP, Ipadeola OO, Michaels JN. Stress measurements in high-shear granulators using calibrated “test” particles: application to scale-up. *Powder Technol.* 2004;140(3):217–227. doi:10.1016/j.powtec.2004.01.015.
117. Adams MJ, Edmondson B. An experimental and theoretical study of the squeeze-film deformation and flow of elastoplastic fluids. 1994;51:61–78.
118. Darelius A, Rasmuson A, van Wachem B, Niklasson Björn I, Folestad S. CFD simulation of the high shear mixing process using kinetic theory of granular flow and frictional stress models. *Chem Eng Sci.* 2008;63(8):2188–2197.
doi:10.1016/j.ces.2008.01.018.

119. Ng BH, Ding YL, Ghadiri M. Modelling of dense and complex granular flow in high shear mixer granulator-A CFD approach. *Chem Eng Sci.* 2009;64(16):3622–3632. doi:10.1016/j.ces.2009.05.011.
120. Darelus A, Rimmelgas J, Rasmuson A, van Wachem B, Bjørn IN. Fluid dynamics simulation of the high shear mixing process. *Chem Eng J.* 2010;164(2-3):418–424. doi:10.1016/j.cej.2009.12.020.
121. Zhang Y, An Z, Bai H, Li Q, Guo Z. Characterization and measurement of apparent viscosity of solid particles in fixed beds under high temperature. *Powder Technol.* 2015;284:279–288. doi:10.1016/j.powtec.2015.06.069.
122. Davies CN, Peetz C V. Impingement of particles on a transverse cylinder. *Proc R Soc London Ser A Math Phys Sci.* 1956;234(1197):269–295.
123. Kiparissides A, Koutinas M, Pistikopoulos EN, Mantalaris A. *Model Development and Analysis of Mammalian Cell Culture Systems.*; 2010. doi:10.1002/9783527631339.ch12.
124. Boukouvala F, Chaudhury A, Sen M, et al. Computer-aided flowsheet simulation of a pharmaceutical tablet manufacturing process incorporating wet granulation. *J Pharm Innov.* 2013;8(1):11–27. doi:10.1007/s12247-012-9143-9.
125. Khola N, Wassgren C. Correlations for Shear-Induced Percolation Segregation in Granular Shear Flows. *Powder Technol.* 2015;288:441–452. doi:10.1016/j.powtec.2015.11.003.
126. Göncü F, Durán O, Luding S. Constitutive relations for the isotropic deformation of frictionless packings of polydisperse spheres. *Comptes Rendus Mécanique.* 2010;338(10-11):570–586. doi:10.1016/j.crme.2010.10.004.

APPENDICES

Appendix A Kinetic Data

Confidence intervals are shown for experiments with more than 2 replicates.

sieve mean size μm	Kinetic Data with 90% CI											
	0 s		1 s		2 s		3 s		4 s		10 s	
	fv(ln(x))	CI +/-	fv(ln(x))	CI +/-	fv(ln(x))	CI +/-	fv(ln(x))	CI +/-	fv(ln(x))	CI +/-	fv(ln(x))	CI +/-
4800	0.435	0.561	0.154	0.156	0.002	0.014	0.003	0.007	0.000	0.000	0.000	0.000
3400	0.398	0.375	0.249	0.028	0.006	0.003	0.003	0.007	0.000	0.000	0.000	0.000
2400	0.292	0.306	0.463	0.262	0.048	0.129	0.018	0.018	0.000	0.000	0.000	0.000
1700	0.190	0.283	0.595	0.101	0.231	0.169	0.109	0.008	0.023	0.004	0.000	0.000
1200	0.097	0.129	0.572	0.180	0.564	0.147	0.409	0.030	0.217	0.036	0.004	0.038
855	0.051	0.084	0.391	0.064	0.759	0.053	0.739	0.025	0.665	0.110	0.078	0.073
605	0.031	0.041	0.222	0.147	0.632	0.176	0.746	0.011	0.881	0.001	0.540	0.281
427.5	0.013	0.001	0.120	0.035	0.400	0.193	0.472	0.023	0.623	0.065	1.220	0.051
302.5	0.012	0.001	0.043	0.037	0.178	0.085	0.206	0.018	0.273	0.082	0.568	0.188
215	0.007	0.042	0.039	0.002	0.114	0.052	0.130	0.022	0.173	0.107	0.302	0.042

Figure A.1 Surfactant A 1200 RPM

sieve mean size μm	Kinetic Data with 90% CI											
	0 s		1 s		2 s		3 s		4 s		10 s	
	fv(ln(x))	CI +/-	fv(ln(x))	CI +/-	fv(ln(x))	CI +/-	fv(ln(x))	CI +/-	fv(ln(x))	CI +/-	fv(ln(x))	CI +/-
4800	0.348		0.174		0.009		0.000		0.000		0.000	0.000E+00
3400	0.329		0.339		0.035		0.000		0.000		0.000	0.000E+00
2400	0.188		0.486		0.123		0.011		0.000		0.000	0.000E+00
1700	0.177		0.547		0.409		0.107		0.047		0.000	4.282E-06
1200	0.094		0.498		0.633		0.419		0.259		0.004	9.449E-06
855	0.039		0.319		0.698		0.768		0.764		0.137	2.741E-05
605	0.013		0.189		0.488		0.739		0.865		0.851	2.215E-05
427.5	0.013		0.102		0.274		0.456		0.558		1.088	6.377E-05
302.5	0.013		0.044		0.122		0.196		0.249		0.499	3.177E-05
215	0.000		0.059		0.105		0.139		0.190		0.287	6.257E-05

Figure A.2 Surfactant A 900 RPM

sieve mean size μm	Kinetic Data with 90% CI											
	0 s		1 s		2 s		3 s		4 s		10 s	
	fv(ln(x))	CI +	fv(ln(x))	CI +	fv(ln(x))	CI +	fv(ln(x))	CI +	fv(ln(x))	CI +	fv(ln(x))	CI +
4800	0.291		0.511		0.238		0.086		0.059		0.000	0.0E+00
3400	0.175		0.434		0.495		0.231		0.156		0.000	0.0E+00
2400	0.119		0.370		0.542		0.514		0.449		0.024	6.8E-06
1700	0.062		0.241		0.581		0.856		0.814		0.189	7.7E-05
1200	0.026		0.128		0.335		0.661		0.768		0.801	3.4E-04
855	0.000		0.050		0.132		0.277		0.360		0.966	1.7E-05
605	0.000		0.025		0.053		0.106		0.159		0.536	4.6E-04
427.5	0.000		0.013		0.030		0.048		0.058		0.230	4.0E-04
302.5	0.000		0.025		0.023		0.059		0.034		0.085	1.9E-04
215	0.000		0.000		0.031		0.013		0.036		0.046	6.2E-05

Figure A.3 Surfactant A 600 RPM

sieve mean size μm	Kinetic Data with 90% CI											
	0 s		1 s		2 s		3 s		10 s			
	fv(ln(x))	CI +	fv(ln(x))	CI +	fv(ln(x))	CI +	fv(ln(x))	CI +	fv(ln(x))	CI +		
4800	0.000	0.000	0.000	0.000	0.000	0.000	0.000	0.000	0.000	0.000	0.000	
3400	1.254	0.365	0.135	0.146	0.012	0.020	0.007	0.011	0.000	0.000	0.000	
2400	0.350	0.043	0.153	0.051	0.047	0.039	0.024	0.038	0.000	0.000	0.000	
1700	0.390	0.094	0.292	0.068	0.107	0.069	0.042	0.019	0.004	0.024	0.024	
1200	0.336	0.112	0.551	0.052	0.341	0.080	0.150	0.043	0.031	0.104	0.104	
855	0.255	0.094	0.609	0.048	0.597	0.040	0.484	0.065	0.334	1.032	1.032	
605	0.174	0.058	0.579	0.057	0.817	0.102	0.921	0.040	1.077	0.208	0.208	
427.5	0.090	0.025	0.407	0.040	0.643	0.093	0.840	0.048	1.042	0.883	0.883	
302.5	0.041	0.008	0.200	0.070	0.358	0.069	0.449	0.063	0.425	0.478	0.478	

Figure A.4 Surfactant B 1200 RPM

sieve mean size μm	Kinetic Data with 90% CI											
	0 s		1 s		2 s		3 s		10 s			
	fv(ln(x))	CI +	fv(ln(x))	CI +	fv(ln(x))	CI +	fv(ln(x))	CI +	fv(ln(x))	CI +		
4800	0.472		0.187		0.005	0.033	0.004	0.023	0.002			
3400	0.328		0.383		0.145	0.089	0.014	0.002	0.001			
2400	0.213		0.449		0.311	0.145	0.014	0.002	0.002			
1700	0.182		0.632		0.678	0.191	0.218	0.035	0.009			
1200	0.094		0.529		0.733	0.074	0.642	0.125	0.239			
855	0.042		0.296		0.524	0.064	0.874	0.184	0.967			
605	0.024		0.161		0.308	0.054	0.666	0.019	1.012			
427.5	0.015		0.078		0.154	0.027	0.390	0.072	0.505			
302.5	0.009		0.084		0.066	0.001	0.111	0.070	0.186			

Figure A.5 Surfactant B 900 RPM

sieve mean size μm	Kinetic Data with 90% CI									
	1 s		2 s		3 s		4 s		10 s	
	$f_v(\ln(x))$	CI +/-	$f_v(\ln(x))$	CI +/-	$f_v(\ln(x))$	CI +/-	$f_v(\ln(x))$	CI +/-	$f_v(\ln(x))$	CI +/-
4800	0.424		0.000		0.000	0.000	0.002		0.000	
3400	0.440		0.013		0.023	3.2E-02	0.001		0.000	
2400	0.452		0.120		0.169	2.0E-01	0.002		0.016	
1700	0.547		0.453		0.430	2.9E-01	0.009		0.306	
1200	0.522		0.773		0.774	1.8E-01	0.239		1.073	
855	0.291		0.668		0.732	1.5E-01	0.967		0.924	
605	0.190		0.499		0.490	2.5E-01	1.012		0.412	
427.5	0.055		0.288		0.229	2.0E-01	0.505		0.155	
302.5	0.007		0.115		0.086	1.1E-01	0.186		0.058	

Figure A.6 Surfactant B 600 RPM

Appendix B Full size distributions of breakage model

The full size distributions for the gSOLIDS are shown here.

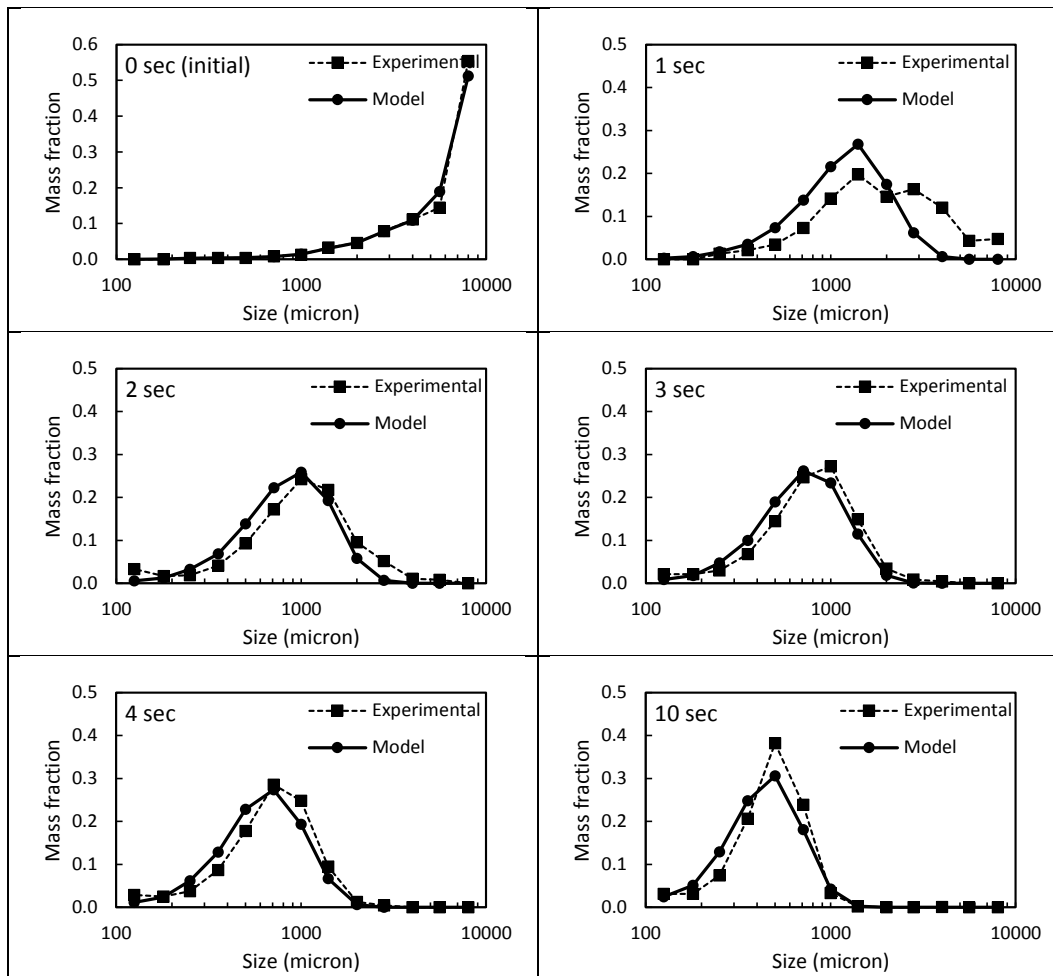


Figure B.1 Particle size distributions of model and experiments for Surfactant A at 900 RPM fit to 1200 RPM experiment data.

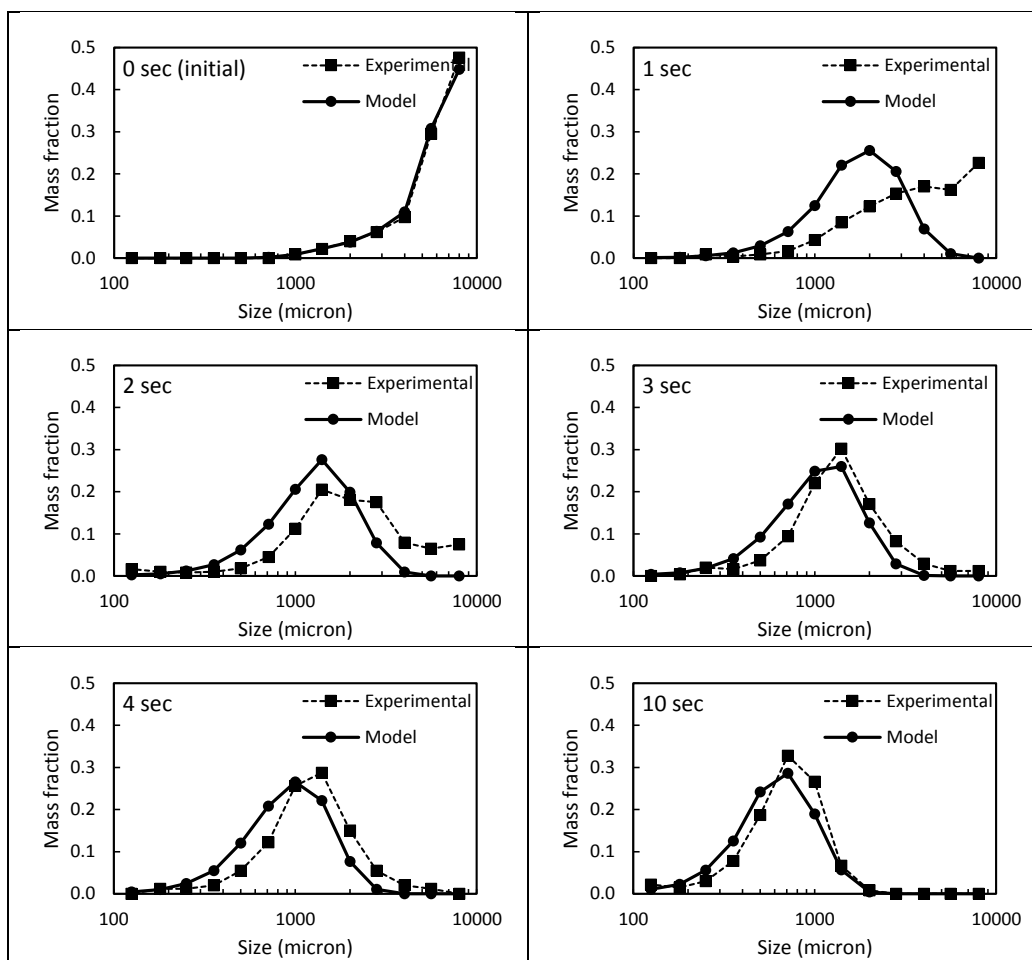


Figure B.2 Particle size distributions of model and experiments for Surfactant A at 600 RPM fit to 1200 RPM experiment data.

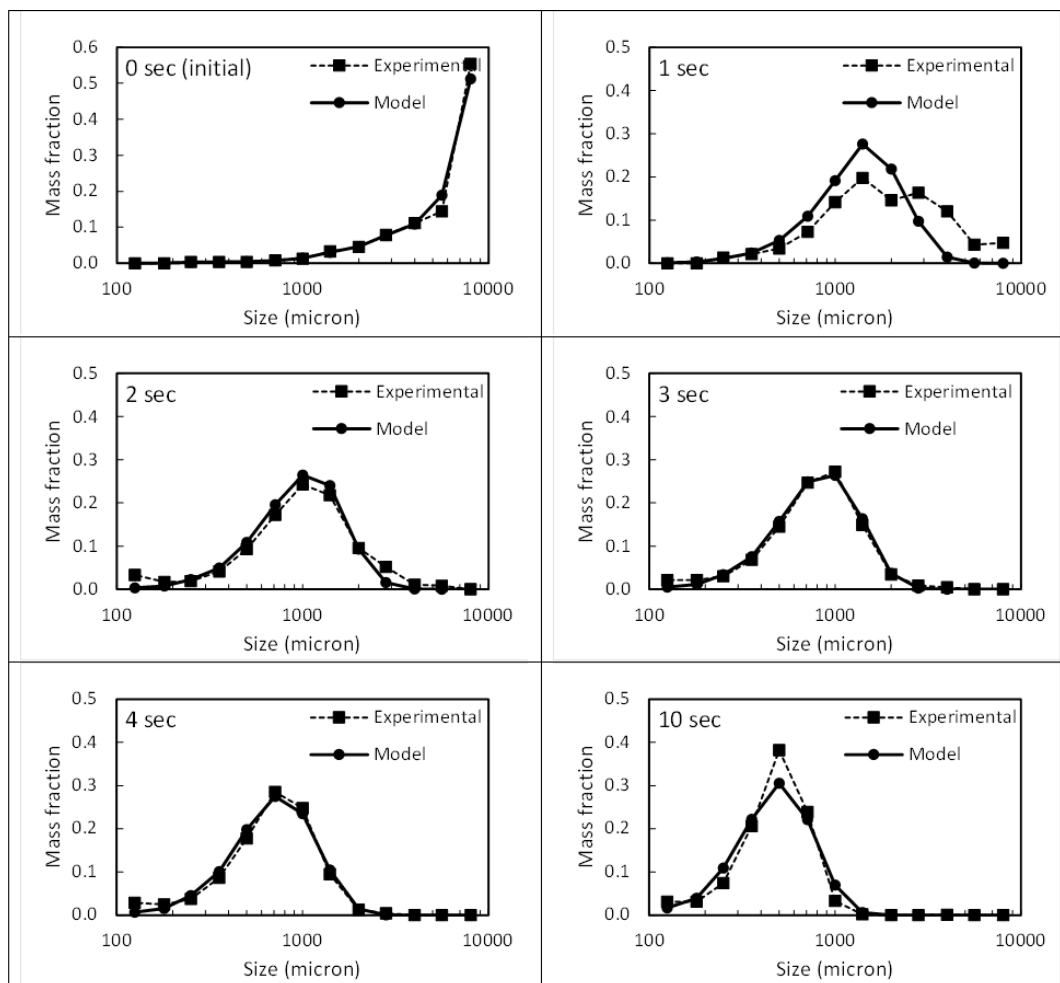


Figure B.3 Particle size distributions of model and experiments for Surfactant A at 900 RPM fit to all experiment data.

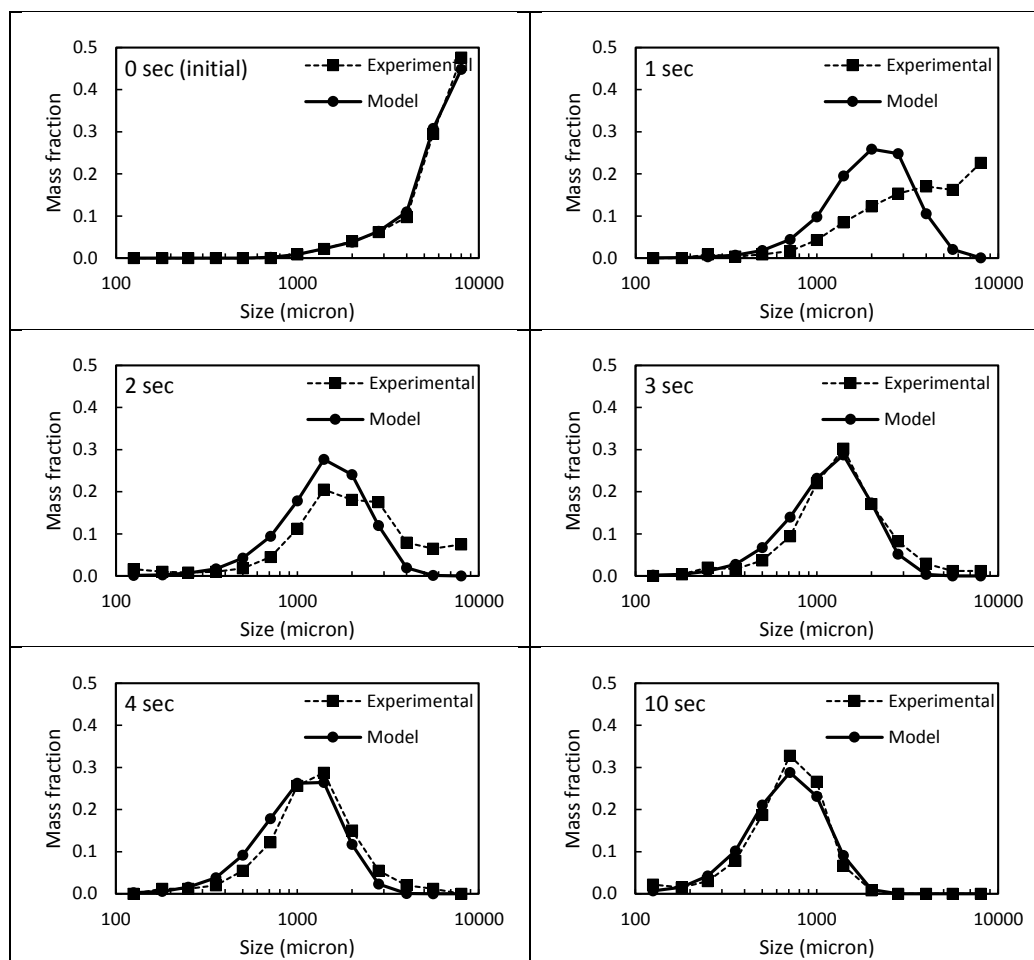


Figure B.4 Particle size distributions of model and experiments for Surfactant A at 600 RPM fit to all experiment data.

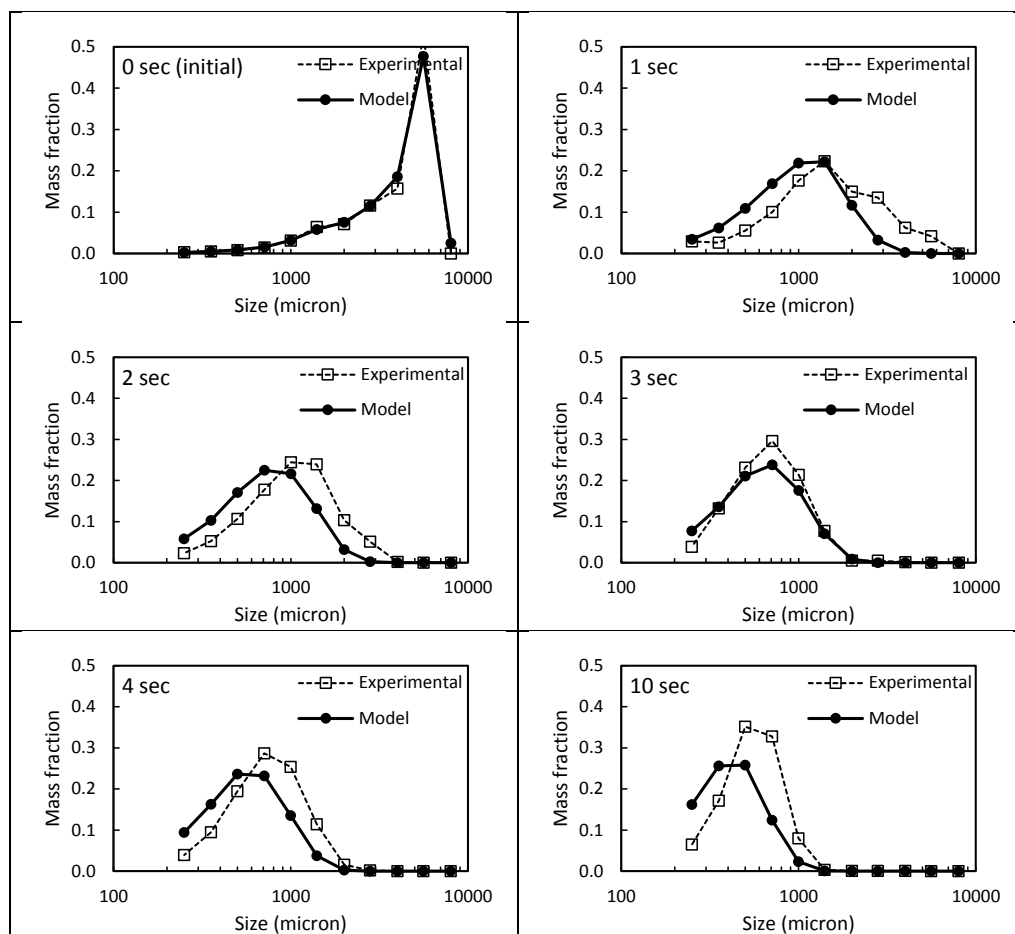


Figure B.5 Particle size distributions of model and experiments for Surfactant B at 900 RPM fit to 1200 RPM experiment data.

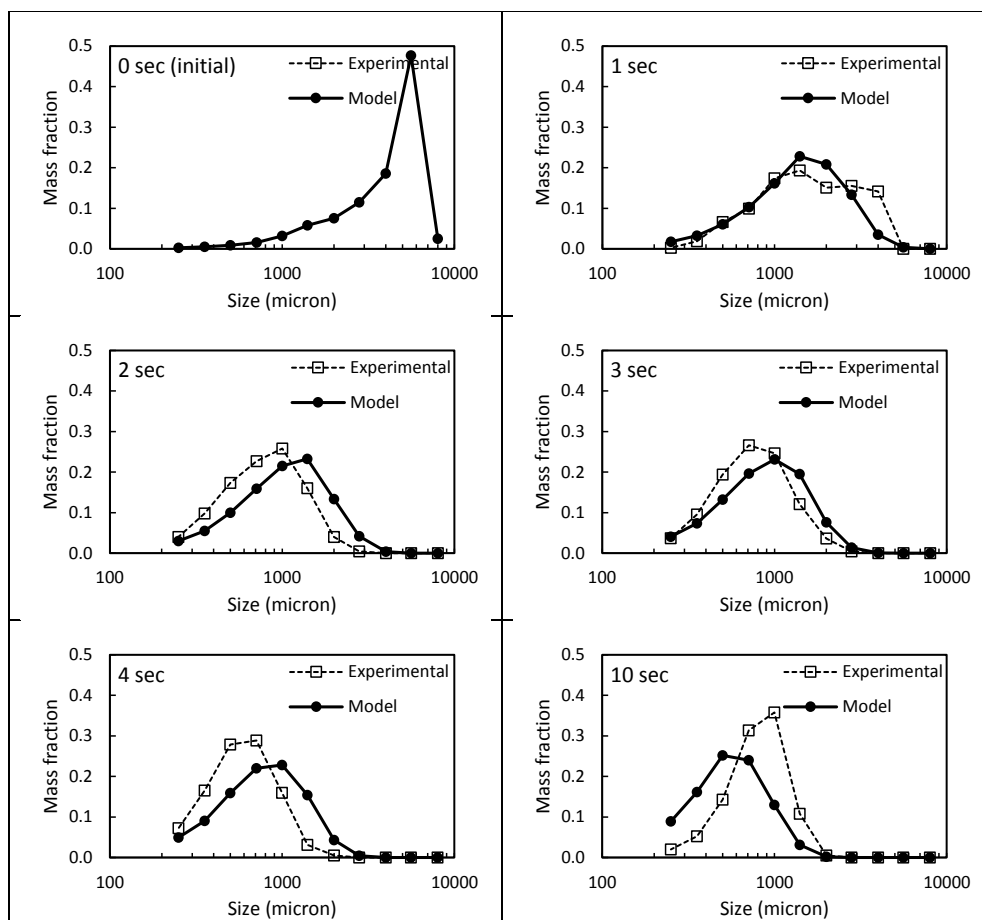


Figure B.6 Particle size distributions of model and experiments for Surfactant B at 900 RPM fit to 1200 RPM experiment data.

VITA

VITA

Education:**Purdue University – West Lafayette, IN**

Ph.D. in Chemical Engineering

Expected March 2016

B.S. in Chemical Engineering with Honors with Distinction

Minor in Chemistry

Graduated: May, 2011

Academic Experience:**1. Purdue University; West Lafayette, IN:**

Mechanical Dispersion of Binders in Granulation (PhD Thesis Topic)

May 2012 – present

2. University of Sheffield; Sheffield, UK:

Collaboration at University of Sheffield with Professor Rachel Smith

Oct 2013 – present

3. Purdue University; West Lafayette, IN:

Undergraduate Research Position & SURF

May 2010 – May 2011